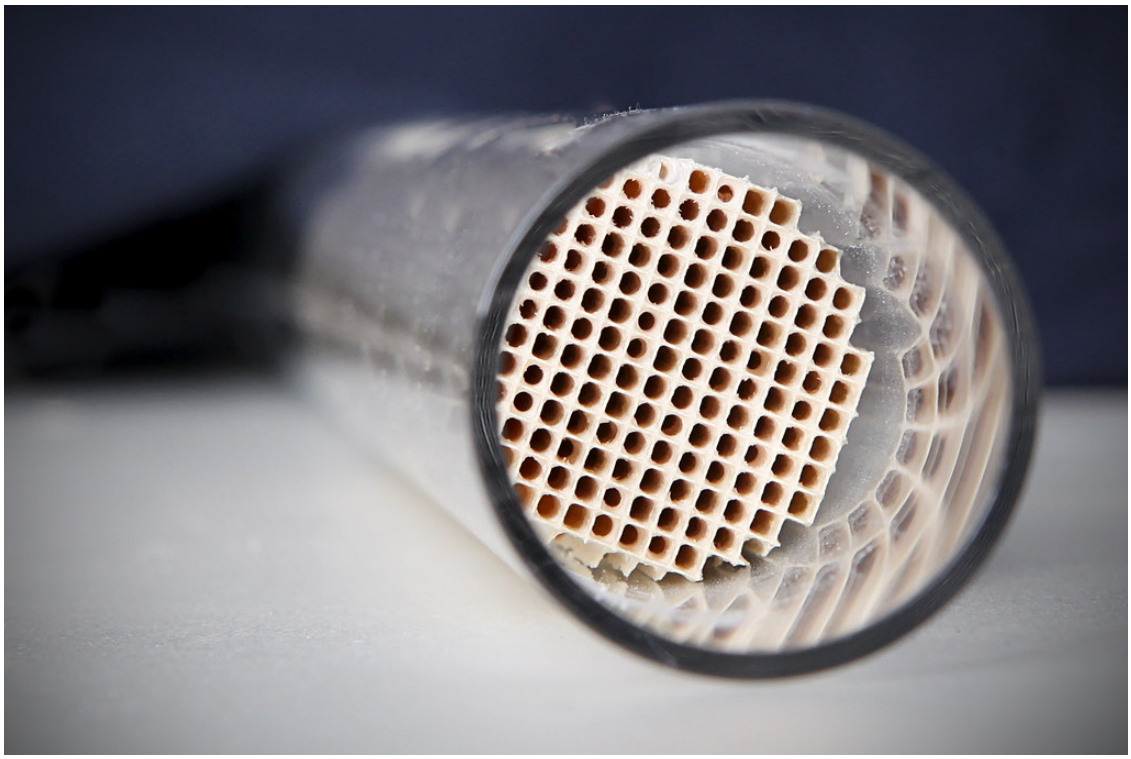

[1]

# Optimization of a Three-Way Catalytic Converter Through Engine Test-Bench Experiments

Master's thesis in Systems, Control and Mechatronics

VICTOR HERNVALL ABHILASH RAVICHANDRAN

DEPARTMENT OF MECHANICS AND MARITIME SCIENCES

CHALMERS UNIVERSITY OF TECHNOLOGY
Gothenburg, Sweden 2021
www.chalmers.se

Master's thesis 2021

# Optimization of a Three-Way Catalytic Converter Through Engine Test-Bench Experiments

VICTOR HERNVALL
ABHILASH RAVICHANDRAN


CHALMERS
UNIVERSITY OF TECHNOLOGY

Department of Mechanics and Maritime Sciences
*Division of Combustion and Propulsion Systems*
Chalmers University of Technology
Gothenburg, Sweden 2021

Optimization of a Three-Way Catalytic Converter Through Engine Test-Bench Experiments
VICTOR HERNVALL; ABHILASH RAVICHANDRAN



Supervisors: Anton Ajne and Fredrik Wemmert, Powertrain Engineering Sweden
Examiner: Jonas Sjöblom, Division of Combustion and Propulsion Systems

Master's Thesis 2021:71
Department of Mechanics and Maritime Sciences
Division of Combustion and Propulsion Systems
Chalmers University of Technology
SE-412 96 Gothenburg
Telephone +46 31 772 1000

Typeset in LaTeX
Printed by Chalmers Reproservice
Gothenburg, Sweden 2021

Optimization of a Three-Way Catalytic Converter Through Engine Test-Bench Experiments

VICTOR HERNVALL, ABHILASH RAVICHANDRAN
Department of Mechanics and Maritime Sciences
Chalmers University of Technology

# Abstract

A three-way catalytic converter model designed in a preceding thesis has been refined and translated from SIMULINK into a script-based MATLAB model, to produce faster, more stable and accurate solutions for the ordinary differential equations (ODE). The model consists of nine ODE's and are solved using the in-built $ode15s$ solver. The states of the model include $O_2$, CO, $C_3H_6$, $C_3H_8$, $H_2$, NO, $CO_2$, $H_2O$ concentrations and oxygen buffer levels for each slice of the catalyst. The scope of the thesis is to gain an in-depth understanding of the workings within the catalyst by conducting experiments in a test-rig where an engine has been used, so as to mimic the composition of the exhaust in a real driving scenario, which is lacking within the scope of literature. The thesis suggests a variety of methods to collect and analyze data, these include using catalysts of different axial lengths (70, 30 and 15mm) and utilizing a heat-exchanger that allow the temperature dynamics to be studied at higher resolution. The collected data is then used to optimize 30 kinetic parameters in the model with the help of a built-in MATLAB function, $lsqnonlin$. Results show that good emission predictions can be obtained for certain space-velocities, with exceptions in higher temperature regions where the model lacks a mass transfer description.

Keywords: Three-way catalyst, optimization, lsqnonlin, MATLAB, ode, ceria, oxygen buffer.

# Acknowledgements

To begin with, thanks to our friends and family for support and care during this (occasionally) challenging time. Thank you Fredrik Wemmert and Anton Ajne at PES for your indespensible expertise and support. This thesis would not have succeeded without you. Additionally, thank you Jonas Sjöblom for your feedback and expertise, keeping us on the right track. Shout-outs to Mats Laurell for occasional input on our work and finally; thank you Anders Botéus for help with practical stuff!

Victor Hernvall, Trollhättan, July 2021
Abhilash Ravichandran, Gothenburg, July 2021

# Contents

# List of Figures

# List of Tables

# Nomenclature

**Abbreviations**

| | |
|---|---|
| $AFR$ | Air-fuel ratio |
| $CLD$ | Chemiluminescence detector |
| $CPSI$ | Cells per square inch |
| $CSTR$ | Continuously stirred tank reactor |
| $EATS$ | Exhaust Aftertreatment System |
| $ECU$ | Engine control unit |
| $EIMS$ | Electron ionization mass spectrometry |
| $EO$ | Engine out |
| $FID$ | Flame ionization detection |
| $HE$ | Heat exchanger |
| $L2R$ | Lean to rich |
| $LUT$ | Look-up table |
| $MPD$ | Magneto-pneumatic detector |
| $OBL$ | Oxygen buffer level |
| $ODE$ | Ordinary differential equation |
| $OSC$ | Oxygen storage capacity |
| $PDE$ | Partial differential equation |
| $ppm$ | Parts per million |
| $R2L$ | Rich to lean |
| $SI$ | Spark ignition |
| $SR$ | Steam reforming |
| $TP$ | Tailpipe |
| $TWC$ | Three-way catalyst |
| $WGS$ | Water gas shift |

**Species**

| | |
|---|---|
| $C_3H_6$ | Propane |
| $C_3H_8$ | Propene |
| $Ce$ | Cerium |
| $CO$ | Carbon monoxide |
| $CO_2$ | Carbon dioxide |
| $H_2$ | Hydrogen |
| $H_2O$ | Water |
| $H_2S$ | Hydrogen sulfide |
| $HC$ | Hydrocarbons |
| $N_2$ | Nitrogen |
| $NO_x$ | Nitrous oxides |

| | | |
|---|---|---|
| $O_2$ | Oxygen | |
| $SO_2$ | Sulphur dioxide | |
| **Indices** | | |
| $a$ | Ambient | |
| $exh$ | Exhaust | |
| $g$ | Gas | |
| $ref$ | Reference | |
| $s$ | Solid | |
| **Variables** | | |
| $\Delta G_{WGS}$ | Water gas shift Gibbs free energy | J/mol |
| $\dot{m}$ | Mass flow | kg/s |
| $\dot{V}$ | Volume flow | $m^3$/s |
| $\lambda$ | Normalized AFR | - |
| $\nu$ | Stoichiometric reaction constant | - |
| $\Theta$ | Oxygen buffer level | - |
| $A$ | Pre-exponential factor | 1/s |
| $a$ | Effective area | $m^2$ |
| $C_p$ | Specific heat capacity | J/kgK |
| $C_x$ | Concentration of species x | mol/$m^3$ |
| $E$ | Activation energy | J/mol |
| $E_{i,G}$ | Inhibition exponential term | K |
| $G$ | Inhibition factor | - |
| $H$ | Enthalpy | J/mol |
| $h$ | Heat transfer coefficient | $W/m^2K$ |
| $k_i$ | Kinetic parameter [1] | $(m^3/mol)^n$ |
| $k_{i,G}$ | Inhibition kinetic parameter [2] | $(m^3/mol)^l$ |
| $K_i$ | Inhibition factor constant [3] | $m^3/mol)^m$ |
| $K_{WGS}$ | Water gas shift constant | - |
| $m$ | Mass | kg |
| $m_{load}$ | Engine load | mg/str |
| $N_{eng}$ | Engine speed | 1/min |
| $Q$ | Space velocity | 1/s |
| $R$ | Reaction rate | mol/$m^3$s |
| $R_g$ | Universal gas constant | J/mol K |
| $T$ | Temperature | K |
| $V$ | Catalyst volume | $m^3$ |

[1] l is 1 for R1-R9, l is 0 for R10-R15
[2] n is 1 if i=1,2,4, n is 4 if i=3
[3] m is 1 if i=1,2,4, m is 4 if i=3

# 1
# Introduction

The aim of this chapter is to motivate why catalytic converters are important, along with the scope and goal of this thesis.

## 1.1 Background

Constantly tougher legislation on vehicle emissions put stress on combustion after-treatment system development. This applies to spark-ignition (SI) engine exhausts, which contains harmful substances such as carbon monoxide (CO), nitrous oxides ($NO_x$), hydrocarbons (HC) and particulate matter (PM) as a result of incomplete combustion [5].

Ideally, the engine should be operated at stoichiometry, which is when the amount of fuel injected to a cylinder is mixed with the exact amount of air required for complete combustion. This is of course not feasible in practice, due to the air-to-fuel mixture not being completely homogeneous. Moreover, the reactions governing combustion require both time and high temperatures to reach a completed state.

By instead running with excess air, referred to as operating lean, a better fuel economy can be attained. The disadvantage however, is that the high amount of nitrogen ($N_2$) in air combined with high temperatures in the combustion chamber would give rise to $NO_x$ in the exhaust. A third alternative, is by running with a shortage of air, referred to as rich operation. This would yield higher engine performance, but would result in high CO and THC emission slips [6].

In order to further reduce the harmful emissions from vehicles, the Exhaust After Treatment Systems (EATS) are equipped with Three-Way-Catalysts (TWC). This is a device designed to accelerate the unfinished chemical reactions within the engine combustion chamber, ultimately lowering the concentrations of CO, $NO_x$ and HC at the exhaust tailpipe to legal standards. The name TWC originates from the fact that it can assist the simultaneous tasks of oxidizing CO and hydrocarbons to $CO_2$ and $H_2O$, as well as reducing $NO_x$ to $N_2$ [7].

The goal is to keep the emissions close to stoichiometry in order to obtain optimal conversions. This is in practice achieved via the use of control systems. Traditionally, a binary type catalyst control strategy, often referred to as bang-bang has been used. As the name suggest, it houses two control settings: which is either rich or

lean. To achieve the desired air-to-fuel ratio, a closed-loop control system using a wide band lambda($\lambda$)-sensor is used, complemented with the voltage readings from a binary $\lambda$-sensor, which are used to give feedback. These types of sensors will be described in more detail in Section 2.3. For example, if a lean air-fuel-mixture is detected by the sensor, the target AFR is set to rich. Similarly when the sensor detects a rich air-fuel-mixture, the target AFR is set to lean. This oscillatory behaviour is repeated, allowing the average AFR to remain close to stoichiometry [8].

Fig. 1.1 below displays conversion efficiencies within a catalyst as a function of $\lambda$, which is defined as the quotient of actual AFR to theoretical AFR (more detail is given in Section 2.2). It can be seen that operation close to stoichiometry ($\lambda = 1$) is necessary to attain good conversion- for all species simultaneously.

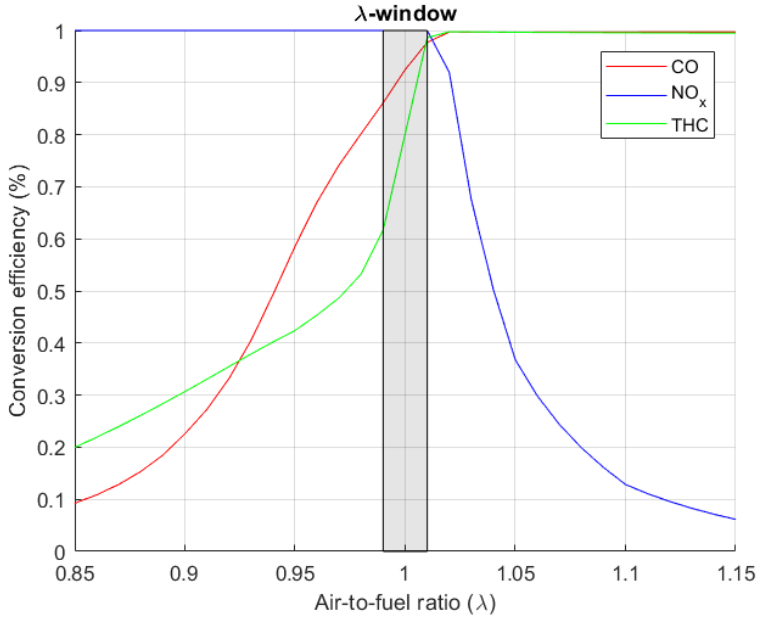


**Figure 1.1:** Conversion efficiency $\eta$ as a function of $\lambda$

## 1.2 Health- and Environmental Aspects

In their annual report on air-quality, the European Environment Agency (EEA), describes air-pollution as a major threat to both health and ecosystems. Regarding health, poor air-quality increases risk of suffering from respiratory- and cardiovascular diseases, as well as asthma and allergy [9]. According to WHO, air-pollution is a major risk filled health-concern in the world, that caused approximately 7 million deaths in 2016 [10].

In relation to the automotive industry, the main pollutants in SI-engine operation as described previously include $NO_x$, CO and HC. $NO_x$ gases cause acid rains, photochemical smog and ozone depletion [5]. Together with ammonia ($NH_3$), it can excessively unbalance the nitrogen nutrient in terrestrial and aquatic ecosystems,

ultimately causing eutrophication. Together with sulphur dioxide ($SO_2$), biodiversity loss can be caused by soil, lake and river acidification [9].

CO is highly toxic to humans as it can bind to haemoglobin, blocking the oxygen supply to the body tissue, ultimately causing suffocation [6]. HC can cause coughing and drowsiness, as well as show narcotic effects [6]. Some hydrocarbons are directly toxic and carcinogenic [5].

The United Nations has formulated two sustainability goals related to this topic. Goal 13: Climate Action considers the global emissions of $CO_2$, resulting in climate change due to an increased atmospheric temperature [11]. Goal 3: Good Health and Well-Being covers a vast range of topics, but in relation to the automotive industry local emission are considered, where focus is to mitigate release of the main pollutants [12].

In order to meet the goals, policy makers legislate allowed emission limits for vehicles. As an example, the current Euro 6/VI standards within the European Union dictates the limits of allowed pollution from light-duty and heavy-duty vehicles, respectively [13],[14]. Standards covers spark-ignited and compression-ignited vehicles. To give an example, the light-duty vehicle emission limits of a spark-ignited vehicle (of category N[1]) is displayed in Table 1.1 below [13]. $CO_2$ is also regulated, but within a different sphere, using a fleet average concept [15].

**Table 1.1:** Euro 6 emission limits for category N - spark-ignited vehicle

| Pollutants | CO | Total HC (THC) | $NO_x$ | PM |
|---|---|---|---|---|
| Limit (mg/km) | 1000 | 100 | 60 | 4.5 |

Additional letters, such as c, d-temp and d can be sometimes be seen appended to Euro 6. The original Euro 6 marking was introduced September 1st 2014 for type approval and September 1st 2015 for registration. It used the New European Driving Cycle (NEDC) for evaluation. From September 1st 2017, a switch from NEDC to the stricter Worldwide Harmonized Light-Duty Vehicles Test (WLTP) was made. Vehicles passing the WLTP were fit into the Euro 6c framework. Both NEDC and WLTP were protocols fitting into a lab-testing environment.

Also in September 2017, the Euro 6d-temp was introduced for new type approvals, working as a transition for manufacturers to adjust the switch from lab manifested protocols to the real drive emissions (RDE). A conformity factor of 2.1 was used, which allowed the emissions to be 2.1 times higher than the legislation frame for Euro 6c. Existing models had to adapt by September 2019.

[1]Motor vehicles with at least four wheels designed and constructed for the carriage of passengers

As the actual Euro 6d came into force for new type approval in Jan 2020, the conformity factor was decreased to 1.43. In Jan 2021 this also applied to new registrations [16].

Research has focused on studying the use of alternative/renewable fuels for use within internal combustion engines, partly focusing on influencing the $CO_2$ release, but also on emissions as a result of different combustion characteristics. Chemistry differs, which affects parameters such as the octane number, energy density, among others. Also, producing fuels from renewable feedstock would result in crops acting as a sink, ultimately lowering atmospheric $CO_2$ [17]. There is of course a more nuanced picture to be given, but this is not within the scope of this thesis.

## 1.3 Euro 7

Stricter limits and testing regarding emissions are expected in the upcoming Euro 7 standard, expected to be adopted by the European Commission by the fourth quarter of 2021 [18]. Building up on the existing emission limits set by Euro 6d, Euro 7 aims to impose the ambition of 'Zero-emission' on vehicles. Many proposals and ideas that have been presented by Advisory Group on Vehicle Emission Standards (AGVES) and Association of Emissions Control by Catalyst (AECC) to further improve the emission standards with current innovative technologies will be briefly discussed below.

Few of the important points listed in the proposal of AECC [19] include,

1. Consideration to the combination of peak value and duration of emission events in addition to the average emission levels present in Euro 6d standards.
2. Ensuring emission fluctuations with operating/driving conditions such as the ambient condition and trip composition are taken into account.
3. Limits on the emissions must be derived from air quality and individual exposure requirements rather than the type of powertrain to avoid market distortion and allow free consumer choice.
4. Irrespective of the type of vehicle, the emission control system might need to have:
    - Close-coupled catalysts for cold-start;
    - Underfloor catalysts for high speed/load;
    - Sufficient total catalyst and filter volume to account for peak engine out emissions.

At the AGVES meetings conducted on 27 October 2020 [20], different ideas and suggestions for Euro 7 include,

1. Extending the ambient temperatures from (-7°C - +35°C) to (-10°C - +40°C) introducing harsher operating conditions.
2. Durability of the exhaust after-treatment systems (EATS) to be increased from 160,000 km to 240,000 km for more robustness.

3. Shortening the trip distance from 16km to less than 5km. Given the fact that cold starts contribute to about 80% of the emissions, the emissions limits on carbon monoxide ($CO$), nitrogen oxides ($NO_x$), particulate matter (PM) and particle number (PN) can be considered to be shortened by a factor of 3.
4. Removing the limits on maximum altitude, average speed and positive elevation gain introduces many more operating conditions for which the emission limits needs to be satisfied.
5. Introduction of new pollutants that include $NH_3$, $N_2O$, $CH_4$ and brake emissions.

Current technologies that may help in complying with Euro 7 legislation are listed below:

1. Pre-heated catalysts could significantly reduce emissions in cold-starts.
2. High gasoline particulate filter (GPF) filtration efficiency from clean state.
3. Accurate combustion control ($\lambda = 1$ across all operating points)
4. Possible catalyst size increase to address higher engine power events, resulting in longer residence times for exhaust gases.

A follow-up meeting was held 8 April 2021 [18]. Challenges recognized for cold-starting, gave rise to an emission budget concept, covering for shorter trips. This included:

- Within the first 16km, a budget of $x$ mg is given, depending on species being considered. When transitioning into normal conditions, the usual $y$ mg/km applies, depending on species.

Additionally, revised emission limit scenarios were presented. Alongside $NO_x$, CO, HC and particulates; ammonia ($NH_3$) and nitrous oxides ($N_2O$) were introduced. THC is a bit more specific, and includes separated limits for methane, non-methane organic gases as well as formaldehyde.

To summarize the statements above; it is expected that meeting Euro 7 limits will be extremely challenging as well as demanding, and hence requires high effort on the development side.

## 1.4 Legacy Thesis

This thesis is a continuation of an older thesis, carried out by students from Linköping University at Volvo Cars in 2019, entitled *Model Based Catalyst Control* [8].

The goal of that thesis was to get a deeper understanding of the dynamic behaviour of a three-way catalytic converter. Thesis workers built a one dimensional discrete mathematical model of the TWC consisting of two bricks virtually partitioned into 5 equal slices. A model-based control structure was implemented, boiling down to a choice of 5 PID-controllers, one for controlling the oxygen buffer level (OBL) of each slice of the TWC.

The model was built in Simulink, using Forward Euler-method to solve the differential equations. This allows for a direct translation to Target Link, a tool used to

generate C-code for running software in the Engine Control Unit (ECU). Simulink also houses a pedagogical value, as it visualizes how sub-systems and signals interconnect with each other, making it easier to get an understanding of the model. An example can be seen in Fig. 1.2, displaying one of the sub-systems where the model dynamics is captured for a single slice of the catalyst.

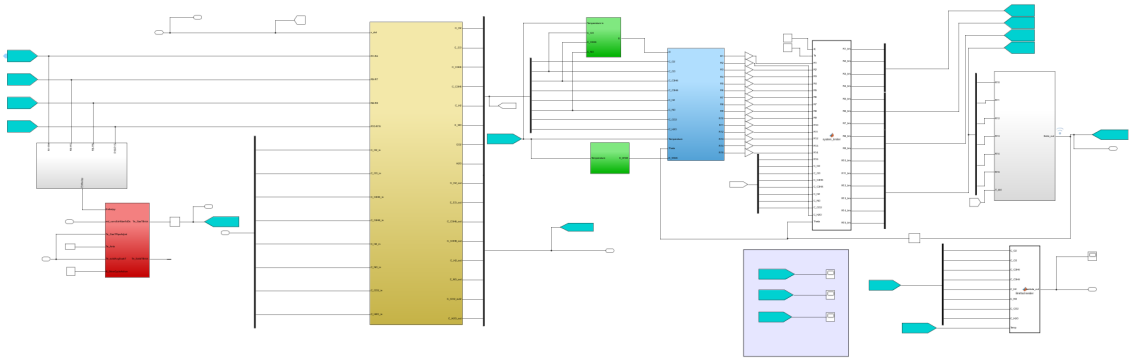

**Figure 1.2:** An overview of a Simulink sub-system

Some aspects of the SIMULINK model had been hard coded such as each slice requiring a single sub-system which made it difficult to expand or condense the model. Moreover, the model became unstable at certain operating points primarily due to the constant sampling time, $T_s = 0.01s$, which also made the simulations considerably long.

In order to decrease simulation time of the model, more sophisticated differential equation solvers, such as *ode15s*, could be used since they allow variable step sizes that depend on state gradients. This opens up for faster, more accurate and stable solutions and this would be a key improvement in comparison to the Euler Forward-method used in SIMULINK. By having faster simulations, it would then be feasible to run an optimization algorithm on collected test-bench data to determine model parameters.

As previously mentioned, the current model lacks calibration. Parameters proposed in a paper by Ramanathan et. al [4] has been used, together with 15 reactions to summarize events occurring within the TWC. Ideally, it would be beneficial to know the rate of each individual reaction. However, many species will fight over the same reactants, making it difficult to tell to what extent a species does consume a reactant. It is not possible to measure reaction rates, so one has to rely on a model to obtain that information. Obtaining representative data is challenging, and adequate experiment design is essential for success.

The focus of the legacy thesis was mainly put on Target Link compatibility as well as the controller implementation, leaving model calibration and validation as future work. Authors listed a number of points that were either out of scope or omitted due to time restrictions, which could enhance the model in a future thesis. These will be briefly discussed along with the scope of this thesis.

## 1.5 Scope

MATLAB script based modelling was chosen in place of SIMULINK for this thesis because it was no longer necessary for the model to be compatible with Target Link and the ECU. MATLAB is considered a simpler environment for model building, hence the choice. Designing a new controller is still possible, along with refining the already proposed PID-design to work for a broader range of operating conditions and tunings. It was decided though, that the prime goal of this thesis should be to refine the workings inside the catalyst, rather than implementing a controller.

To do this, collecting data is of prime interest. Experiments will include tests on catalyst of different lengths with the same specification. If a reference catalyst of 70mm is considered, using shortened variants of 30mm and 15mm will be able illustrate a detail that 70mm alone cannot.

A gradient based optimization will be used to search for the optimal kinetic parameters that closely match the collected emission data. In MATLAB, *lsqnonlin* function is used to solve for the non-linear least-squares problem, where comparisons between experimental- and model emissions data are used to find optimal tuning.

The highlighted activities are summarized as:

1. Update model from SIMULINK to MATLAB scripts
2. Perform relevant experiments and collect data
3. Perform post-data processing
4. Optimize for the kinetic parameters
5. Validate the model using other experiments

# 2
# Theory

In this section, a basic understanding of the engine and the exhaust after-treatment system is covered along with a literature survey into the work done regarding the modelling and control of three-way catalytic converters.

## 2.1 Engine Combustion

It is in theory possible to calculate the amount of air required to fully combust a given quantity of fuel. This is referred to as the stoichiometric air-to-fuel (AFR) ratio, and is defined as the fraction of air mass to fuel mass. The procedure uses two assumptions: i) Air is modelled as a mixture of 21% $O_2$ and 79 % $N_2$. ii) The fuel can be approximated as one common hydrocarbon, $C_aH_b$ [7].

If assumption i) above is applied, it would mean that for each mole of oxygen, there exists 3.773 moles of nitrogen. By balancing the combustion reaction,

$$C_aH_b + (a + \frac{b}{4})(O_2 + 3.773N_2) \rightarrow aCO_2 + \frac{b}{2}H_2O + 3.773(a + \frac{b}{4})N_2 \tag{2.1}$$

it is possible to calculate the theoretical $AFR_t$ using molecular masses via the relation

$$AFR_t = \frac{(1 + \frac{b}{4}(16 * 2 + 3.773 * 2 * 14))}{12a + b} \tag{2.2}$$

The theoretical AFR value will depend on the ratio between hydrogen and carbon ($\frac{a}{b}$), but a typical AFR value for gasoline is 14.7. The quotient between the theoretical $AFR_t$ and the actual $AFR_a$ is referred to as lambda ($\lambda$),

$$\lambda = \frac{AFR_a}{AFR_t} \tag{2.3}$$

where $\lambda$ indicates deviation from stoichiometry. When excess air is used, $\lambda > 1$ and the mixture is referred to as lean. When excess fuel is used, $\lambda < 1$ and the mixture is referred to as rich. Ideally, $\lambda = 1$ is desirable and this would result in the highest conversion of the pollutants [21].

The mass flow through an engine is a function of the engine speed, $N_{eng}$, and/or the load, $m_{load}$. Engine speeds and loads are represented by revolutions per minute (RPM) and milligram air per inlet stroke (mg/str) respectively. The relation is summarized in Eq. 2.4 below.

$$\dot{m} = 2 * \frac{N_{eng}}{60} * \frac{m_{load}}{1000} \left[\frac{g}{s}\right] \tag{2.4}$$

$N_{eng}$ and $m_{load}$ are divided by 60 and 1000 in order to convert the units from minutes to seconds and milligrams to grams respectively. Finally, the flow is multiplied by 2 to take into account the number of cylinders that perform the air intake/compression stroke simultaneously, which is 2 for a 4 cylinder engine.

## 2.2 Three-Way Catalytic Converter

As a result of incomplete combustion, exhaust aftertreatment systems are equipped with catalytic converters, driving unfinished reactions closer to completion. SI engines produce harmful pollutants such as CO, HC and $NO_x$, with amounts depending on the operating point.

An important message is that $NO_x$ is an abbreviation of nitrous oxides, where $x$ denotes either 1 or 2. Hence, $NO_x$ is an acronym for NO and $NO_2$. SI engines produce a negligable amount of $NO_2$; Heywood suggests that the ratio of $NO_2$/NO peaks at 2% running $\lambda = 1.2$ [7]. All possible $NO_2$ production will be neglected in this thesis, meaning that it will be assumed that $NO_x$ at all times is represented by the NO emissions.

Delving a bit deeper into the catalyst once more, a simplistic way to describe the workings inside the catalyst can be summarized in the reaction scheme below [7]:

*Oxidation:*

$$CO + \frac{1}{2}O_2 \longrightarrow CO_2 \tag{2.5}$$

$$H_yC_x + (\frac{y}{4} + x)O_2 \longrightarrow \frac{y}{2}H_2O + xCO_2 \tag{2.6}$$

*Reduction:*

$$NO + CO \longrightarrow \frac{1}{2}N_2 + CO_2 \tag{2.7}$$

$$(x + \frac{y}{2})NO + H_yC_x \longrightarrow (\frac{x + \frac{y}{2}}{2})N_2 + xCO_2 + \frac{y}{2}H_2O \tag{2.8}$$

$$NO + H_2 \longrightarrow \frac{1}{2}N_2 + H_2O \tag{2.9}$$

CO and HC get oxidized to produce $CO_2$ and $H_2O$. NO can be reduced via either CO, HC or $H_2$, producing the harmless gases such as $N_2$ along with $CO_2$ and $H_2O$. An illustration can be seen in Fig. 2.1 below.

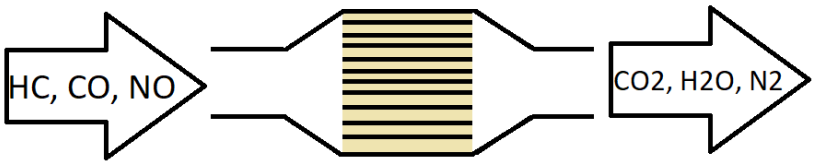


**Figure 2.1:** A schematic of the TWC - Pollutants HC, CO and NO enter, $CO_2$, $H_2O$ and $N_2$ leave.

The TWC consists of a number of parallel channels, resembling a honeycomb structure, to maximize the surface area for reactions to take place [22], see Fig. 2.2 below.

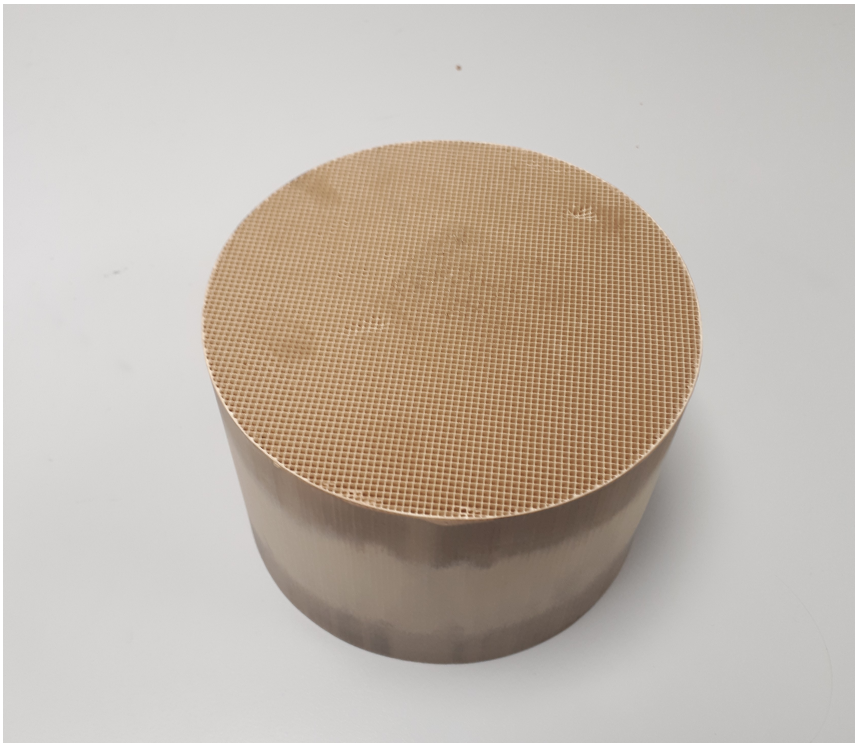

**Figure 2.2:** A ceramic monolith - displaying the characteristic honeycomb pattern

The channel walls are coated with a washcoat, which is a porous ceramic mainly consisting of $\gamma Al_2O_3$. Cerium/Zirconium mixed oxides are added as oxygen storage promoters and thermal stabilizers [6],[22],[23]. Noble metals such as Palladium (Pd), Platinum (Pt) and Rhodium (Rh) are dispersed on the washcoat as catalytic active components, where the ratio influences the conversion efficiency of the catalyst. Rood et al. suggests that Pt and Pd covers oxidation, while Rh covers reduction [24]. This binary reasoning is likely not the complete picture, as the authors in the above mentioned paper refer to research suggesting that Pd also can be attributed to NO removal.

Having a porous washcoat allows for a large active surface area for reactions to occur [6]. The Ceria in the washcoat constitute of the oxygen buffer due to it's ability to store oxygen. Due to the fluctuations between rich and lean phase in a bang-bang setting, incorporation of oxygen storage and release acts like a safety net, such that species conversion is not affected by an increased $\lambda$-window [7].

### 2.2.1 Catalyst Deactivation

Aging effects such as poisoning, sintering, as well as masking and fouling influences the number of active catalytic sites. A direct consequence of this, is worsened oxygen storage capabilities. These mechanisms will be described in more detail below.

Aging has been shown to influence catalyst behaviour. As described and shown by Auckenthaler [6], aging primarily affects the water gas-shift (WGS) and steam reforming (SR) reactions

$$\mathrm{CO} + \mathrm{H_2O} \rightleftharpoons \mathrm{CO_2} + \mathrm{H_2} \tag{2.10}$$

$$C_3H_6 + 3H_2O \longrightarrow 3CO + 6H_2 \tag{2.11}$$

This results in aged catalyst to operate further away from equilibrium. As the reactions display, hydrogen production will then decline. If the same conditions (operating point, temperature profile within the catalyst) could be recreated both pre- and post deactivation, this reasoning suggests a potential leakage increase of hydrocarbons and THC as a result of the aging effects.

Moreover, in aged catalysts, Auckenthaler observed an increase in $CO_2$ on the lean operations. This was not expected as lean operation would correlate to low amounts of CO and THC, as well as repressed WGS and SR reactions. Therefore, it was believed that the aged catalyst displayed an increased storage of carbonaceous species, that were oxidized while running lean.

#### 2.2.1.1 Poisoning

Poisoning is a form of deactivation of active catalytic sites, and can be induced by contaminants in the fuel, such as sulphur. Poisoning primarily impacts the kinetics and can be counter-balanced by running at elevated temperatures to achieve a desired activity level [7].

As an example, sulphur can exit the exhaust as either $SO_2$ or $H_2S$. It has been shown that sulphur poisoning is mainly a problem on the rich side, where it hinders the water-gas shift and steam reforming reactions.

These reactions play a key role in mitigating CO and HC emissions. On lean side, this is not as crucial, as HC and CO will be exposed to an abundance of $O_2$ [25]. However; this is not a major problem in this thesis, as sulphur content in gasoline has decreased over time. It is believed that the influence of sulphur chemistry is negligible and as a consequence, will not be accounted for in the kinetic model.

#### 2.2.1.2 Sintering

Sintering is a process also referred to as thermal deactivation. As an effect of high temperatures, active noble metal sites migrate and coalesce, ultimately forming larger, but fewer available sites for reaction. Similar to poisoning, sintering primarily impacts kinetics [7].

Sintering may also influence porosity. The $\gamma$-alumina can at high temperatures transform to either $\theta$- or $\alpha$-alumina, which are phases with lower surface and pore area, resulting in an encapsulation such that noble metal surfaces become inaccessible for reactants. Adding a stabilizer, such as $ZrO_2$ can be used to mitigate the effect [26].

#### 2.2.1.3 Masking and fouling

Masking and fouling is a process where carbon compounds attach to the catalytic surface, hindering catalytic activity [26]. Carbon originates from heavy, unburnt hydrocarbons, as well as oil additives. Corrosion scaling and dust is also a cause of decreased activity. Masking and fouling causes both loss of active sites as well as blocking of pores. An efficiency curve displaying conversion versus temperature will hence be both shifted in temperature and also exhibit a reduced slope [7].

## 2.3 $\lambda$-sensors

In order to control the operating point of the engine at stoichiometry ($\lambda = 1$) to minimize emissions of HC, CO and $NO_x$, control system needs to make use of the available oxygen content [7]. This information is obtained via oxygen sensors, usually referred to as $\lambda$-sensors. There are two different types namely, linear (wide-range) and binary (switch-type) lambda sensor.

### 2.3.1 Binary type $\lambda$-sensor

Binary type $\lambda$-sensors, as the name suggests, gives an indication about whether the gas exhaust is either in a lean or rich state through a voltage signal that is highly sensitive around stoichiometry. See Fig. 2.3 for visuals.

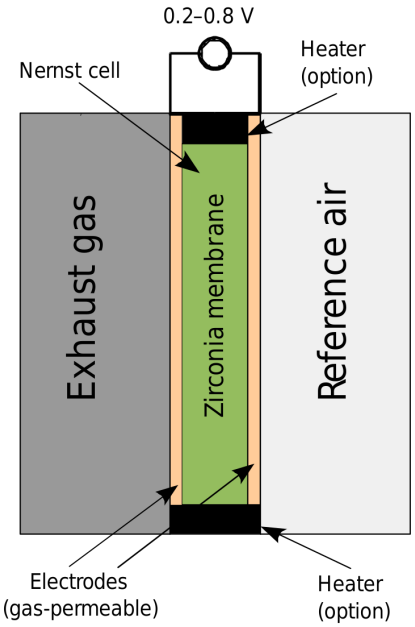


**Figure 2.3:** Schematic of a binary type $\lambda$-sensor [2]

The sensor is essentially a galvanic cell whose electrolyte is a solid, such as yttria ($Y_2O_3$)-stabilized zirconia ($ZrO_2$). The electrolyte separates the two gas chambers that belong to the exhaust and ambient, where the ambient air is used as a reference gas [7].

On the region exposed to the exhaust gases, a platinum electrode is used. It serves as a cathode (the side of the cell in which electrons enter the electrolyte), driving the exhaust gas composition to a chemical equilibrium. A gradient between adsorbed $O_2$ on the electrode and $O_2$-ions on the electrolyte arises, causing migration/donation of electrons to or from the electrode to the electrolyte, with respect to the anode/cathode. Similar process takes place at the anode and the resulting current generates an electric potential, which correlates to the oxygen content in the exhaust [6].

Not only $O_2$ drives the exhaust gas to chemical equilibrium, but also reducing species such as $H_2$, CO or HC. This makes the name $O_2$-sensor misleading, as reducing species also makes an influence on the output voltage. It has been shown that during rich operation, coking and hydrocarbon coverage on the catalytic sites can hinder the water-gas shift reaction. When using aged catalysts, the ratio of $H_2$ and CO/HC will be distorted, in comparison of using a fresh catalyst. This will alter the information the lambda sensor provides [6].

### 2.3.2 Linear type $\lambda$-sensor

Linear or wide-range $\lambda$-sensors are sensitive across a larger $\lambda$ range, in contrast to the binary type which is highly sensitive at close-to-stoichiometric region. The sensor houses two cells: An oxygen pump cell and a Nernst cell, see Fig. 2.4.

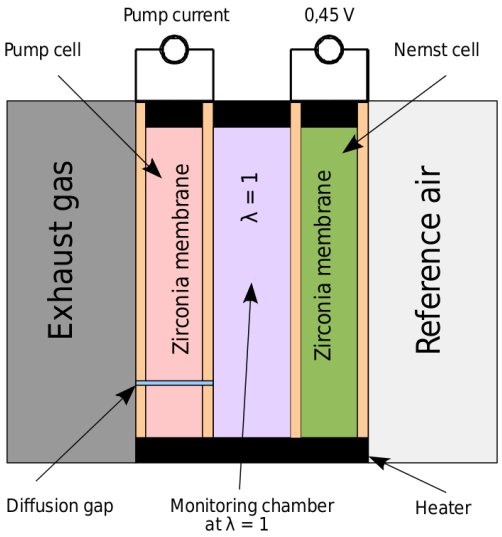


**Figure 2.4:** Schematic of a linear type $\lambda$-sensor[3]

These work similar to what was described in the binary $\lambda$ sensor-section above. These cells are separated by a diffusion gap, in which the exhaust gas mixture is introduced. The oxygen pump transfers electrons to or from the diffusion gap to bring a non-stoichiometric mixture into equilibrium. The Nernst cell is able to detect this relative to a reference ambient air cell. The voltage driving the current is measured and gives a more resolute indication of the oxygen content, in contrast to the binary sensor [7].

### 2.3.3 Analytical $\lambda$ calculations

A theoretical way to calculate $\lambda$ can be found in [27] and [6]. By holding information on what the current mole fraction of each species are, denoted $y_x$, it is possible to calculate a $\lambda$-value given experimental data:

$$\lambda = \frac{2y_{O_2} + y_{NO} + y_{CO} + 2y_{CO_2} + y_{H_2O}}{2y_{CO} + y_{H_2} + (2a + \frac{b}{2})y_{C_aH_b} + 2y_{CO_2} + y_{H_2O}} \tag{2.12}$$

Another approach is the so called Brettschneider-$\lambda$ [28], introduced by Dr. Johannes Brettschneider at Bosch which is similar to the above mentioned formula, but has in our studies shown to work better

$$\lambda = \frac{y_{CO_2} + \frac{y_{CO}}{2} + y_{O_2} + \frac{y_{NO}}{2} + (\frac{H_{CV}}{4}\frac{3.5}{3.5+\frac{y_{CO}}{y_{CO_2}}} - \frac{O_{CV}}{2})(y_{CO} + y_{CO_2})}{(1 + \frac{H_{CV}}{4} - \frac{O_{CV}}{2})(y_{CO_2} + y_{CO} + n * y_{HC})} \tag{2.13}$$

where $H_{CV}$ and $O_{CV}$ are the atomic ratios of hydrogen and oxygen to carbon in the fuel. The variable $n$ is an integer variable to account for the number of carbon atoms in the selected HC molecule.

## 2.4 Literature Review

### 2.4.1 Models

Modelling and control of a TWC has been covered extensively in literature. One of the most common models found are the one-dimensional two-phase models [4], [29],[30],[31]. which consider one dimensional (time series) model that represent the solid and gas phase dynamics individually.

As stated by Joshi, even though it is possible for computers to solve detailed, sophisticated models considering coupled non-linear partial differential equations with multi spatial-coordinates, these are highly limited when it comes to real-time applications [29]. By making axial averaging over the catalyst length, the axial coordinate dependency can be neglected, and hence be left with an ordinary differential equation (ODE), dependent only on time [22].

In two succeeding publications, a 0D axially averaged TWC-model was compared to a 1D model to study the limitations of the low-dimensional 0D model [22],[30]. The updated 1D-model was similar to its legacy, but without the axial averaging. As a consequence, the follow up publication considered a set of partial differential equations (PDE), which were solved both in time and space. The conclusion was that axial gradients in temperature and oxygen storage profile could not be neglected during cold starts or fast lean to rich cycling as well as sudden changes in inlet conditions [30].

### 2.4.2 Mass Transfer Effects

Santos & Costa [32] make a detailed study on the effects of external and internal mass transfer. External mass transfer relates to exhaust gases diffusing onto the washcoat while, internal mass transfer corresponds to the internal pore diffusion inside the washcoat, where they adsorb onto an active catalytic site and react to form products. These products are then reversibly brought back to the bulk phase via desorption.

A number of reports, including Kumar and Ramanathan [22],[30],[4], considers mass and heat transfer via use of correlations, where Sherwood number (Sh) and Nusselt number (Nu) correlations are used. These dimensionless numbers can be used as an approximation for transport gradients. By considering an effective heat or mass transfer coefficient, transverse/radial behaviour can be eliminated, decreasing that particular space coordinate [33].

### 2.4.3 Chemical Reactions

How many reactions should be considered? Well, that depends on the objective. Auckenthaler [6] uses a reaction scheme based on the works of Jobson et. al [34] where sulphur poisoning effects have been omitted. This results in a reaction scheme with a total number of 15 reactions, using Eley-Rideal and Langmuir-Hinshelwood kinetics. The reaction scheme makes a distinction between noble metal sites and Ceria. The Ceria is simply used for oxygen storage and release, while the noble metal accounts for adsorption of $O_2$, CO, $H_2$, $NO$ and $C_3H_6$ on the catalytic surface. CO, $H_2$ and $C_3H_6$ can be oxidized and $NO$ can be reduced. Oxygen from $O_2$ as well as $H_2O$ can be stored on Ceria, and $C_3H_6$, CO and $H_2$ can reduce the Ceria.

Ramanathan [4] uses a different approach, but the reaction scheme still shows some similarities. The reactions are split into four sub-categories, which are

1. Oxidation Reactions
2. NO Reductions
3. Water-Gas and Steam Reforming
4. Ceria Reactions

In this paper, no distinction between noble metal and Ceria is made. The available catalytic sites are embedded in the kinetics, which are of Langmuir-Hinshelwood type. The intermediate step covered in Auckenthaler, where the species has to first attach to a catalytic site, is not considered in Ramanathan.

There is more nuance to NO reductions, which include reaction with CO, $C_3H_6$ and $H_2$. The Ceria storage and release are similar between papers, but with the difference that in Auckenthaler, $H_2O$ can oxidize Ceria, as opposed to NO in Ramanathan.

Auckenthaler considers one hydrocarbon, which is $C_3H_6$ and Ramanathan considers $C_3H_6$ and $C_3H_8$. According to Bäroth [35], the exhaust gas hydrocarbon composition includes aromatics, paraffins, olefins, alcohols and aldehydes. In order to capture this diversity, a modelling choice is to consider two hydrocarbon species, such as propane ($C_3H_6$) and propene ($C_3H_8$) to cover fast and slow oxidizing hydrocarbons [36]. In Pontikakis, the hydrocarbon mixture was split into 85% fast, and 15% slow. In the legacy thesis [8] the split was instead 67% and 33 %.

Another strategy is to lump oxidizing species and reducing species [27],[22],[30] into separate categories. Species such as $H_2$, CO and HC can take oxygen from other reactants and reduce them; hence the term reducing agent. Kumar also considers $NH_3$ as a reducing species [22],[30]. On the contrary, $O_2$, NO and $NO_2$ can give oxygen to other reactants; hence the term oxidizing agent. In both the papers, a third category is referred to as oxidized reducing agents, which is $CO_2$ and $H_2O$. The lumping reduces the number of reaction to its minimum, resulting in a total of three chemical reactions. By for instance referring to oxidizing agents as OA, reducing agents as RA, oxidized reducing agents as ORA as well as oxidized and reduced Ceria as $Ce_{Ox}$ and $Ce_{Red}$, we can illustrate this as:

$$\mathrm{Ce_{Red}} + \mathrm{OA} \rightleftharpoons \mathrm{Ce_{Ox}} \tag{2.14}$$
$$\mathrm{Ce_{Ox}} + \mathrm{RA} \rightleftharpoons \mathrm{Ce_{Red}} + \mathrm{ORA} \tag{2.15}$$
$$\mathrm{OA} + \mathrm{RA} \rightleftharpoons \mathrm{ORA} \tag{2.16}$$

Looking at Reaction 2.14, an oxidizing agent OA can oxidize the washcoat Ceria. Having oxidized the Ceria, Reaction 2.15 can occur and the reducing agents can be oxidized to $CO_2$ and $H_2O$, leaving Ceria in its reduced state. Finally, Reaction 2.16 considers direct catalytic activity via the noble metal.

The main advantage of lumping is two reasons. By considering only three main reactions, Kumar can keep the optimization parameters at a minimum, only having to consider three pre-exponential factors and three activation energies. Lumping has an obvious major drawback, which is of course that detail on specific species can't be studied. In a control perspective, this is considered powerful, as less calculations would be necessary while still keeping the essential behavior in the model [22].

### 2.4.4 Oxygen Storage

Oxygen storage dynamics has been considered in many papers [27], [37], [4], [22], [8], and the idea can be summarized in Eq. 2.17

$$\frac{d\Theta}{dt} = C(r_{store} - r_{release}) \tag{2.17}$$

where $\frac{d\Theta}{dt}$ is rate of change of the oxygen storage capacity and $r_x$ denotes the rates of storage and release, respectively. By looking at a proposed reaction scheme involving Ceria, the reactions involving storage are lumped into $r_{store}$, while the release reactions are lumped into $r_{release}$. The rate of change is $\frac{d\Theta}{dt}$ integrated to obtain the storage level.

In catalyst specifications, a theoretical oxygen storage capacity in weight unit per volume unit is denoted. The factor $C$ simply normalizes this to values in between 0 and 1, where 0 means empty and 1 means fully saturated with oxygen. The variable $\Theta$ will for further reference be referred to as the oxygen buffer level (OBL).

### 2.4.5 Langmuir-Hinshelwood Kinetics

Langmuir-Hinshelwood kinetics in TWC modelling has been covered in literature [38],[4],[39]. Langmuir-Hinshelwood type kinetics are used in heterogenous catalysis, and the mechanism considers reaction between molecular species that has been adsorbed onto a catalytic surface [40].

The first appereance of this type of kinetics can be found in Voltz from 1973 [41]. The scope of that paper was to determine the kinetics of CO and $C_3H_6$ on a Pt-Al catalyst. The data acquired was used to fit a variety of reaction mechanisms and kinetic rate equations. An optimization routine was executed to find to best parameters for the fit. The following rate equations $r_x$ were used

$$-r_{CO} = \frac{k_{r_1}[CO][O_2]}{R} \tag{2.18}$$

$$-r_{C_3H_6} = \frac{k_{r_2}[C_3H_6][O_2]}{R} \tag{2.19}$$

where R is the inhibition factor, which accounts for inhibition effects of CO, $C_3H_6$ and NO on the catalyst. Brackets denote concentration of species, and $k_{r_x}$ is a kinetic parameter. The inhibition factor includes chemisorption of CO and $C_3H_6$, adsorption of NO and a fitting term for CO and $C_3H_6$ at higher concentrations, relating to the lack of $O_2$ able to adsorb to the catalyst surface [41]. Chemisorption is short for chemical adsorption, where molecules or atoms usually covalently bond onto the substrate/catalyst [40]. The equations presented in Voltz paper has been used as a foundation for subsequent publications using Langmuir-Hinshelwood kinetics.

### 2.4.6 Control

In a traditional control system with bang-bang characteristics, controlling the theoretical AFR close to stoichiometry (by $\lambda$-sensor feedback) is difficult in practice. This is partly due to randomness in engine variations, but also due to the deliberate oscillations in between lean and rich phases. By incorporating oxygen storage and Ceria into the washcoat, the fluctations in between rich and lean can be handled more efficiently, and increases the window in which emissions are controlled [7].

A model-based control strategy involves controlling the OBL, which is considered key and presumably would allow tighter control on breakthrough emissions [42]. A way to control the OBL is presented in the just cited paper, using a PI-controller with anti-windup.

A cascaded structure is used using an inner- and an outer loop, where the inner-loop produces a set point for the outer loop. The purpose of the inner loop is to maintain AFR close to reference. Information from a post-catalyst binary $\lambda$-sensor is used as a set-point for the outer loop, with the purpose of modifying the lambda-reference. In the outer loop, a difference between predicted (based on a model) and desired OBL is calculated, and fed via the PI-controller which translates that difference to a control signal giving the adequate AFR. The controller is calibrated using the Ziegler-Nichols method, and is tuned via a look-up table based on different engine speeds and loads [42].

The proposed control strategy in the legacy thesis considers a PID-design for OBL control of each individual slice. In this approach, each slice is assigned a PID-controller, where only one controller is active at each time instance. The last slice

is to be filled first, and then next to last, and so on. This design is limited to all slices having the same OBL set-point. The final control signal is obtained by adding an additional feed forwarded 1 to the PID-controller, to account for the nature of wanting the AFR being close to stoichiometry. The choice of tuning is important, since this affects the OBL which in turn, affects the tailpipe emissions. The tunings are as of now ad-hoc, and depend on the three different exhaust gas mass-flow settings [8].

## 2.5 Previous Work

As this thesis is a continuation, it is relevant to briefly overview the results of the legacy thesis [8]. A model was developed in Simulink, consisting of a two brick TWC, virtually partitioned into five slices. Brick one was discretized into three slices. Brick two was discretized into two slices.

An engine out model was used to determine exhaust gas concentration. This model takes an engine operating point (including engine speeds, mass flows, mass load and $\lambda$ as inputs), and uses look-up tables acquired from experiments to make a translation from this operating point to actual emissions. These emissions are referred to as raw emissions, for future reference.

The raw emissions enter the TWC, and 15 different reactions were modelled using Langmuir-Hinshelwood type kinetics to account for NO reduction and CO and HC oxidation along with oxygen storage.

A species balance solver was used, to determine how mass convection and reactions affected how species concentrations changed within each individual slice. All individual components will be described in more detail as follows.

### 2.5.1 Reactions and Kinetic Model

A total number of 15 reactions were modelled which can be categorized into oxidation, NO reduction, water-gas shift and steam reforming, oxygen storage and oxygen release; see below.
Oxidation:

$$1 : CO + \frac{1}{2}O_2 \rightarrow CO_2 \tag{2.20}$$

$$2 : C_3H_6 + \frac{9}{2}O_2 \rightarrow 3CO_2 + 3H_2O \tag{2.21}$$

$$3 : C_3H_8 + 5O_2 \rightarrow 3CO_2 + 4H_2O \tag{2.22}$$

$$4 : H_2 + \frac{1}{2}O_2 \rightarrow H_2O \tag{2.23}$$

$NO_x$ reduction:

$$5 : CO + NO \rightarrow CO_2 + \frac{1}{2}N_2 \tag{2.24}$$

$$6 : C_3H_6 + 9NO \rightarrow 3CO_2 + 3H_2O + \frac{9}{2}N_2 \tag{2.25}$$

$$7 : H_2 + NO \rightarrow H_2O + \frac{1}{2}N_2 \tag{2.26}$$

Water-gas shift and steam reforming:

$$8 : CO + H_2O \rightarrow CO_2 + H_2 \tag{2.27}$$

$$9 : C_3H_6 + 3H_2O \rightarrow 3CO + 6H_2 \tag{2.28}$$

Oxygen storage:

$$10 : 2Ce_2O_3 + O_2 \rightarrow 4CeO_2 \tag{2.29}$$

$$11 : Ce_2O_3 + NO \rightarrow 2CeO_2 + \frac{1}{2}N_2 \tag{2.30}$$

Oxygen release:

$$12 : CO + 2CeO_2 \rightarrow Ce_2O_3 + CO_2 \tag{2.31}$$

$$13 : C_3H_6 + 18CeO_2 \rightarrow 9Ce_2O_3 + 3CO_2 + 3H_2O \tag{2.32}$$

$$14 : C_3H_8 + 20CeO_2 \rightarrow 10Ce_2O_3 + 3CO_2 + 4H_2O \tag{2.33}$$

$$15 : H_2 + 2CeO_2 \rightarrow Ce_2O_3 + H_2O \tag{2.34}$$

The reaction scheme was found in Ramanathan et. al [4] where a slight modification was made on Eqs. 2.32 and 2.33, to circumvent control problems. The kinetic model was also found in this paper, which considers Langmuir-Hinshelwood type kinetics on the following generic form: Reaction rate = (Kinetic parameter * Driving force)/Resistance. In mathematical terms, this can be expressed as

$$R_i = \frac{k_i \prod C_j}{G} \tag{2.35}$$

where $i \, \epsilon \, R$, which corresponds to reaction $i$ within the reaction set $R$. $\prod C_j$ is the product of reactant concentrations pertaining to the given reaction. The kinetic parameter, $k_i$, is determined by the Arrhenius law,

$$k_i = A_i e^{\left(\frac{-E_i}{R_g T_g}\right)} \tag{2.36}$$

where $A_i$ is the pre-exponential factor, $E_i$ activation energy, $R_g$ the ideal gas constant and $T_g$ the gas phase temperature. G is the inhibition term, which takes CO and $C_3H_6$ chemisorption, as well as NO adsorption into account [41]. The kinetic parameter upper case $K_i$ is used to calculate the inhibition factor

$$G = (1 + K_1C_{CO} + K_2C_{C_3H_6})^2(1 + K_3C_{CO}^2C_{C_3H_6}^2)(1 + K_4C_{NO}) \tag{2.37}$$

where $K_i$ is calculated via

$$K_i = k_{i,G} e^{\left(-\frac{E_{i,G}}{T_s}\right)} \tag{2.38}$$

where $k_{i,G}$ as well as $E_{i,G}$ are tuning parameters and $T_s$ is the surface temperature.

### 2.5.2 Some Exceptions to the General Formula

Even though the general Arrhenius behaviour is kept, the water-gas shift reaction shows a different driving force as is displayed in Eq. 2.39 below:

$$R_8 = \frac{k_{WGS} e^{\left(-\frac{E_8}{R_g T_s}\right)} (C_{CO} C_{H_2O} - \frac{C_{H_2} C_{CO_2}}{K_{WGS}})}{G} \tag{2.39}$$

Note that the driving force is expressed as a difference between reactant and product concentrations, giving some additional nuance to the mathematics. Additionally, he kinetic parameter $k_{WGS}$ is slightly different from the previous formula

$$k_{WGS} = e^{\left(-\frac{\Delta G_{WGS}}{R_g T_s}\right)} \tag{2.40}$$

where a polynomial as function of surface temperature is used to determine the Gibbs free energy

$$\Delta G_{WGS} = -4.10 * 10^4 + 44.19 T_s - 5.55 * 10^{-3} T_s^2 \tag{2.41}$$

This polynome originates from the Chemical Properties Handbook [43], where it is suggested that the Gibbs free energy can be modelled using second order polynomials given tabular values for coefficients.

The reactions involving ceria are also different, depending on if it involves storage or release of oxygen

$$R_r = k_r e^{\left(-\frac{E_r}{R_g T_s}\right)} \Theta \tag{2.42}$$

$$R_s = k_s e^{\left(-\frac{E_s}{R_g T_s}\right)} (1 - \Theta) \tag{2.43}$$

where index $r$ and $s$ refer to release or storage, respectively. Note that an inhibition term is not included here, as these reactions do not rely on available noble metal sites. Variable $\Theta$ is the OBL, being 0 if empty or 1 if full. The rates are hence proportional to the number of available sites.

Calculating the OBL is done by integration of

$$\dot{\Theta} = \frac{V_{cat}}{\Theta_{den}} (4R_{10} + 2R_{11}) - (2R_{12} + 12R_{13} + 14R_{14} + 2R_{15}) \tag{2.44}$$

where $V_{cat}$ is the catalyst volume and $\Theta_{den}$ are the number of active noble metal sites of the catalyst. Reactions numbered 10 and 11 are storage reactions, while reactions 12-15 are release reactions.

### 2.5.3 Species Balances Solver

The species balance solver was modelled via the use of continuously stirred tank reactors (CSTR) in series, where each slice corresponds to a single CSTR. Mathematically, this can be phrased as follows:

$$\frac{dC_n}{dt} = \Delta CQ + \sum_{j\epsilon R} R_j \nu_j \tag{2.45}$$

$$\Delta C = C_{in} - C_{out} \tag{2.46}$$

$$Q = \frac{\dot{V}}{V} \tag{2.47}$$

The quotient $Q = \frac{\dot{V}}{V}$ is referred to as the space velocity, and can be viewed as an inverse time constant. It describes how many reactor volumes can be treated per a given time unit. In an ideal CSTR, mixing is perfect and instant, which results in the concentration $C_n$ of species $n$, immediately reaching the value $C_{out}$. Species can also be produced/consumed via reaction, which is reflected in the term $\sum_{j\epsilon R} R_j \nu_j$, where R is the reaction rate and $\nu_j$ is the stoichiometric coefficient of a species, see Section 2.5.1.

Due to instability issues in SIMULINK, this differential equation was split into two sub-equations, allowing for an explicit solver to calculate the concentration out of each slice.

$$C_n^* = \begin{cases} C_n + (C_{in} - C_n)T_s Q, & T_s Q < 1 \\ C_{in}, & otherwise \end{cases} \tag{2.48}$$

where $C_n^*$ refers to as a preliminary concentration. The subscript refers to the concentration going out of the slice, at the time instant $n$.

By multiplying the sampling time with the space velocity, a condition can be set as to give a limit when the flow is too fast for it to be meaningful to sample. In this case, this bound was set to 1. If this condition is not fulfilled, the preliminary concentration is set equal to the species concentration going into the slice.

The concentration going out at the next time instant $n+1$ of a slice can finally be calculated as follows

$$C_{n+1} = C_n^* + \sum_{j\epsilon R} R_j(C_n^*)\nu_j T_s \tag{2.49}$$

where the preliminary concentration out is modified by the rates of reaction. In a MATLAB-environment, stability issues is of no concern, meaning that Eq. 2.45 can be solved directly.

### 2.5.4 Summary and Relation to Literature

The model is hence a low-dimensional model, where the discretization method of slicing creates a semi-axial dimension, where each tank in series considers an averaged concentration, similar to Kumar [22]. The kinetic model is directly obtained from Ramanathan [4], along with parameters for activation energies, pre-exponential factors as well as inhibition terms. The choice of using 15 reactions can be justified by the desire to acquire as much information as possible of the workings within the catalyst. Lumping for instance, would make it impossible to make any conclusions on individual species.

This model considers only one common phase, in contrast to what has been found in the literature. The physical interpretation of having one phase, is that the mass transfer resistance is completely neglected. Species entering the catalyst will hence instantly diffuse to surface, being ready for reaction. This is of course not what is happening, as bulk molecules has to diffuse onto the surface, in order to react.

Santos and Costa [32],[23] distinguishes between two extreme cases: kinetically controlled and mass transfer controlled regions. Kinetics based on Arrhenius expressions show an exponential relation to temperature, whilst the mass transfer does not. It is known that for temperatures above light-off (a benchmark value defined as the point where 50% conversion of a species is found), the mass transfer will restrict the conversion. As mass transfer is not considered in the legacy model, the limitations imposed at temperatures above light-off will not be captured. This has to be kept in mind, when experimental results are analyzed.

# 3

# Methods

This section describes the instrumentation utilized and how the experiments were conducted. It also presents steps following for optimizing the model from the collected data and it's validation.

## 3.1 Experiment Setup

An illustration of the experimental setup including instrument locations are displayed in Fig. 3.1 below,

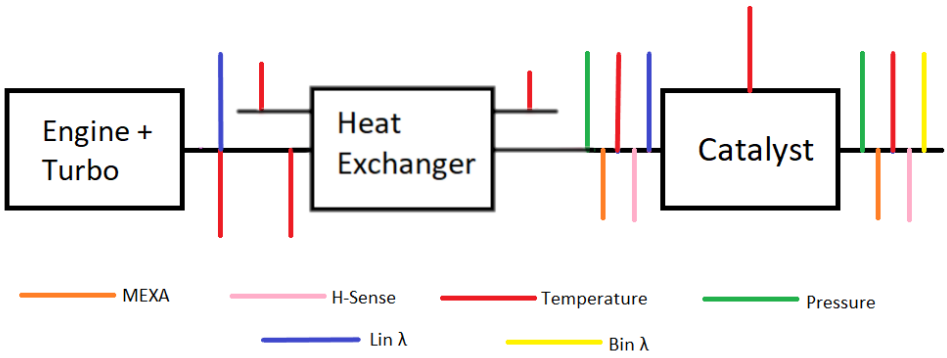


**Figure 3.1:** A schematic overview on sensor placements

Thermocouples are localized at four locations to measure the gas temperatures:

1. post turbo,
2. pre- and post HE exhaust line,
3. pre- and post HE air line,
4. Catalyst (varies depending on the catalyst length)

MEXA and $NO_x$-sensors are located at both pre- and post catalyst. Linear $\lambda$-sensors can be found post turbo and pre catalyst. A binary $\lambda$-sensor is installed post catalyst. H-Sense sensor has 2 channels at both pre- and post catalyst however, only one of the channels can be measured at a given time.

### 3.1.1 Engine + Turbo

A turbocharged spark-ignited gasoline engine was used as a means to produce emissions to be fed through the catalyst, see Table 3.1 for specifications.

**Table 3.1:** Engine specifications

| Name | VEP LP |
|---|---|
| No. of Cylinders | 4 |
| Displacement (cc) | 1969 |
| Compression Ratio | 12 |
| Injection Type | Direct-Injection |
| Turbocharged | Yes |

Using an engine allows for real emissions to be simulated but the flexibility on the composition of exhaust emissions is lost. On the other hand, a laboratory set-up enables the composition entering the catalyst to be controlled and in turn, the ability to isolate the chemical reactions. The tuning of various kinetic parameters becomes easier by separation of the chemical reactions, however the priorities of each reactions compared to one another may be lost. In Section 3.4, a method is devised to group a set of reactions to different regions in the experiment when using an engine.

Given numerous engine operating points, engine speeds were restricted to choices of 1500, 2250, 3000, 4000 and 4500 RPM, where 1500, 3000 and 4500 were the most common. Load was mostly set to 325 mg/str, while 390 mg/str was sometimes used; Load signifies the air mass injected during each intake stroke.

### 3.1.2 Heat Exchanger

The setup also included a heat exchanger (HE), to allow for manipulating the temperature dynamics of the gases entering the catalyst. This device acts as both a heater and a cooler, depending on its use in relation to the catalyst temperature profile. A schematic is displayed in Fig. 3.2.

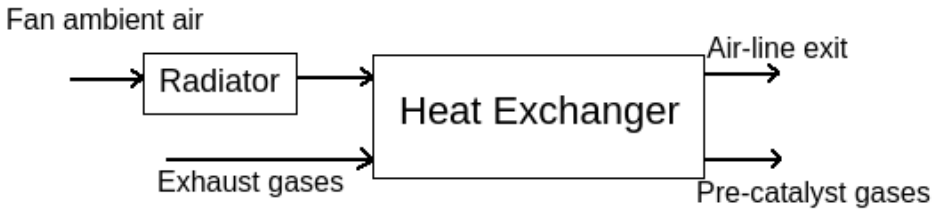


**Figure 3.2:** Schematic of the HE inside the rig

The exhaust and air lines are co-current, and was chosen over counter-current setup due to implementation ease within the test-rig. A fan connected prior to the inlet

port introduces air at a constant rate as the exchange medium. A thermal element/radiator controls the ambient air temperature between 24°C and 700°C. Fig. 3.3 illustrates the HE within the test-rig environment. The red and yellow lids are the inlet and outlet ports for air, respectively. Note the thick pipes of the exhaust line entering and exiting the HE.

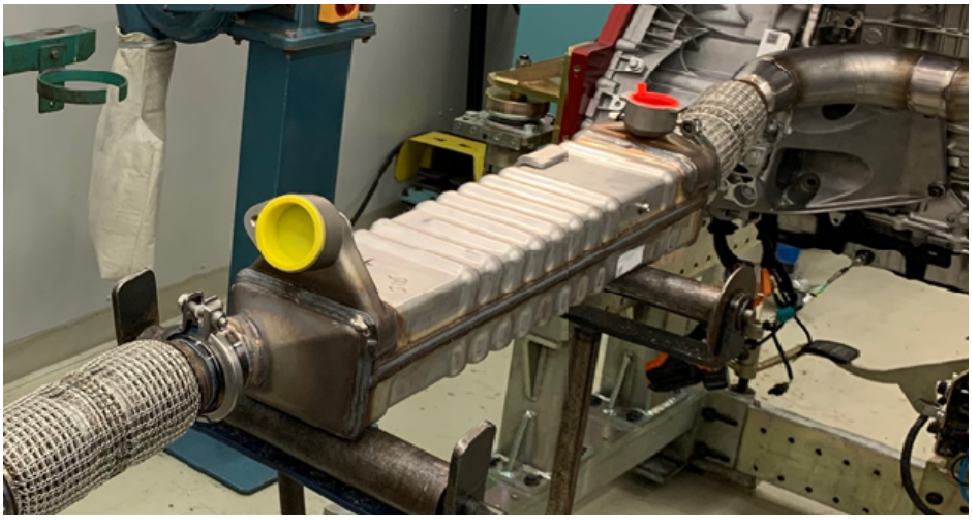

**Figure 3.3:** Display of the HE inside the rig

In Fig. 3.4, an illustration of the fan installed within the rig can be seen. The red circle depicts the inlet port into the HE. Note that, in the background, the HE is covered with thermofoil to reduce the convective heat losses to the ambient.

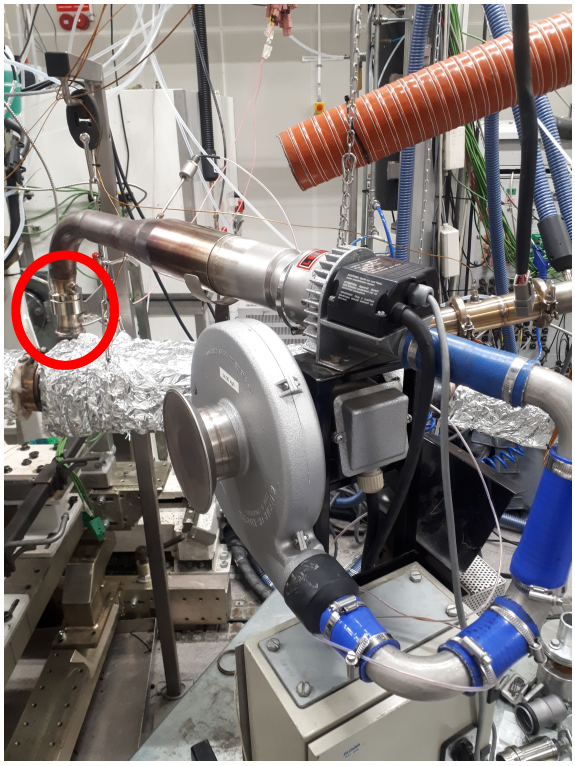

**Figure 3.4:** Display of the fan used for heating/cooling purposes

The high thermal mass of the cooler allows for the smaller temperature gradients throughout the experiments. When temperatures settles at certain operating points, it became possible to heat the exhaust stream even further. This allowed for an operating point to have a larger temperature range. Similarly, cooling the exhaust gases is an option that is utilised to achieve a negative temperature gradient sweep.

### 3.1.3 Catalyst

Lastly, a catalyst is mounted after the HE. Three catalysts with same washcoat specifications were sliced to lengths of 15, 30 and 70mm. The 70mm catalyst mounted inside the rig is displayed in Fig. 3.5.

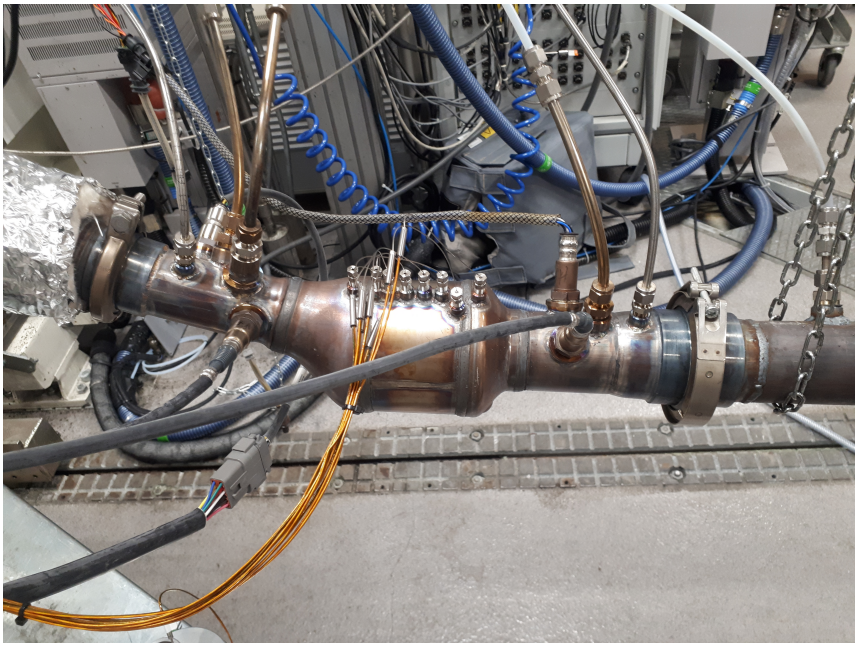

**Figure 3.5:** 70mm catalyst in rig environment

The thermocouples were all placed close to the center of the catalyst but at different axial positions as shown in Table 3.2. The various axial temperature measurements allow for the approximation of the catalyst slice temperatures which results in more accurate simulations.

**Table 3.2:** Place of the theromocouples for each catalyst

| Catalyst length | Thermocouple placement |
|---|---|
| 70 mm | 0, 7, 18, 29, 40, 51, 63 and 70 mm |
| 30 mm | 0, 10, 20 and 30 mm |
| 15 mm | 0, 7.5 and 15 mm |

The 70mm catalyst had the volume 0.40L, making the 30mm and 15mm being 0.17L and 0.09L respectively, having taken the effective open area into consideration. The

CPSI was 400, for all catalysts. All catalysts was from the same manufacturer, meaning that the specifications (such as coating weight, theoretical oxygen storage capacity (OSC), noble metal dispersion, etc.) were linearly related to each other. Unfortunately, this information can not be published within the thesis.

The temperature data from thermocouples gives a hint of where in the catalyst exotherms appear. This is essential when predicting reaction rates. When running data through the model-script, the slicing of the model is adjusted to the thermocouple measurements.

The purpose of running three different catalysts is to obtain species conversion with respect to temperature. A longer catalyst, i.e. 70mm, displays more than double the residence time to a 30mm, at a specific operating point. Studying a 30mm catalyst would ideally be equivalent of taking data 30mm into a 70mm catalyst, see Fig. 3.6.

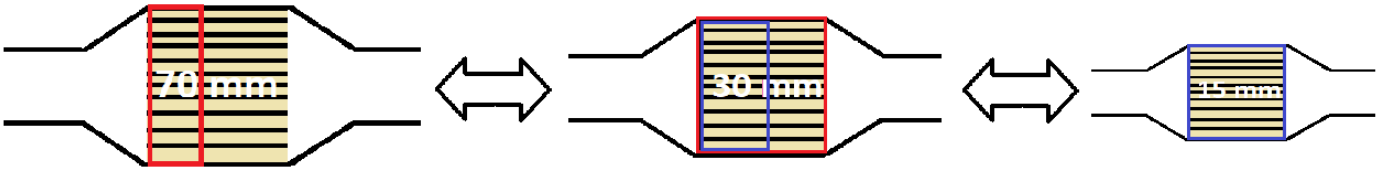


**Figure 3.6:** An illustration of equivalence in between the different catalyst sizes

This is not feasible with the instruments available, which is why these catalysts have been prepared. The main idea is that by using shorter catalysts, a higher reaction sensitivity can be found, which can be used to obtain in increased understanding in the operations within the catalyst.

## 3.2 Instruments

A number of instruments are used to categorize measurements. From Horibas MEXA-system, signals such as NO, CO, $CO_2$, THC, $O_2$ and $\lambda$ are obtained, both pre- and post catalyst. An $H_2$ measuring system called H-Sense from V&F is also available. It is possible to measure both pre- and post catalyst, but not simultaneously. In the following sections a brief overview on the systems together with delays and dynamics will be given.

### 3.2.1 MEXA-system

The MEXA-system can measure NO, CO, $CO_2$, THC, $O_2$ and by using that information calculate $\lambda$ via the Brettschneider equation, as presented in Eq. 2.13. The calibration on the MEXA-system shows $\pm$ 1.0% full scale and $\pm$ 2.0% point scale accuracy for all species. The drift within $\pm$ 0.75% is based on full scale per 8 hour time span. For all species, the accuracy is within $\pm$ 2.0%, repeatability within $\pm$ 1.0% and the noise level within $\pm$ 1.0%. Response time includes addition of the transport

delay $T_d$ and the time taken to reach 90% of the response, $T_{90}$. This information was obtained from a test report given by HORIBA on the system. Unfortunately, the details on the test procedure are unbeknownst to us.

In the upcoming sections the principles on which measurements are made are described. The specifications for all instruments are summarized in Table 3.3.

**Table 3.3:** Specifications for all parts of the MEXA-system

| Species | Range | Calibration gas concentration | Td+T90 Pre (s) | Td+T90 Post (s) |
|---|---|---|---|---|
| CO(H) | 0-3∼12[1] (vol%) | 8.6 (vol%) | 10.5 | 7.9 |
| CO(L) | 0-50∼3000 (ppm) | 991 (ppm) | - | 8.1 |
| $CO_2$ | 0-0.5∼16 (vol%) | 12.93 (vol%) | 10.7 | 8.1 |
| THC | 0-1∼500 and 2000∼15000 (ppmC[2]) | 11000 (ppm) | 3.8 | 3.7 |
| NO | 0-10∼500 and 200∼15000 (ppm) | 4925 (ppm) | 4.9 | 4.7 |
| $O_2$ | 0-1∼25 (vol%) | 20.5 (vol%) | 11.2 | 9.1 |

#### 3.2.1.1 CO & $CO_2$

CO and $CO_2$ are measured using a non-dispersive infrared sensor (NDIR). The principle exploits the fact that different compounds absorb infrared light at wavelengths characteristic to that specific compound. The intensity of absorbed light is proportional to the species concentration, which is used as a basis for measurement [6].

Interference can be exhibited from a range of compounds, including $H_2O$. CO and $CO_2$ can even interfere with one another. It has been possible to measure CO on two scales: high (H) and low(L), with high having a larger measurement range and low being more accurate in a short range. High scale is in percentage while low scale is in ppm. Giving more priority to a wider range, the CO measurements were collected at high scale and then converted to ppm.

#### 3.2.1.2 THC

The principle to measure HC is flame ionization detection (HFID). The exhaust gas enters a chamber where it is burned with $H_2$ and air. The reaction produces HC ions and electrons, where the amount of ions are proportional to the amount of carbon in the sample [44]. $O_2$ can interfere with the measurement within ± 1.5% at 21 vol%.

[1] Would be read as: Between 0 and 3 to approximately 12
[2] Methane($CH_4$)-equivalents

#### 3.2.1.3 NO

NO is measured via a chemiluminescence detector (HCLD), by forming an excited state of $NO_2$ via reaction with ozone ($O_3$). When returning to its normal state, it emits light of a certain intensity which is proportional to the amount of NO in the measured sample [44].

Additionally, $CO_2$ and $H_2O$ show interference within 0.05% and 0.22% respectively, at 1 vol%. A typical vol% for $H_2O$ of 15% would imply an error of 3.3%. These errors were not compensated for. The reasoning was that since $H_2O$ was not measured, it would be nonsensical to error compensate for something inherently erroneous. The $H_2O$ used within the EO-model was calculated as a look-up-table (LUT) vs $\lambda$ given the engine used from Auckenthalers thesis [6]. Regarding $CO_2$, even though information on this species was obtainable, the error is one magnitude lower than $H_2O$, meaning that the error was considered negligible.

#### 3.2.1.4 $O_2$

A magneto-pneumatic detector (MPD) is used to measure $O_2$ content in the exhaust gas stream, by taking advantage of its strong paramagnetic properties. If exposed to different magnetic fields, $O_2$ is attracted to the stronger one. It goes through a detection section, producing a force on a dumbbell as a consequence of the magnetic properties. The dumbbell rotates, influencing the amount of light reaching a photocell. A counter torque, proportional to the oxygen concentration, is applied to return the dumbbell to its original position [45].

### 3.2.2 $H_2$-Sense System

The $H_2$ system is separate from the MEXA instruments, and has to be processed independently. As mentioned previously, it allows for measurements both pre- and post catalyst, but not simultaneously. This is not considered a major problem, as an engine out mapping procedure is carried out to obtain a model of $H_2$ emissions as a function of $\lambda$, as well as engine speed and load. The model will be used to obtain $H_2$ emissions pre-catalyst, and hence we always measure $H_2$ on tailpipe during experiments.

The instrument is a H-Sense from V&F and is based on Electron Ionization Mass Spectrometry (EIMS). As described in a technical description from V&F [46], it is similar to Ionization Mass Spectrometry (IMS), with the exception of a different ionization process. After ionizing the species of the sample gas, a quadrupole is used as a filter to only let ions of a specific atomic mass pass through, which are registered by a counting detector. Calibration gases can be used to translate the ion count to a concentration. The instrument shows an accuracy of $\pm$ 2%, repeatability of $\pm$ 3% and a drift of $\pm$ 3% per 24h. This system has been shown to be slow in comparison to MEXA. Transport delay and 90% response time is close to 30s.

### 3.2.3 Sensor dynamics and delay

Given a change in target lambda, many factors contribute to the delay in emission changes. Firstly, there exists a delay caused by the fuel injector within the $\lambda$-control system which is negligible. Secondly, modifications to the exhaust manifold and the addition of the HE would introduce a transport delay of the exhaust gases to reach the catalyst from the engine. This was calculated by observing the delay in pre-catalyst $\lambda$ sensor given a target $\lambda$ change and this resulted in 300ms delay at 17g/s flow. As a form of validation, this delay reduced to 150ms when the volume flow was increased to 34g/s.

Lastly, both the MEXA analysers, that pertain to pre- and post-catalyst measurements, were placed before the catalyst and the delay in response with respect to each species were noted after a target $\lambda$ change, see Table 3.4.

| Instruments | $O_2$ | CO | THC | $NO_x$ | $CO_2$ |
|---|---|---|---|---|---|
| MEXA$_{Pre}$ | 11.3 | 10.2 | 2.8 | 3.9 | 10.2 |
| MEXA$_{Post}$ | 8.1 | 6.6 | 2.8 | 3.6 | 5.9 |

**Table 3.4:** Species delays by MEXA sensors that correspond to Pre- and Post catalyst positions

Along with the above time delays, the sensors also inflict a low pass characteristic effect on the measurements and this is clearly seen on the engine-out emissions as shown in Fig. 3.7. This effect was rectified by calculating the average steady-state after each transition which would then replace the transient dynamics as shown in Fig. 3.8.

Even though these dynamics are visible on the tailpipe too, the effect is more pronounced due to the oxygen buffer filling and depletion effects. This greatly affects the optimization of the oxygen buffer reactions (R10- R15) which will be discussed further in Section 3.4.

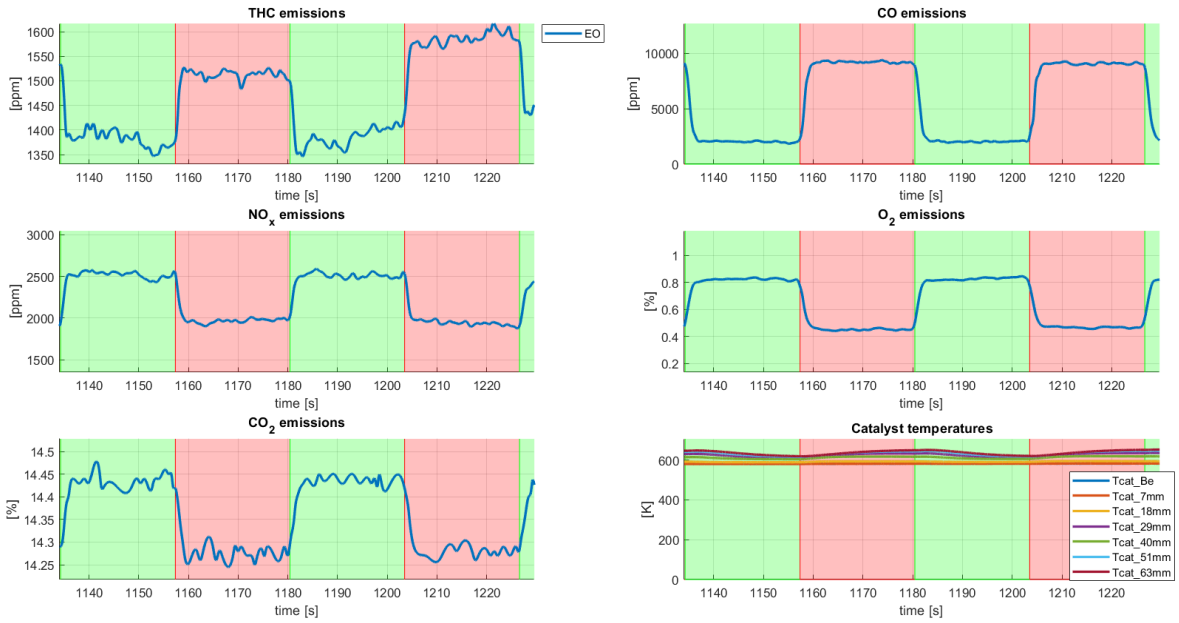


**Figure 3.7:** An example of the low pass characteristic on the engine-out emissions due to the sensor dynamics

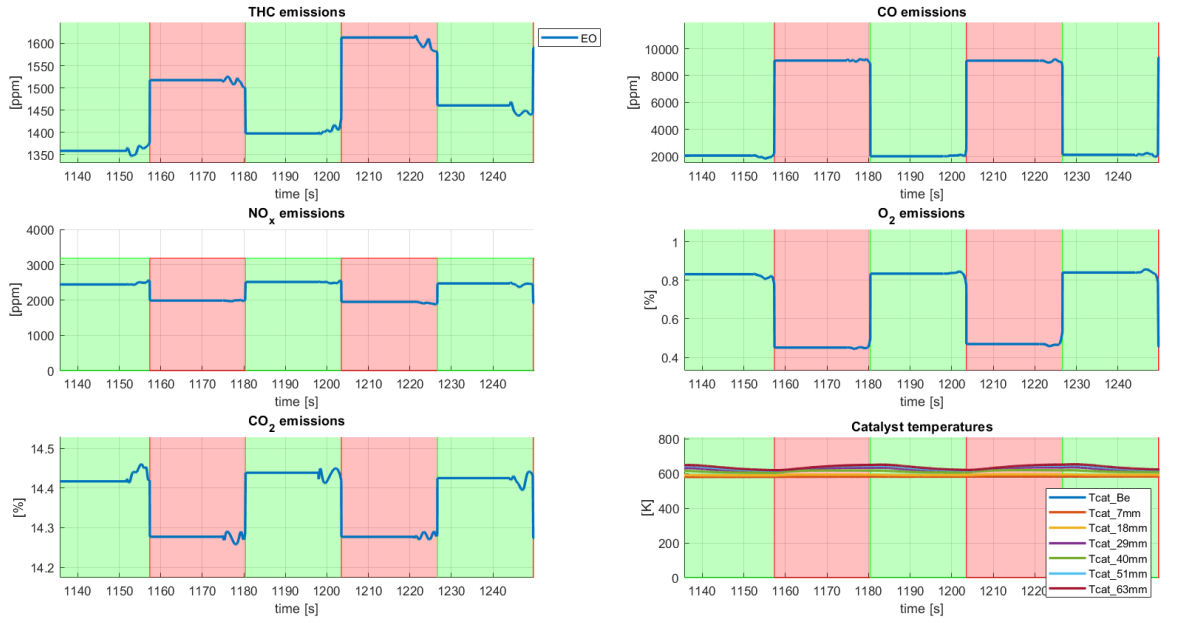


**Figure 3.8:** Sensor dynamics removed from the above example by extending the steady-states to the transient period

## 3.3 Experiments

A number of experiments have been carried out to obtain data for optimization, as well as to study general behaviour and trends. An initial engine-out mapping was carried out, followed by temperature sweeps given an operating point for each catalyst (15, 30 and 70 mm) and then temperature sweeps using open loop bang-bang control. These will be described in more detail in the upcoming sections.

### 3.3.1 Engine-out mapping

A model for engine out (EO) emissions was made for the particular engine in use. Tests included the following combinations of $\lambda$, engine speeds and engine loads:

- Engine speed: 1500, 3000, 4500 [rpm]
- Engine load: 100, 250, 500 [mg/str]
- $\lambda$: 1.2, 1.1, 1.05, 1.02, 1.01, 1.0, 0.99, 0.98, 0.95, 0.9, 0.8

The procedure can be thought of as a three-stage for-loop as follows:

**Algorithm 1:** EO-mapping procedure

```
for i = 1:No. of engine speeds do
    for j=1:No. of engine loads do
        for k=1:No. of λ do
            Allow to emissions to settle;
            Collect data;
        end
    end
end
```

In Fig. 3.9, a section of the EO-mapping of a CO measurement for 1500 rpm is shown; note the stepwise changes in emissions. At roughly 500s and 950s, the engine load is switched and the $\lambda$ values are reiterated given the updated load value.

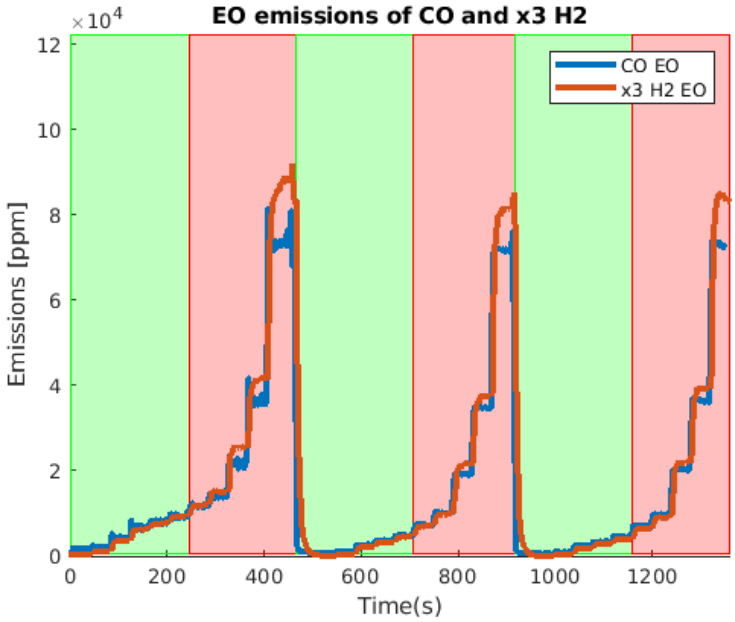


**Figure 3.9:** Engine out mapping of $H_2$ at 1500rpm

Alonside the blue CO legend, a red legend dictated to $H_2$ EO emissions can be seen. Notice the factor 3 multiplication, making the two curves co-align fairly well. This is expected, and a check to see if the H-Sense can be trusted.

To summarize: EO emissions were collected on CO, $CO_2$, NO, THC, $O_2$ and $H_2$ and was used to create look-up tables for emissions to be extracted as a function of the operating point.

### 3.3.2 Catalyst mapping

The mapping of the catalyst was performed using two types of experiments that consisted of temperature sweeps for each catalyst,

1. Constant $\lambda$ experiments
2. Open loop bang bang control or alternating $\lambda$ experiments

#### 3.3.2.1 Constant $\lambda$ experiments

A universal test routine for all catalyst sizes has not been used due to characteristics of smaller catalysts requiring slight modifications but the general theme has been to obtain a large temperature profile given an operating point. A temperature sweep is a technique where the experiment is initiated with a cold catalyst, followed by a section where it is heated up, finishing with a cooling down phase. Below follows a bullet list of the general steps involved using this technique.

1. Catalyst is initiated cold (i.e. before light-off) at 1500 rpm and 325 mg/str and a constant $\lambda$.
2. Catalyst heats up and reaches a steady-state. Fan is turned on and the air is heated to 700°C.

3. Catalyst heats up even more and settles at a new steady-state.
4. The engine speed is increased to 3000 rpm and the process is allowed to settle.
5. Catalyst is cooled down through either step 6 or 7.
6. Fan is turned to ambient temperature and engine speed is reduced to 1500 rpm simultaneously.
7. Engine speed is reduced to 1500 rpm and the process settles, followed by setting the air through the HE to ambient temperature.

Graphically, this can translate to an illustration displayed in Fig. 3.10.

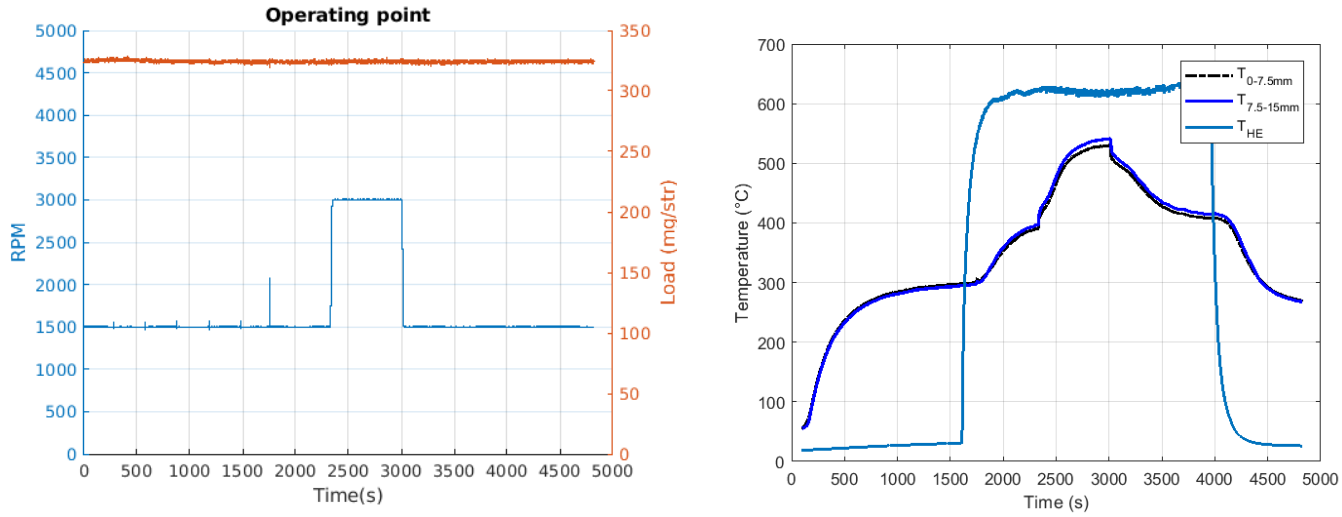


**(a)** **(b)**

**Figure 3.10:** a) Operating point; b) Temperature profile

To the left, an operating point graph is shown. The red legend shows the engine load in mg/str, while the blue legend displays the engine speed in rpm. To the right, a temperature profile is displayed where $T_{HE}$ is the air temperature inside the HE. The other lines display temperatures within the catalyst in °C. The changes to the HE such as heating or cooling the air is manually performed by the operator by visibly checking if the temperature have settled.

The purpose of this experiment is to capture the temperature dynamics such that it is possible to closely observe the light-off and reverse light-off in detail. The distinct temperature dependence is important to fit the activation energies, $E_a$, in the optimization routine.

By using the above experiment as a foundation, Fig. 3.11 displays conversions of CO and THC as a function of catalyst rear temperature, using acquired data.

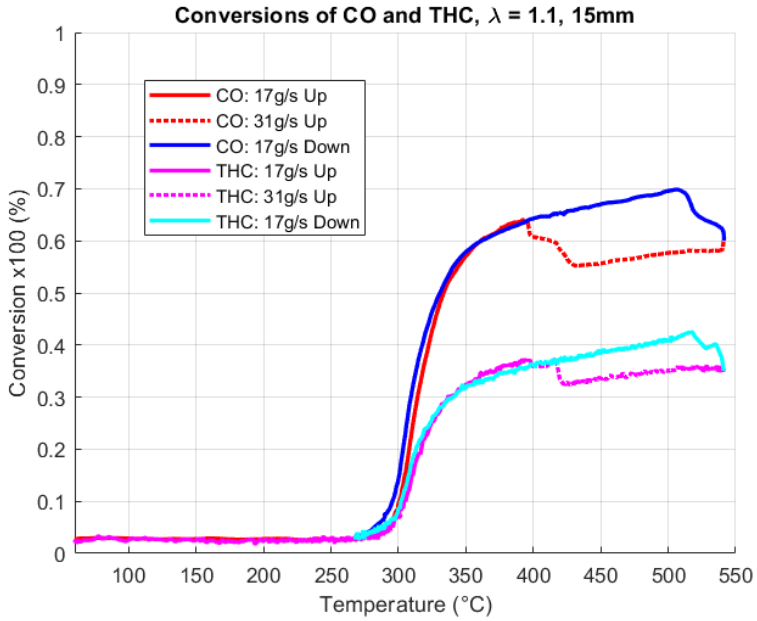


**Figure 3.11:** An example of how conversion changes as a function of temperature using the 15mm catalyst

It is important to keep in mind that when switching engine speeds the mass flow is affected, see Eq. 2.4. In the above example, engine speed is revved up at 2300s, and revved down at 3000s. This explains the drop at 400°C and jump at 550°C, as a result of a varied residence time. It will be shown later that this type of plot was a good tool for analysis, especially when running rich side, as it can highlight a poisoning phenomenon.

In Table 3.5 below a visualization has been made to show the choice of $\lambda$ made for each individual catalyst size.

**Table 3.5:** Constant $\lambda$ experiments performed

| Catalyst size | $\lambda$ | | | | | | |
|---|---|---|---|---|---|---|---|
| | 1.20 | 1.10 | 1.02 | 1.0 | 0.98 | 0.977 | 0.90 |
| 70mm | ■ | | | ■ | | | ■ |
| 30mm | | ■ | ■ | ■ | ■ | | ■ |
| 15mm | | ■ | ■ | ■ | ■ | ■ | ■ |

The inconsistency in experiments is explained due to the fact that different realizations were made as this phase progressed. Initially the 70mm was tested, followed by 30mm and 15mm. Catalyst of 15mm and 30mm included ±2% and ±10% change from stoichiometric lambda as the conversion rates were more sensitive to small changes.

$\lambda = 0.977$ might seem random, but is in practice a value that Volvo engineers has found superior to the theoretical $\lambda = 1$. Also 30mm was run at $\lambda = 0.98$. A rich side poisoning effect was found at this stage, and studying this value was hence considered interesting. More detail will be given in an upcoming section.

Additionally, a range of extra experiments as saw fit was tested which included spark-retards as well as alternating engine speeds. These will also be focused upon in a later section where phenomenological observations are illustrated.

#### 3.3.2.2 Alternating $\lambda$ experiments

The open loop bang-bang control experiments were initially decided upon for oxygen buffer tests. The temperature sweep as described earlier is utilized here. Table 3.6 summarizes the intervals of $\lambda$ studied for each catalyst size.

**Table 3.6:** Alternating $\lambda$ experiments performed

| Catalyst Size | $\lambda$ | | | |
|---|---|---|---|---|
| | 0.90-1.10 | 0.92 - 1.08 | 0.96-1.04 | 0.98-1.02 |
| 70mm | | ■ | ■ | ■ |
| 30mm | ■ | | ■ | ■ |
| 15mm | ■ | | ■ | ■ |

A closed-loop bang-bang controller switches $\lambda$ given information from the binary sensor, as explained in Section 1.1. A feed-forward controller follows another protocol, where the period time is dictated by the following integral,

$$\int_0^T \dot{m}\Delta\lambda \, dt = \Big[\dot{m}\Delta\lambda t\Big]_0^T = \dot{m}\Delta\lambda T = Constant \tag{3.1}$$

$$T = \frac{Constant}{\dot{m}\Delta\lambda} \tag{3.2}$$

where $\dot{m}$ is the massflow out of the engine. When the integral has accumulated to a value of choice, it will switch $\lambda$, reset the integral and recount up to the value of choice.

These measurements can cover steady-state data for two $\lambda$-values along with transients if the period time is sufficiently long for the process to settle. However, this time efficient data collection method comes with the trade-off of some additional post-processing of data. Similar to the constant operating point conditions, at high mass flows and temperature, effect of mass transfer limitation and coking can still be observed.

Fig. 3.12 shows a 30mm experiment that is explained in order to understand and visualise the data that is used for optimisation. The either green or red backgrounds display whether the target-$\lambda$ is set to lean or rich.

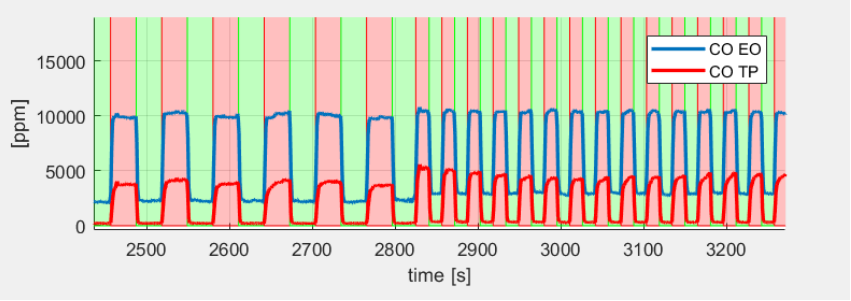


**Figure 3.12:** 30mm catalyst feedforward bang-bang experiment with Lambda ranging from 0.98 to 1.02

It must be noted that the engine speed is increased to 3000rpm from 1500rpm at 2800secs and in turn, mass flow increases accordingly. This causes the integral in Eq. 3.1 to accumulate faster, thus reducing the period time. This data shows visual interest as it depicts differences between rich and lean states in a neat way. Moreover, this data was used for optimization purposes in this thesis.

This reduction in period time is harmless to the MEXA instruments due to their fast response time but it does not allow the $H_2$ measurements to settle. Therefore, either the value up to which the integral accumulates to is increased or such data is avoided during optimization.

## 3.4 Optimization routine

Optimization is carried out via use of MATLAB function *lsqnonlin()*. This section holds a description of this method, details on the MATLAB implementation and selection of data for optimization.

### 3.4.1 lsqnonlin

*lsqnonlin*[47] is a built-in routine in MATLAB to solve nonlinear least-squares curve fitting problems on standard form

$$\min_x \quad ||f(x)||_2^2 = \min_x \quad f_1(x)^2 + f_2(x)^2 + ... + f_n(x)^2 \tag{3.3}$$

where $f$ is the objective function and $x$ is the variable to optimize for, which in this thesis will be kinetic parameters. Two potential choices of objective functions are proposed in a paper by Rao [48]. The first one is based on instantaneous data

$$f(x) = \sum_{i=1}^{N} \sum_{j=1}^{N_{comp}} w_j \Big( \frac{X_{i,j}^{meas}(t) - X_{i,j}^{pred}(t)}{X_{i,j}^{in}(t)} \Big)^2 \tag{3.4}$$

where $X$ denotes a species and $w_j$ a weighting factor. $N$ and $N_{comp}$ are number of data points and number of species considered. The variable $x$ is the parameter vector of kinetic parameters to be optimized for. Indices $meas$, $pred$ and $in$ refer to measured, predicted and inlet, respectively.

The normalization with $X^{in}$ is important as the species under certain operating conditions can be on different scales. For instance, when running rich NO is in ppm while CO is in percent. By dividing by the inlet concentration, these signals can be compared on a similar magnitude.

The other choice of objective function proposed is a cumulative variant

$$f(x) = \sum_{i=1}^{N} \sum_{j=1}^{N_{comp}} w_j \Big( \frac{Cumulative_{meas} - Cumulative_{pre}}{Cumulative_{meas}} \Big)^2 \tag{3.5}$$

which is considered more robust, as it is shows more sensitivity to kinetic parameter changes than Eq. 3.4. It also gives more weight to the initial seconds, accumulating information from the past into the future. The authors argue that the instantaneous variant can lead to numerical errors in contrast to the cumulative method, as measured values can be low after light-off when full conversion has been reached. Cumulative values never become close to zero. By having these arguments in consideration, we will still use the instantaneous version when optimizing, as it performed without any evident problems over the course of this thesis.

Additionally, the *lsqnonlin* has a parameter called *DiffMinChange* which dictates the change in the parameter space that is checked before an iteration and this value is common for all the tuning parameters. Due to numerical differences between the pre-exponential, $A_i$, and activation energy, $E_i$, tuning parameters $a_i$ and $e_i$ were introduced as shown in Eq. 3.4.1. The base values for $A_i$ and $E_i$ are derived from the estimations by Ramanathan et al [4], while the initial guesses for $a_i$ and $e_i$ are kept as one.

$$k_i = a_i \times A_i exp\left(\frac{-e_i \times E_i}{RT_g}\right) \tag{3.6}$$

### 3.4.2 Optimization scheme

Optimization of all reactions at once is not feasible, as the parameter space becomes too large to handle. Instead, it is beneficial to separate the number of reactions based on a rough estimate of the regions they are active at and optimize them step by step.

With $\lambda < 1$, in constant $\lambda$ experiments, a performance loss effect was very much evident which will be shown in Section 5. This was undesirable as the model does not capture this effect and also since the engine is rarely subjected to such operating point for an extended period of time. Hence it was more meaningful to use the

steady-states seen in the alternating-$\lambda$ experiments.

A script for extracting steady-states was developed. Fig. 3.13 shows an example of the steady states collected at each step. Markers $x$ and $o$ on emission graphs correspond to lean and rich steady-state regions respectively. The objective function can be adapted to making comparison at these points only, focusing to tune the reactions for a steady-state fit.

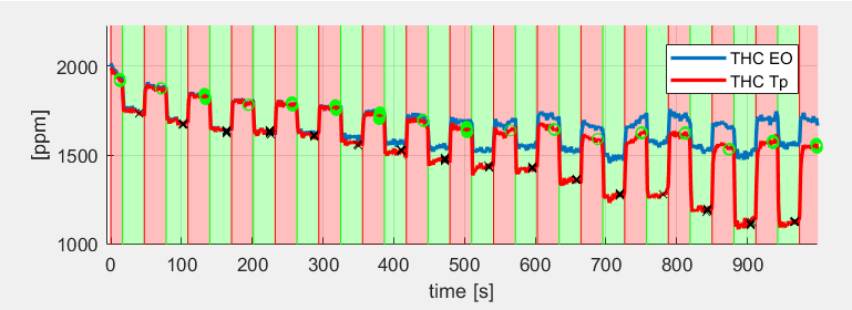


**Figure 3.13:** Steady-state indices chosen for a 30mm catalyst feedforward bang-bang experiment

The optimization started out by including multiple experiments (different amplitudes of lambda) pertaining to a catalyst length and also using experiments from different catalysts. It became apparent that finding a minima that is satisfactory to many experiments is not feasible as the chances of getting stuck in a local minima is high. Hence the model was tuned for a specific catalyst length alone and validated using other catalysts.

An assumption has been made regarding the buffer not being dominant when the emissions have settled for a given $\lambda$. The optimization is hence split into two sections:

1. Non-Ceria related : 9 reactions (18 parameters)
2. Ceria related : 6 reactions (12 parameters)

The optimization of the non-ceria reactions can be divided even further as follows,

1. Oxidation with $O_2$ (R1-R4)
2. Reduction of $NO$ (R5 - R7)
3. Water-gas shift and steam reforming (R8-R9)

#### 3.4.2.1 Sensitivity analysis

Sensitivity of the objective function, given by Eq. 3.4, with respect to the pre-exponential parameters were performed at different time intervals such that a step-by-step approach towards optimization can be formulated. The parameters pertaining to the activation energy were not taken into account due to the complexity it would bring into the analysis.

For reference, the following reactions will be considered:

$$R1 : CO + \frac{1}{2}O_2 \rightarrow CO_2 \tag{3.7}$$

$$R5 : CO + NO \rightarrow CO_2 + \frac{1}{2}N_2 \tag{3.8}$$

$$R8 : CO + H_2O \rightarrow CO_2 + H_2 \tag{3.9}$$

These reactions focus on CO, and will serve as a proxy on oxidation, reduction and WGS/SR sensitivities. The different regions considered and the sensitivities observed were,

1. Lean steady-states during catalyst light-off.
   This region contains the pre- and post-catalyst emission data when the engine is operated lean. Conversion of $NO$ is very minimal at lean regions and together with the knowledge that the water-gas shift and steam reforming reactions light off or become active at higher temperatures, it is intuitive that the oxidation using $O_2$ is most active.
   Fig. 3.14 compares the sensitivity of pre-exponential factor for reaction 1, $a_1$, to its counterparts $a_5$ and $a_8$. It is clear that the objective function has no sensitivity to $a_8$, while the model demonstrates a certain degree of sensitivity to $a_1$ and $a_5$. This is expected as both these reactions influence $CO$ concentrations and thereby, exhibit sensitivity to the objective function. Since the $NO$ conversions are minimal in the lean regions, it is safe to say that the lean light-off region can be used to optimize the reactions $R_1$ to $R_4$ (Oxidation using $O_2$).

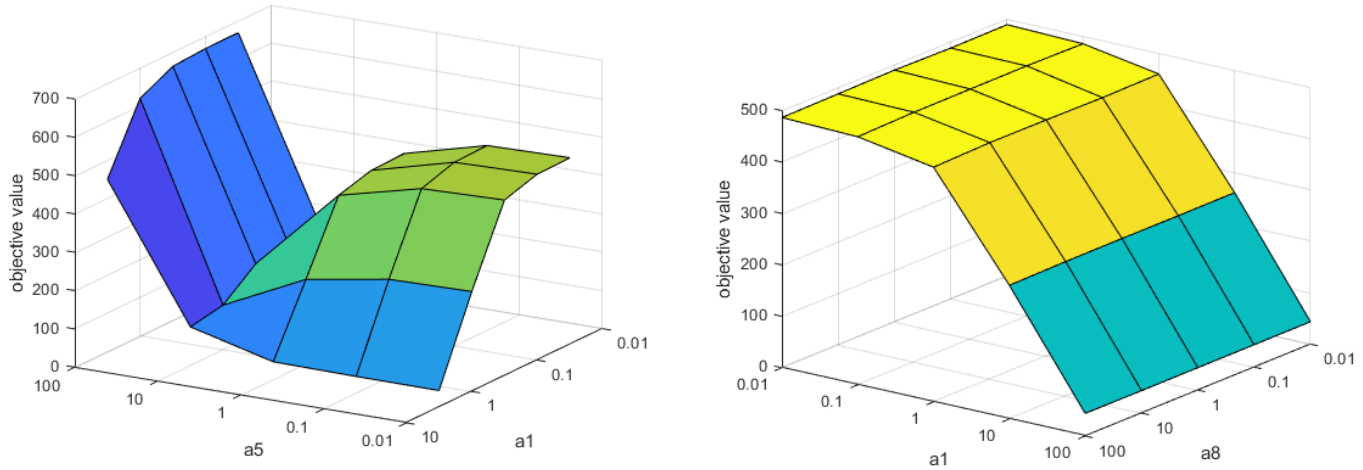


**Figure 3.14:** Sensitivity of the objective function with respect to the lean intervals during catalyst light-off towards a) $a_1$ compared to $a_5$; b) $a_1$ compared to $a_8$

2. Rich steady states during catalyst light-off

The region contains the pre- and post-catalyst emission data when the engine is operated rich. Using the tunings for reactions, R1 to R4, from the previous case, it is now possible to tune the reduction of $NO$ reactions, R5 to R7. The sensitivity of $a_5$ has been analysed in this region as shown in Fig. 3.15.

The objective function is most sensitive to $a_5$ compared to $a_1$ and $a_8$, which denotes that this region can be utilised for the optimization of reactions, R5 to R7.

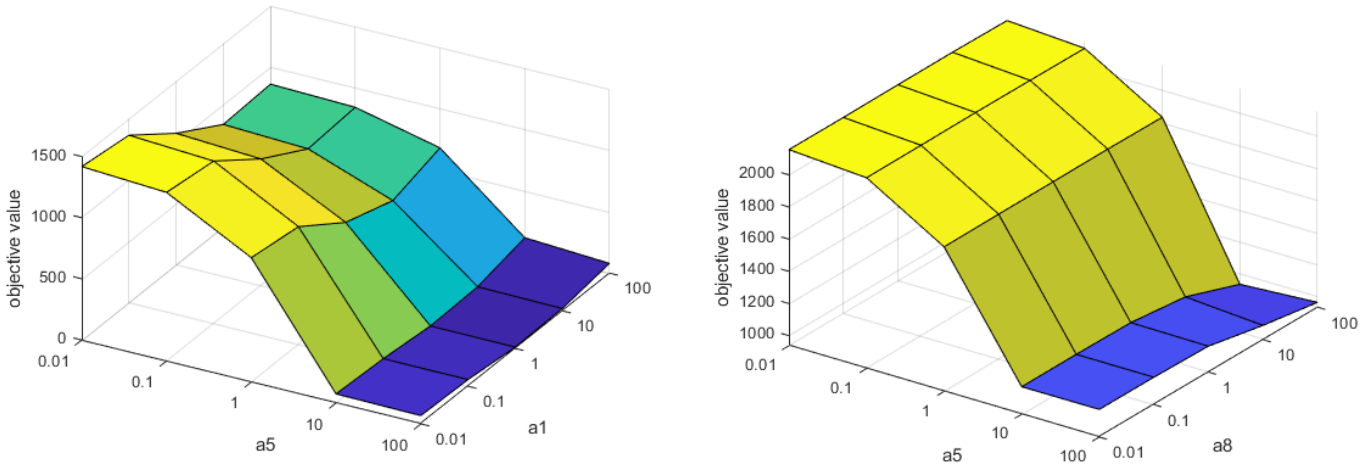


**Figure 3.15:** Sensitivity of the objective function with respect to the rich intervals during catalyst light-off towards a) $a_5$ compared to $a_1$; b) $a_5$ compared to $a_8$

3. Region that has deterioration of $H_2$ conversion (in other words $H_2$ production) with increasing temperature

The tuned reactions, R1 through R7, are kept active while analysing the sensitivity to the parameters in this region. Therefore, the sensitivity of the objective function is analysed with respect to $a_8$ and $a_9$ alone as shown in fig. 3.16. It is evident that this region is sensitive to both reactions, R8 and R9.

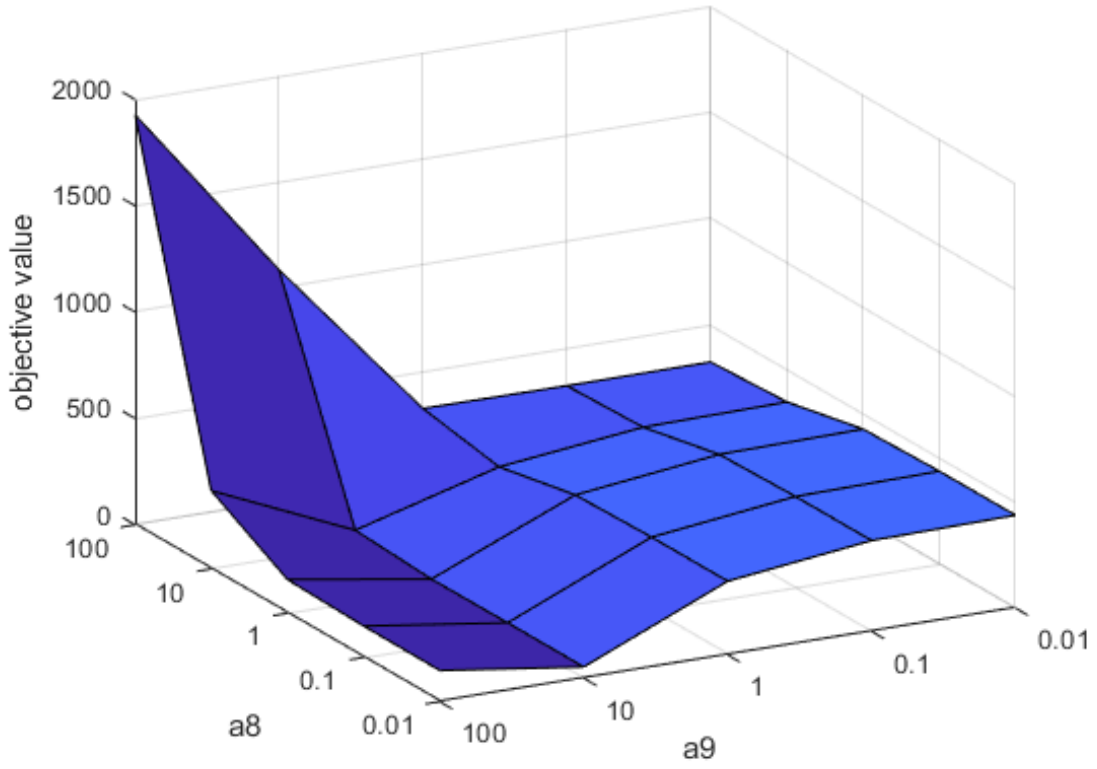


**Figure 3.16:** Sensitivity of the objective function with respect to the rich intervals during the activation of water-gas shift towards $a_8$ and $a_9$

### 3.4.3 Centered Arrhenius Expressions

By a bit of algebraic manipulation, one can rewrite the Arrhenius expressions slightly in order to de-correlate the activation energies $E_a$ and pre-exponential factors $A$, making the parameter search quest easier:

$$k = Ae^{\frac{-E_a}{RT}} = Ae^{\frac{-E_a}{R}(\frac{1}{T}+\frac{1}{T_{ref}}-\frac{1}{T_{ref}})} = Ae^{\frac{-E_a}{RT_{ref}}}e^{\frac{-E_a}{R}(\frac{1}{T}-\frac{1}{T_{ref}})} = k_{centered}e^{\frac{-E_a}{R}(\frac{1}{T}-\frac{1}{T_{ref}})} \tag{3.10}$$

The centered pre-exponential, $k_{centered}$, will work as an amplification at the reference temperature $T_{ref}$, while the exponential part will take care of the temperature dependence [49].

## 3.5 Selection of Data for Optimization

As already stated, optimizing for all reactions at once is suboptimal, as the parameter space becomes too large to handle. It was realized that even with only a few selected parameters, the *lsqnonlin* was prone to get stuck in local minima. Hence initial guesses are an important factor.

A starting point for guessing was by using the parameters proposed by Ramanathan et. al [4], see Appendix A. Some facets of the model was collected from the results of that paper, such as the kinetic model along with the reaction scheme.

Additionally, as optimization is a time consuming activity, it was considered necessary to run for dynamic data only and not data with little or complete conversions. This helps in obtaining sensitivity towards the objective function.

### 3.5.1 70mm ±2% feedforward bang-bang experiment

This is a catalyst heat-up experiment using a ±2% feed forward bang-bang controller and its engine-out and tailpipe data for the different species are displayed in Fig. 3.17. This data has been widely used to obtain the tuning parameters later shown in Chapter 4.

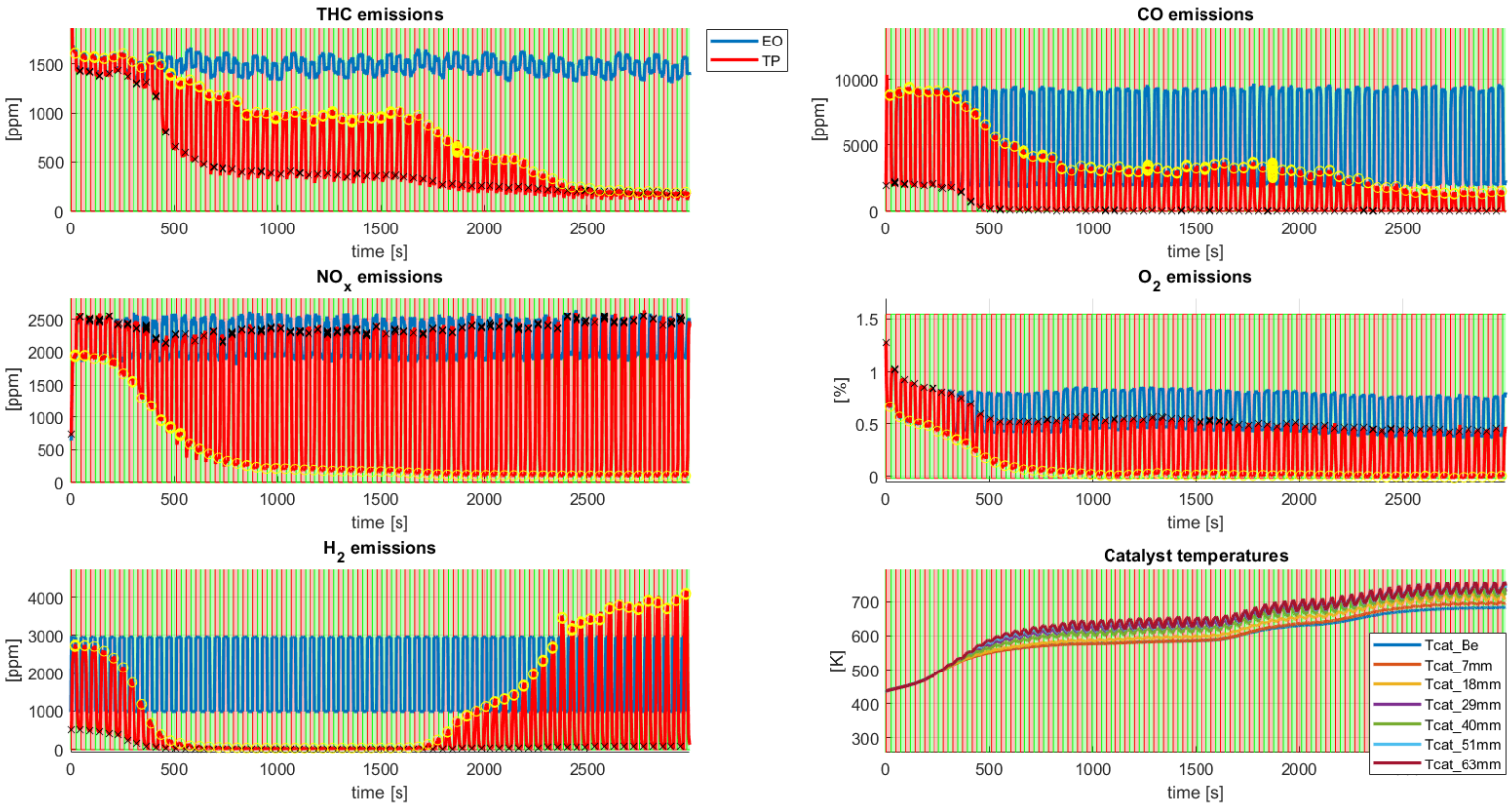


**Figure 3.17:** Data visualization for a 70mm ±2% heat-up bang-bang experiment

As recently explained, black and yellow markers denote the lean and rich steady-states, respectively. In between are oscillations, as a result of the bang-bang controller switching target $\lambda$ as a consequence of Eq. 3.1 summing up to a pre-defined value. The green and red background colours refer to $\lambda$ being in either lean or rich

state, and is just a tool for visualization purposes. This experiment is a temperature sweep, where a constant operating point of 1500 rpm and 325 mg/str is used. The air through the HE is heated to 700K (∼425°C) at 900s. In Fig. 3.18, the conversion equivalent (as a function of temperature) to Fig. 3.17 can be seen. Red legend is rich state, green is lean state.

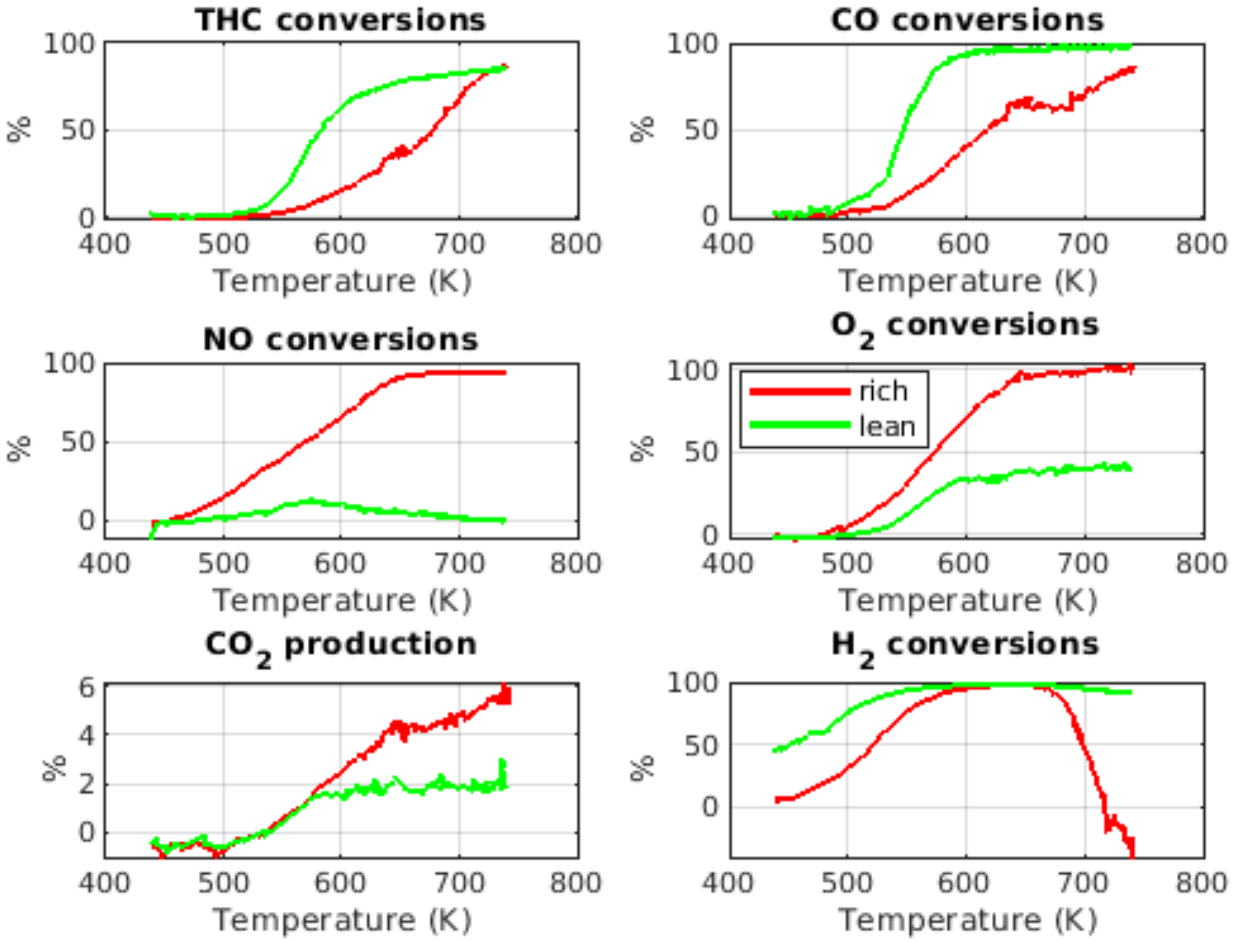


**Figure 3.18:** Species conversion with respect to catalyst temperature for a 70mm ±2% heat-up bang-bang experiment

It can be noted that the experiment starts at 450 K (∼ 175°C). This is before CO and THC lights-off, but it can be seen that NO has already slowly started its conversion, both lean and rich sides. This also applies to $H_2$ rich side. When the experiment starts already a 50% conversion lean side can be seen for $H_2$.

The lean side show especially good variation for THC and CO. Naturally, also $O_2$ vary due to the THC and CO combustion. $H_2$ also varies, but not to the same extent due to its reactivity at lower temperatures, in contrast to its co-species. This is hence good data for optimizing R1-R4. Even though there is abundance of $O_2$,

some THC fail to combust. This is captured in the model by introducing the slow oxidizers: $C_3H_8$. Some NO is used, but seems to be decreasing with increasing temperature. One explanation could be, that as temperature increases, $O_2$ usage increases, overpowering the reduction capabilities of NO, leaving less NO converted lean side. However, this has not been verified.

The rich side shows conversion for all species, and holds information on NO conversion, which the lean side lacked. This is hence a good region for optimizing R5-R7. $O_2$ ends up fully depleted, and WGS and SR contributes to THC conversion on par with its lean side counterpart. As for CO, a high conversion level can be noted, but it is not on the 100% that can be obtained lean side.

Note the negative conversion of $H_2$, which is a consequence of WGS and SR lighting-off. At this stage, more $H_2$ is produced than consumed. This is a good region for optimizing R8 and R9.

Lastly, the transient regions that capture the filling and depletion of the buffer is obtained as shown in Fig. 3.19.

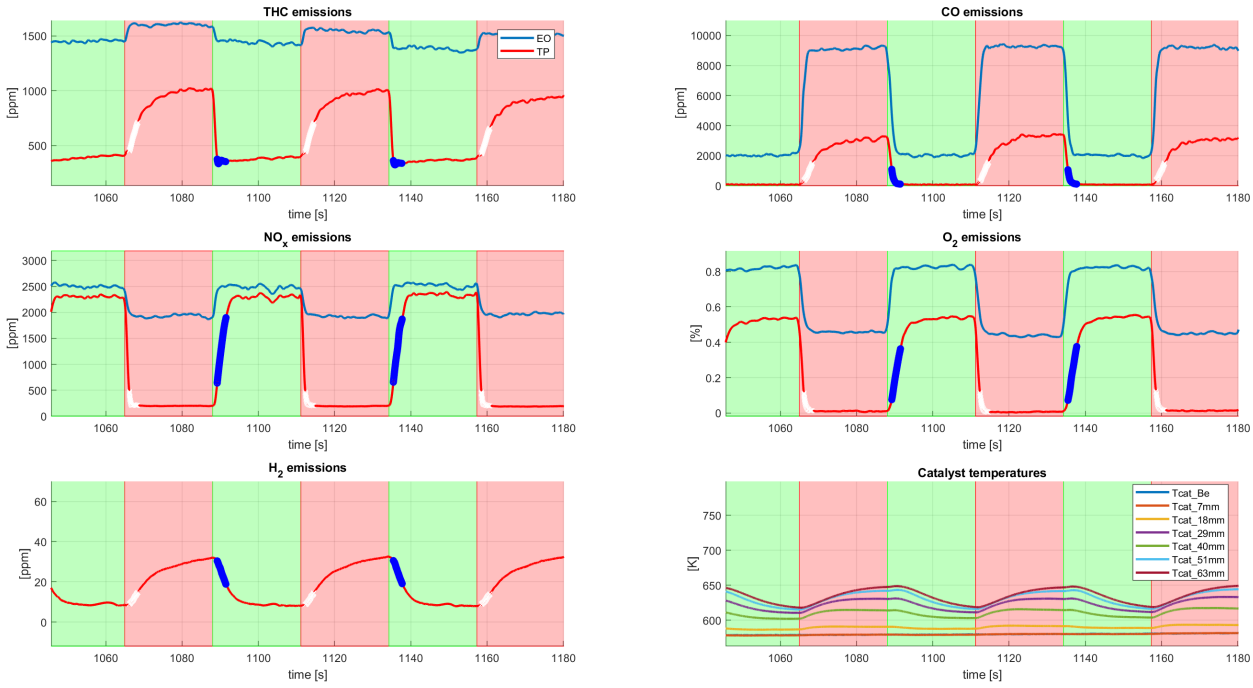


**Figure 3.19:** A zoom on the 70mm ±2% heat-up bang-bang experiment that captures the transients

After a switch to lean lambda, $\lambda > 1$, there is a considerable delay seen in the $O_2$ and $NO$ emissions to reach a steady-state. This region is given by the blue markers and it represent the filling of the buffer. Similarly, after a switch to rich lambda, $\lambda$

$< 1$, both $CO$ and $THC$ experience high conversion for an extended period of time. This region is given by white markers and it represents the depletion of the buffer.

### 3.5.2 30mm ±2% feedforward bang-bang experiment

Fig. 3.20 displays the corresponding conversion data for the 30mm catalyst. There are some similarities but also some differences as a result of the change in space velocity. The operating point is the same, resulting in a mass flow of 17 g/s.

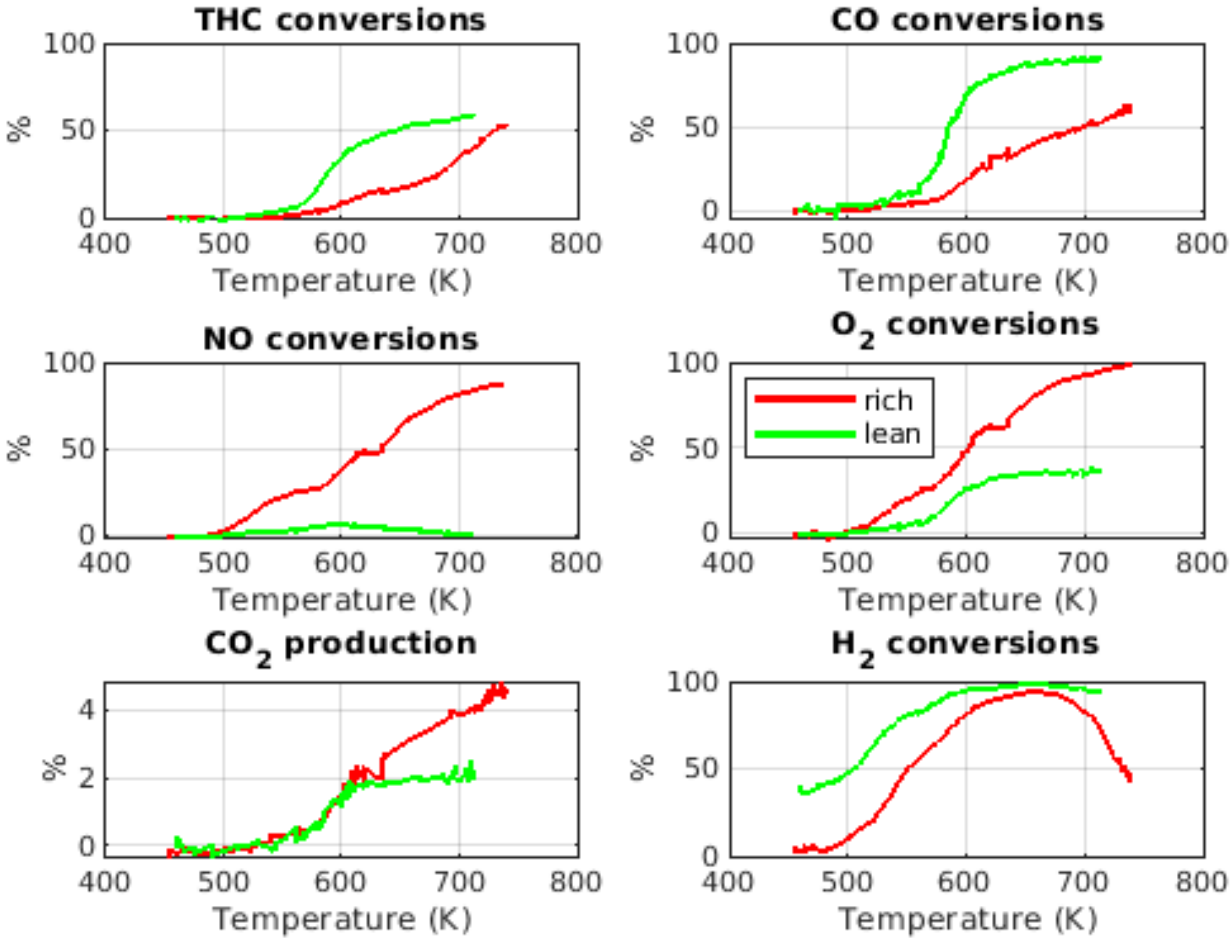


**Figure 3.20:** Species conversion with respect to temperature for a 30mm ±2% heat-up bang-bang experiment

The temperature frame is roughly the same, and so is the general curvature, but lower conversion levels can be seen. It is slightly better information $H_2$ lean side, as it starts at ∼40% conversion, rather than 50%. This data shows more nuance, as species can reach a steady-state without depleting. In that situation, which is the case for the 70mm, relevant information can be lost about the reaction kinetics.

## 3.6 Model Validation

To evaluate the tuning found via the optimization routine, some data has to be used for validation purposes. As will be shown later, the model will be optimized using 70mm data. Data for validation will hence be 30mm and 15mm data. Three different operating points can be tested, which is 1500, 3000 and 4500 rpm. Since load was always set to 325 mg/str, this translated to 17, 34 and 51 g/s mass flows. Experiments include a positive and negative temperature transients, which can be used. Also, a range of temperatures emerge as a result of the different operating points, in combination with using the HE.

# 4

# Experimental Results

## 4.1 Constant $\lambda$

Below follows a high-lighted summary of phenomena found using constant $\lambda$-experiments. This includes temperature distributions, light-offs as well as going in depth on a rich side performance loss phenomena running the catalyst excessively rich for a longer time period. For the interested reader, an in-depth analysis of all individual runs can be found in the Appendix section.

This particular phase of the thesis was part of learning how to use the instruments, meaning that a set experiment layout was not decided upon when starting. This resulted in an inconsistency in measurements taken, which is why some comparisons might seem arbitrary. This should still give an insight in how different sizes influence the behaviour.

### 4.1.1 Comparisons 30mm and 15mm $\lambda = 1.1$

In Fig. 4.1, the conversions of THC and CO is displayed as a function of rear temperature. It is obvious that the longer catalysts display higher conversion for both species. NO is omitted since the conversion is insignificant at a lean $\lambda$.

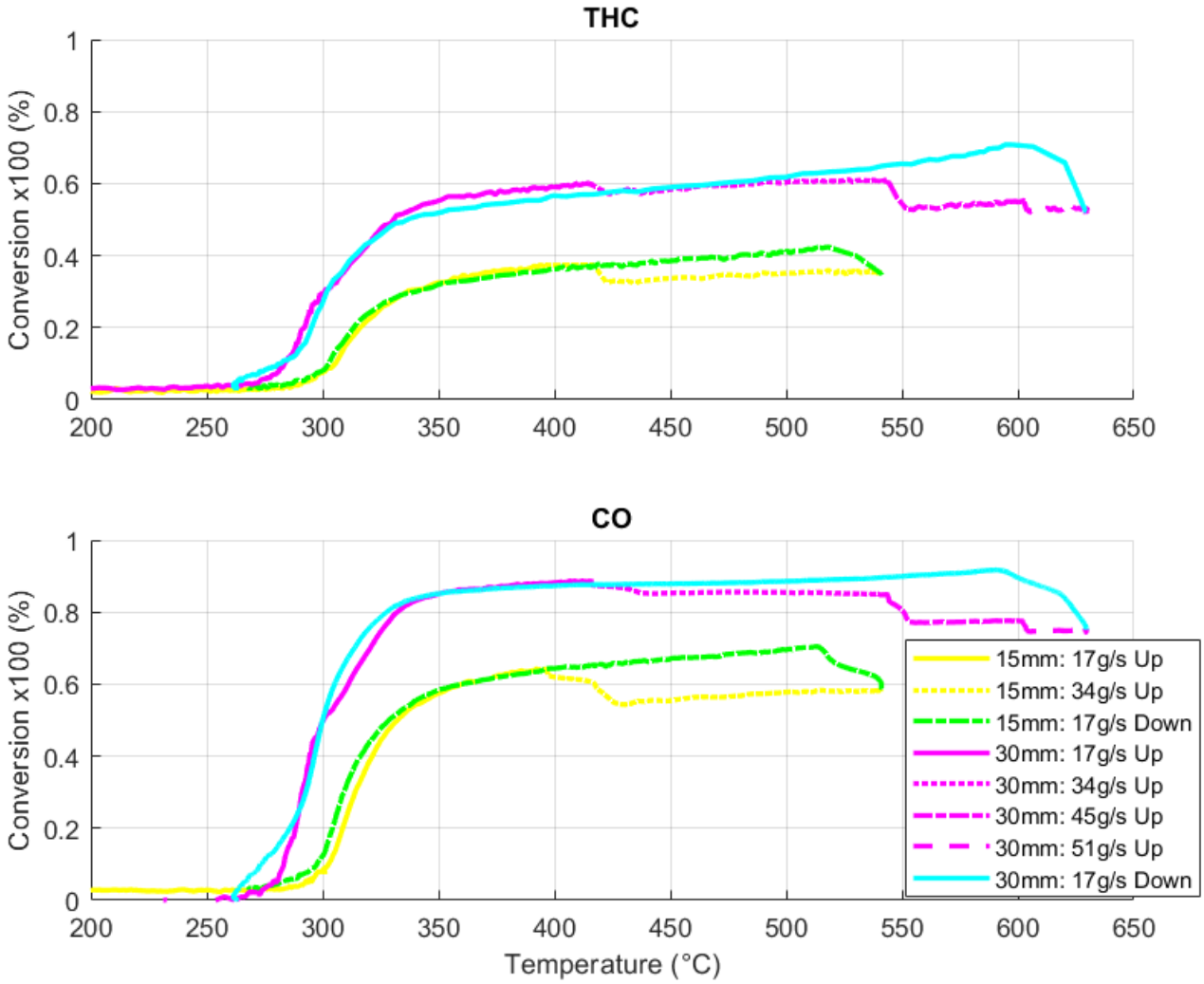


**Figure 4.1:** Conversion comparisons between 15mm and 30mm for THC and CO using $\lambda$=1.1

When changing the operating point, the influence of a decreased residence time becomes prominent. A sudden drop can be noted, followed by a section with a slight inclination, which is due to the temperature increase generated by the increased amounts of gas sent through the catalysts.

For both catalyst sizes, the up- and down-slopes coincide, showing no system hysteresis, which is expected.

### 4.1.2 Comparisons 70mm, 30mm and 15mm $\lambda = 1.0$

A change to a stoichiometric $\lambda$ is displayed in Fig. 4.2. Here, all main species has been studied for all catalyst sizes. Once again, it is quite obvious that the larger the catalyst, the more conversion occurs.

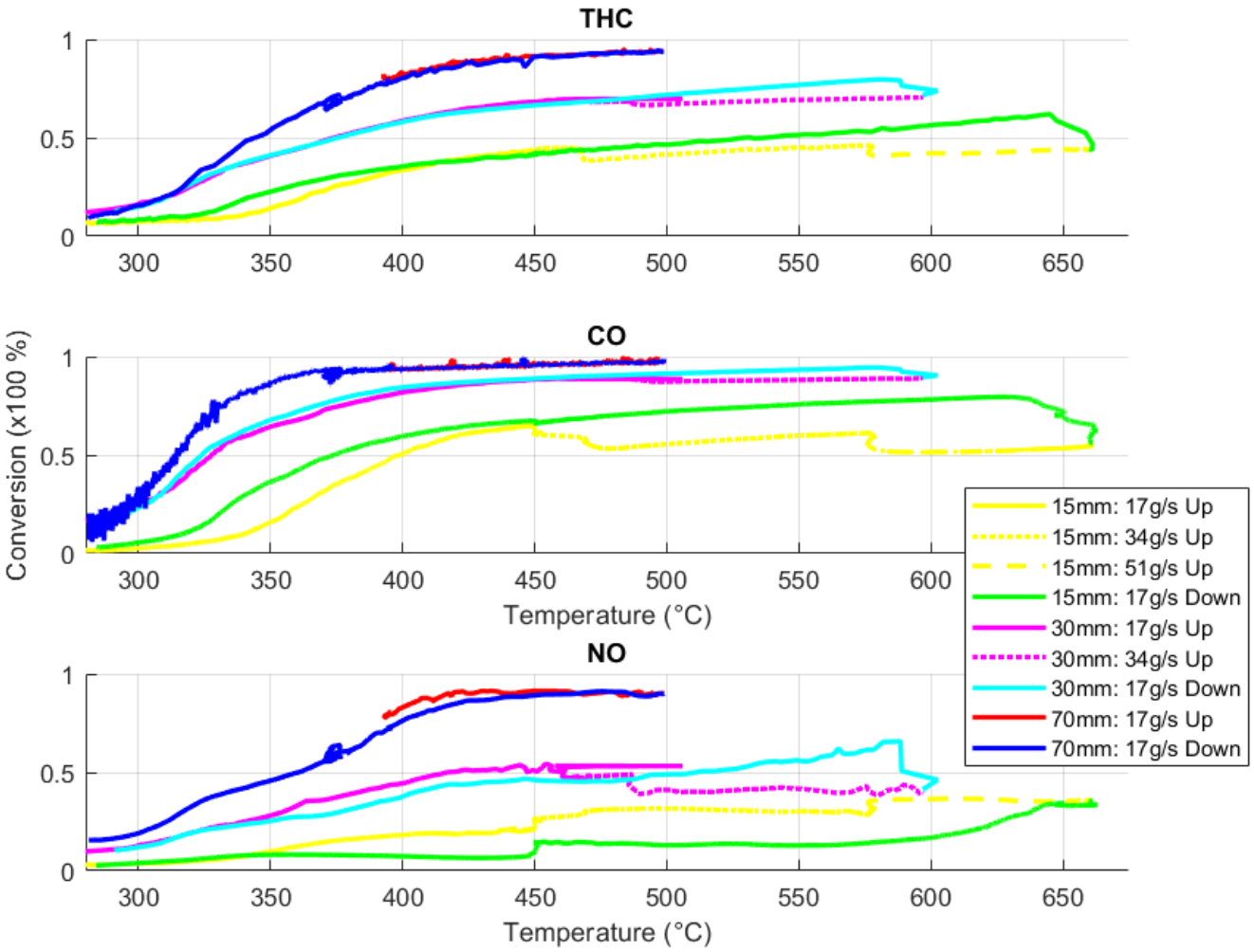


**Figure 4.2:** Conversion comparisons between all sizes and all species using $\lambda$=1.0

THC and CO conversions show similar light-off, but a hysteresis can be seen on 15mm. NO signals were noisy, and was low-pass filtered to obtain better graphs. The 15mm data shows a peculiar behaviour, where the conversion increases as the residence time decreases as a result of changing the operating point. It is unclear why this is the case, as CO and THC for the same experiment does not show the same behaviour.

The 15mm showing a hysteresis can be understood by studying the Brettschneider-$\lambda$ calculations, see Fig. 4.3.

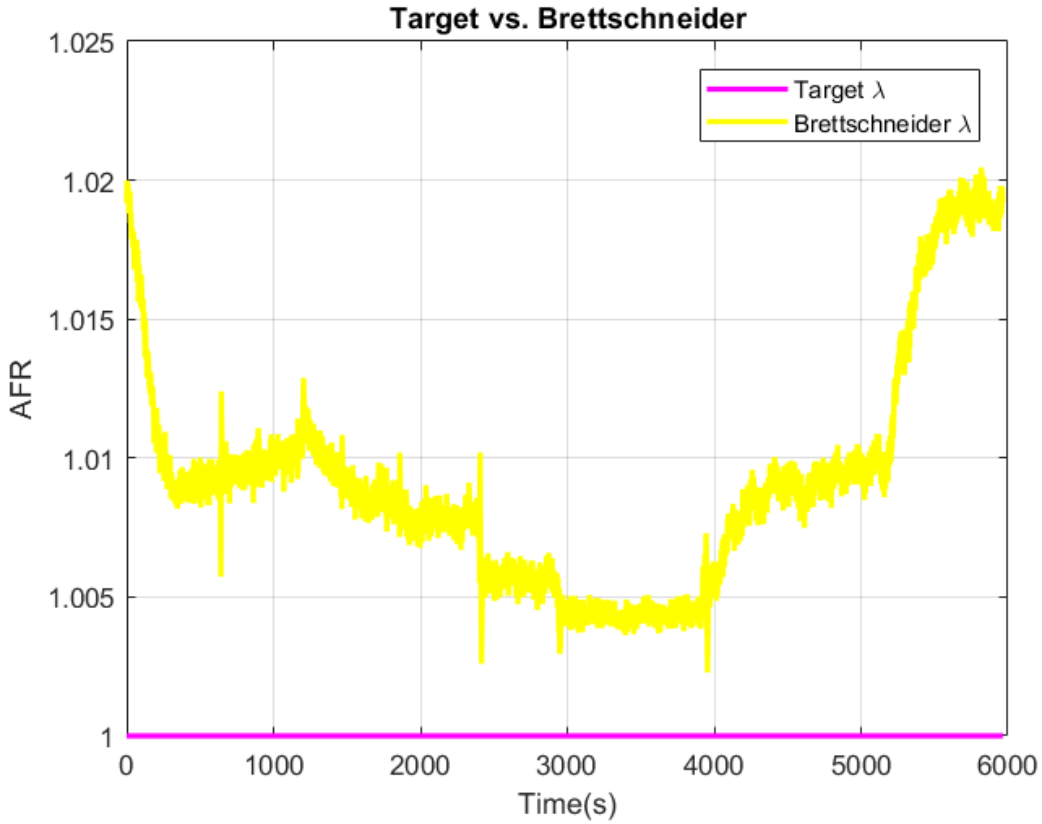


**Figure 4.3:** Target $\lambda$ vs. Brettschneider $\lambda$ for the 15mm $\lambda = 1.0$ experiment

The Brettschneider-$\lambda$ suggets that values are different up- and downslope. The target $\lambda$ is set to 1, which the controller obviously fails to meet. The Brettscheider-$\lambda$ is influenced by the operating point, and becomes more accurate as the mass flow increases. That is why it is believed that this phenomena can be attributed to a leakage of air into the heat-exchanger, influencing the $\lambda$-control system. This phenomena is reduced by pressure increase due to temperature or mass flow increases, obtained by changing the engine operating point.

### 4.1.3 Comparisons 70mm and 15mm $\lambda = 0.9$

Finally, a plot is displayed for $\lambda = 0.9$, see Fig. 4.4. Only NO conversion is shown, as CO and THC are non-existent at a rich $\lambda$.

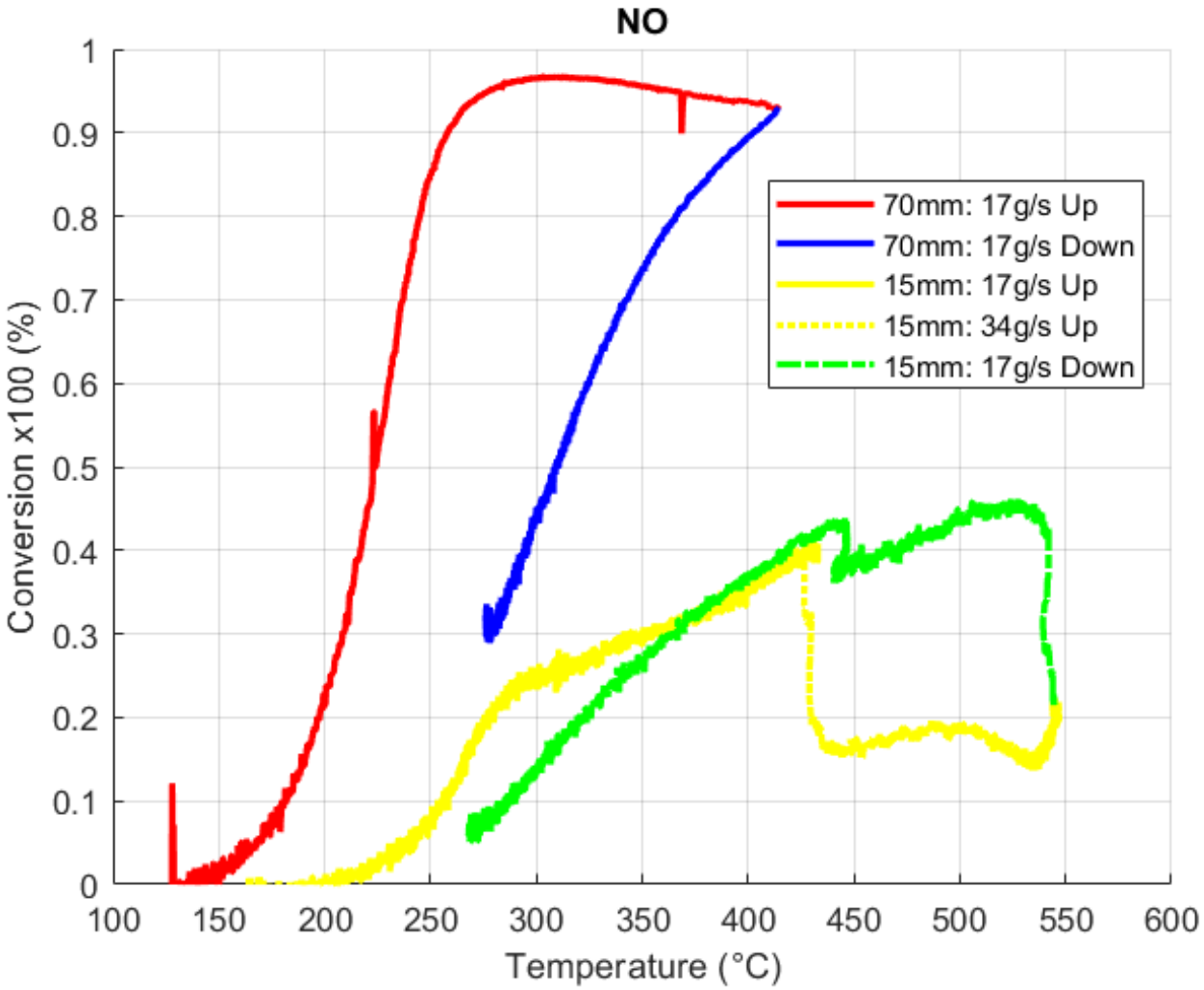


**Figure 4.4:** Conversion comparisons between 15mm and 70mm for NO using $\lambda$=0.90

Notice how the up- and downslopes are vastly different from each other. The 70mm upslope even shows a decreasing slope as a function of temperature. This is attributed to what is believed to be a poisoning effect, rather than hysteresis. This will be indulged upon in Section 4.5. It could also be attributed to an equilibrium between NO and $NO_2$, but since $NO_2$ data was not available, this assumption has not been verified.

## 4.2 Temperature Distribution

The 70mm catalyst houses a total of 6 thermocouples. The temperature development inside the catalyst can clearly be seen here. If the focus is put on the main three $\lambda$ tested using the 70mm catalyst, i.e. 0.9, 1.0 and 1.2, a typical temperature curve is displayed in Fig. 4.5. The operating point is 325 mg/str and 1500 rpm. The cooler is turned on at 0s and turned off at 2000s, its legend is omitted for visual purposes.

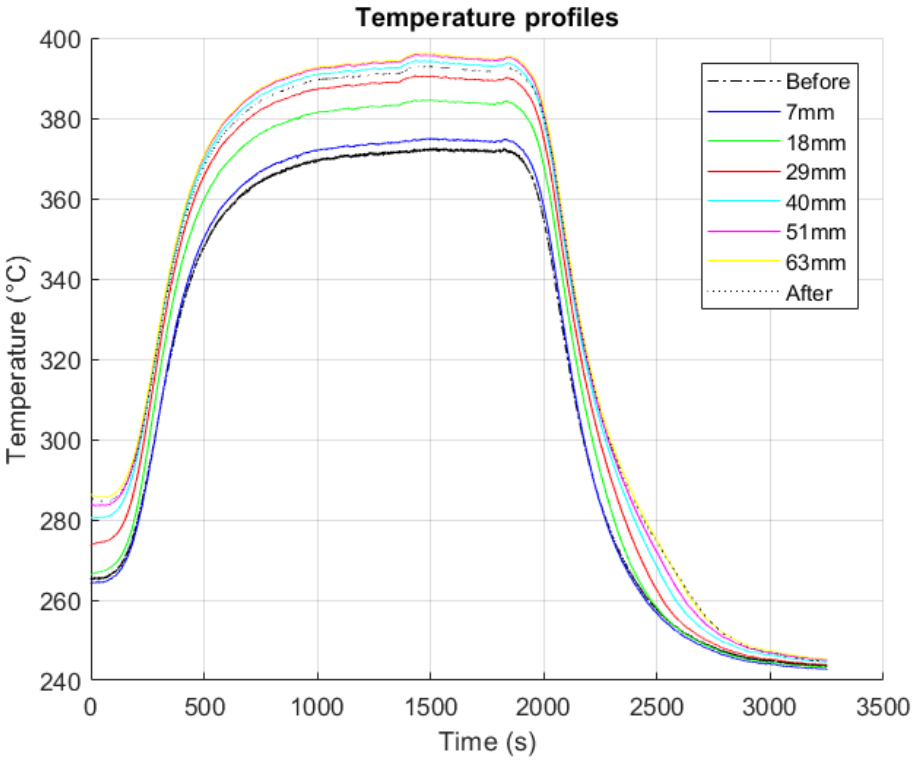


**Figure 4.5:** Temperature profiles (excluding the cooler) for $\lambda$=1.2

Exotherms are directly proportional to the amount of conversion within the catalyst, hence the amount of heat generated can be seen as a heuristic on where the reactions finish. Consider the formula

$$\frac{T_x - T_{Bef}}{T_{63} - T_{Bef}} \tag{4.1}$$

where $x$ is an arbitrary thermocouple location, such as 7mm, 18mm, etc. By seeing the $T_{63}$ as a max temperature, while $T_{Bef}$ as a minimum temperature, the above formula can be seen as a percentage of heat distribution within the catalyst. This is displayed in Fig. 4.6 below for all $\lambda$ studied using the 70mm catalyst. The temperature after the catalyst, $T_{After}$ is not used as it was seen to measure lower temperatures than $T_{63}$ which may either be attributed to convective heat losses from the system or contribution of the solid catalyst in temperature rise.

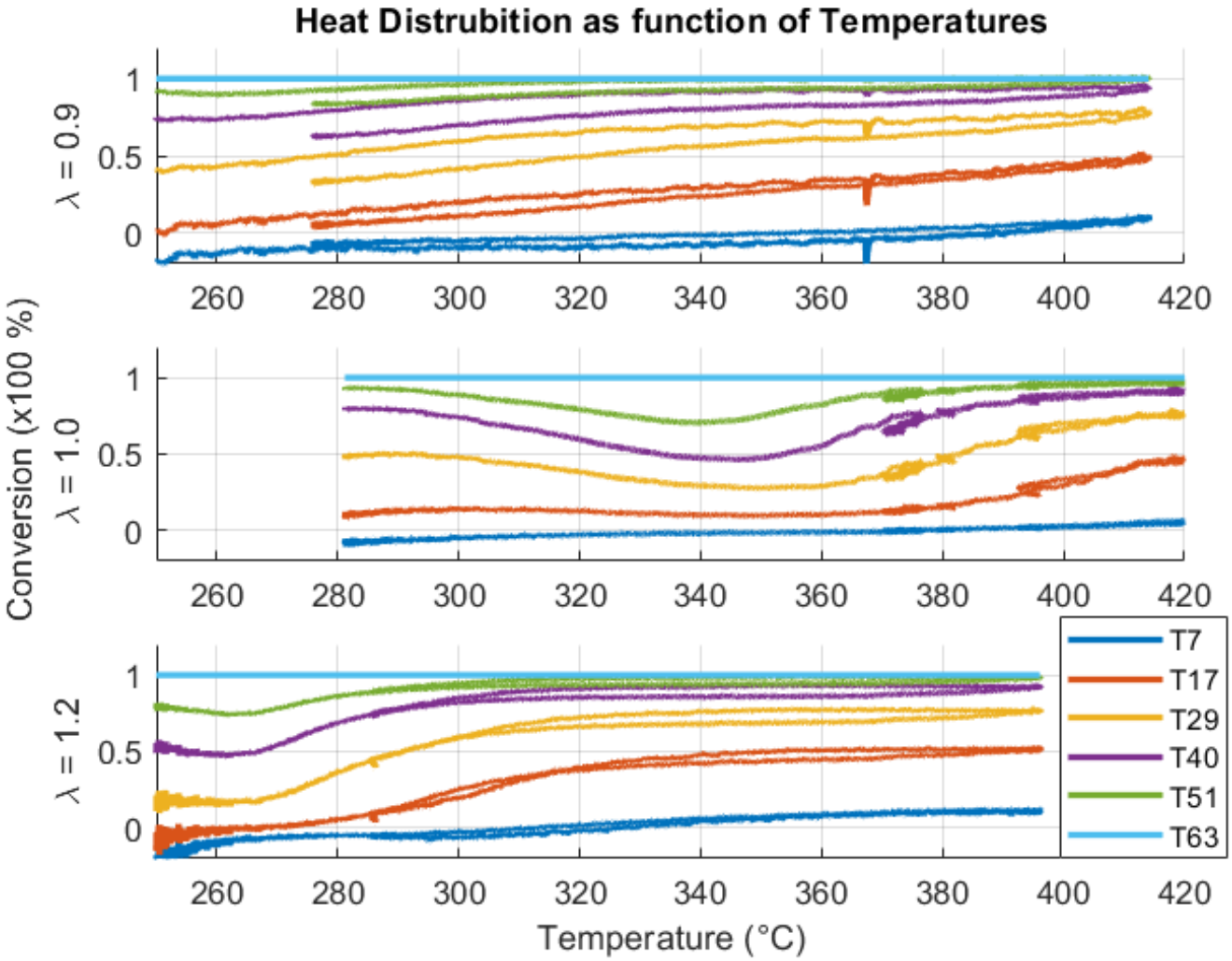


**Figure 4.6:** A subplot displaying the temperature distribution within the 70mm catalyst for each choice of $\lambda$ as a function of temperature

As the legend suggests, "full" conversion (the reference in this case) is the 63mm thermocouple which always displays 100%. The other legends suggest how far the temperature has developed. For all $\lambda$, when the catalyst is heated to its maximum for the current operating point, 95% of the heat development can be attributed to the first 40mm. Hence, the succeeding 30mm is not necessary as it does not contribute remarkably to any conversion. This analysis should be taken cautiously, as the thermocouples are sensitive during transients. This results in T7 at times suggesting negative conversion. However, the general distrubution is kept intact despite this fact.

As the 30mm and 15mm catalyst used less thermocouples, i.e. 2, the same resolution in temperature could not be seen for these experiments. This explains their absence in the analysis above. Given the results from the 70mm catalyst however, it seems like the choices of 30mm and 15mm are good candidates of shortenings, as this is less than the roughly 40mm required to finish reactions for those operating points

studied within the scope of this thesis.

## 4.3 Light-off Regions

The graphs displaying temperatures during light-off can be studied. Consider this setting using the 70mm catalyst, where 1500 RPM and 325 mg/str is used. The catalyst is initially cold at roughly 150°C, and it can be seen in Fig. 4.7 that all temperatures coincide.

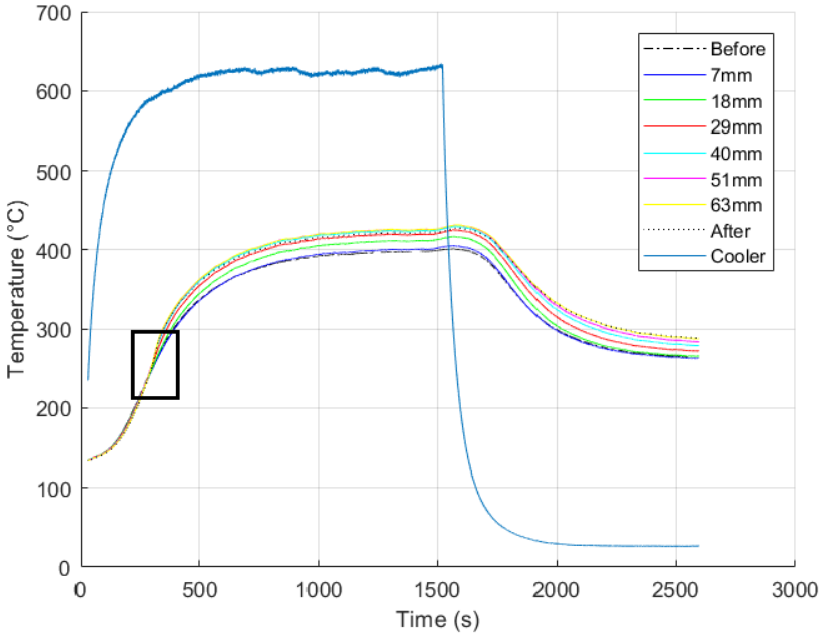


**Figure 4.7:** Temperatures at $\lambda = 0.9$, 1500 RPM and 325 mg/str using 70mm catalyst

Note the area marked with a black rectangle. This region is displayed in higher resolution in Fig. 4.8.

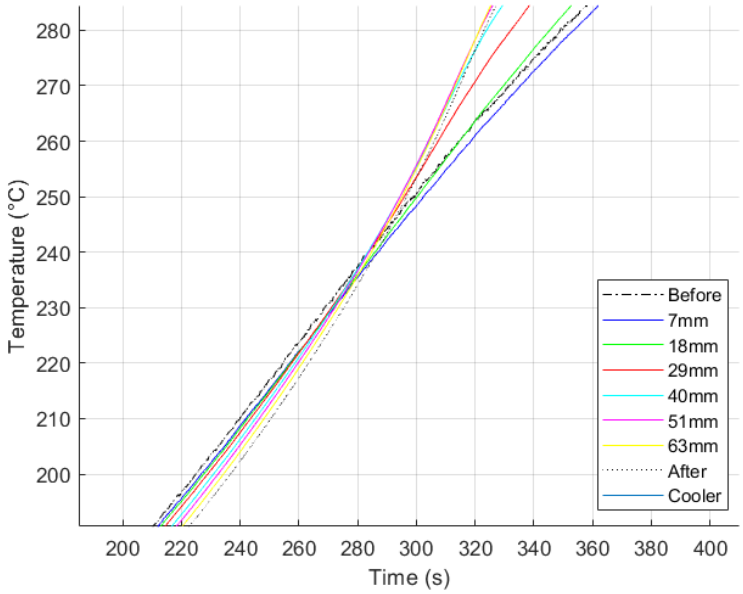


**Figure 4.8:** Light-off region at $\lambda = 0.9$, 1500 RPM and 325 mg/str using 70mm catalyst

The yellow curve, which is the rear temperature, is located below the blue curve displaying front temperature. As the catalyst lights off, it does this from the rear which is illustrated by the yellow curve showing a higher slope than the blue curve at light-off.

Conversion graphs are quite interesting as they display more in depth on how fast the light-off is for individual species. To study conversion of all species, $\lambda = 1.0$ is interesting, as it is reknown for being the preferred setting for converting all pollutants simultaneously. Looking at Fig. 4.9, it is quite clear that CO lights off faster, followed by THC and NO.

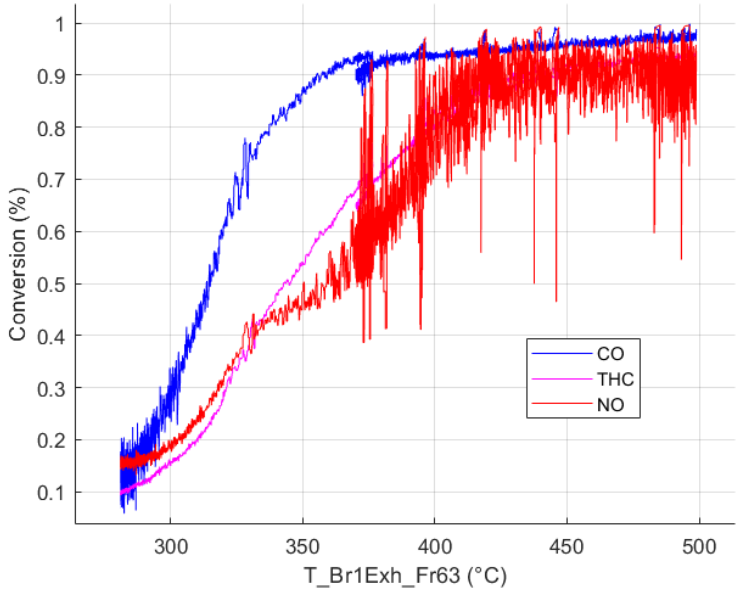


**Figure 4.9:** Conversions at $\lambda = 1.0$, 1500 RPM and 390/325 mg/str using 70mm catalyst

This is a general behaviour no matter the choice of catalyst size. The reason for using a 70mm once more is that the corresponding 30mm and 15mm experiments displays pulsing, giving less presentable graphs. The observant reader might note that the initial slope of NO is higher than the THC slope, suddenly decreasing, later picking up with temperature. The experiments suggest that NO do light-off earlier than THC, but is eventually overpowered by CO and THC as a result of $O_2$ being more prone to combust CO at higher temperatures, leaving less CO as a reducing agent for NO.

An attempt to validate the above reasoning, is by observing the model rate predictions, see Fig. 4.10. The rates are displayed in $\frac{mol}{m^3 s}$ as a function of time.

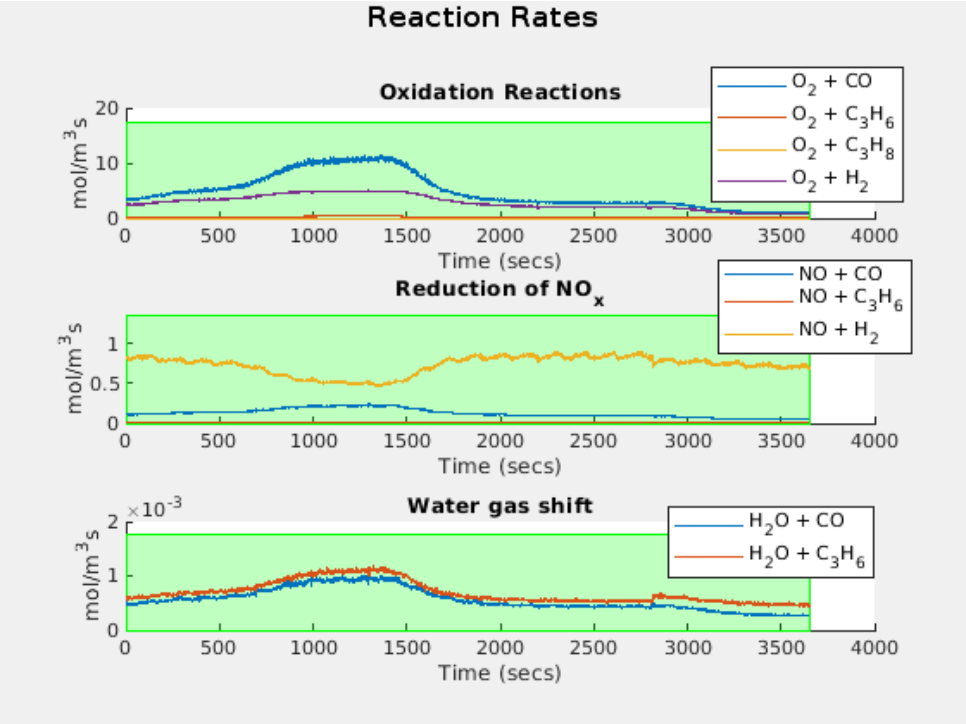


**Figure 4.10:** Rates as a function of time at $\lambda = 1.0$, 1500 RPM and 390/325 mg/str using 70mm catalyst

Important events are 1500s, when the fan is set to ambient. Already from the start, the fan is set to heat. Both CO rates via paths $O_2$ or $H_2$ shows a continuous increase over time.

However, note that the NO reduction via $H_2$ shows a continuous decrease up until the event of setting the fan to ambient, even though WGS and SR continuously increases, producing $H_2$. This suggests that at higher temperatures, $H_2$ favours $O_2$ combustion, rather than reducing NO.

## 4.4 Conversion Differences

As suggested earlier, a distinct hysteresis could be seen, especially for rich side experiments. This could be a result of a poisoning phenomena, which will be explained in more detail in an upcoming subsection. As for lean side experiments, a slight discrepancy up- and downslope could sometimes still be seen. This could be attributed to $\lambda$-control system issues, beyond the scope of this thesis. By studying the Brettschneider-$\lambda$, it could clearly be seen that the control system failed to find the right $\lambda$, which is believed to be due to a leakage in the heat exchanger.

An example can be made by looking at a 30mm $\lambda = 1.10$ experiment, where a slight discrepancy can be seen for THC up- and downslope. The operating point for this experiment is displayed in Fig. 4.11.

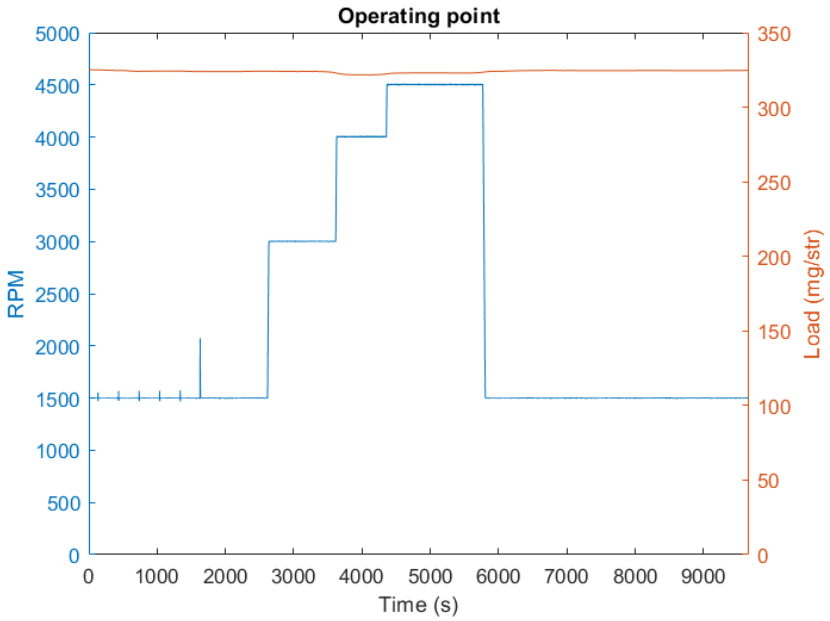


**Figure 4.11:** Operating point at $\lambda = 1.1$ using 30mm catalyst

See conversion profiles in Fig. 4.12, and note the THC graph. NO shows too low conversion for this $\lambda$ and CO is too noisy to show anything of particular interest. A small difference can be noted up- and downslope for THC, beyond the jumps due to changes in operating point.

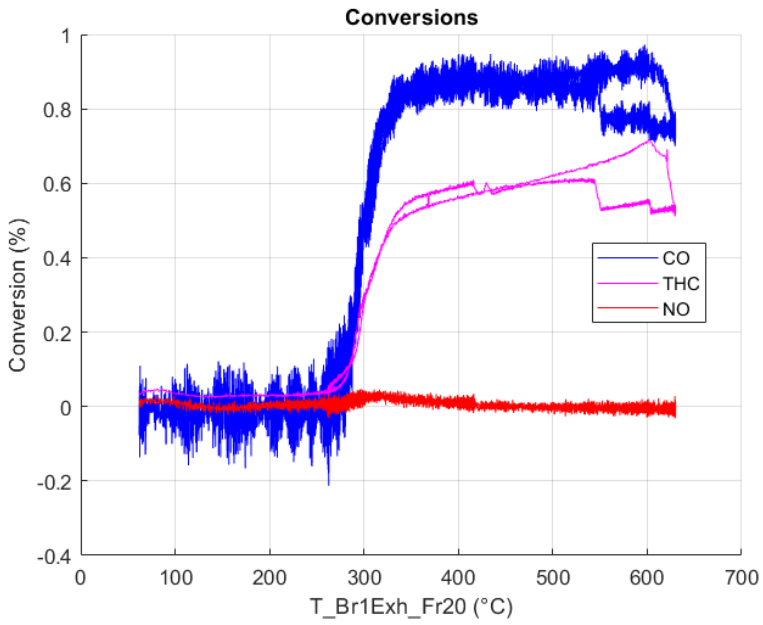


**Figure 4.12:** Conversions at $\lambda = 1.1$ using 30mm catalyst

If the $\lambda$:s are studied. it can be noted that Brettschneider-$\lambda$ oscillates during the period where the massflow is 17 g/s, i.e. when 1500 rpm is used, see Fig. 4.13. When the operating point is changed, giving an increase in massflow, this discrepancy is

no longer as prevalent. This suggests that there is a leakage affecting the $\lambda$-control. This means that there will in this particular case be slightly different $\lambda$ up- and downslope, resulting in non-equivalence in conversions. The observant eye might notice the slight discrepancy between up- and downslope using 17 g/s massflow.

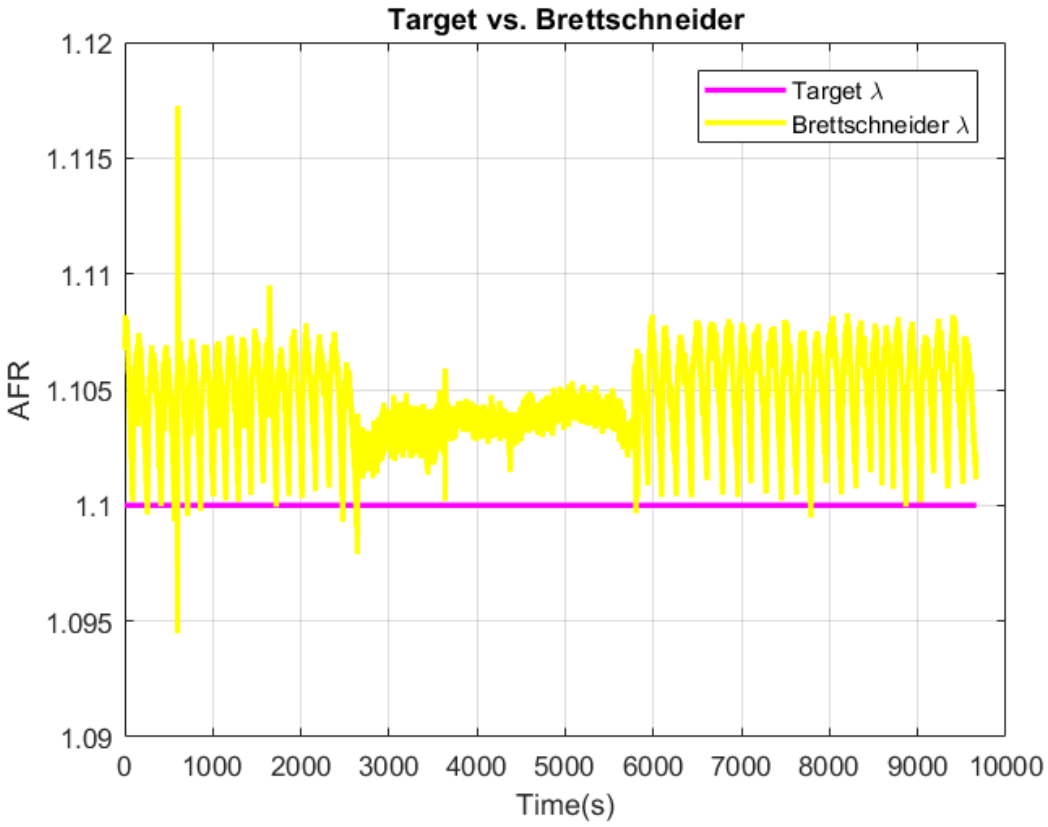


**Figure 4.13:** $\lambda$-discrepancy at $\lambda = 1.1$, using 30mm catalyst

For a retry experiment testing rich-pulsing influence, using engine speeds as displayed in Fig. 4.14 this behaviour became even more prominent. Notice the slight difference up- and downslope. Upslope uses 1540, while downslope uses 1501.

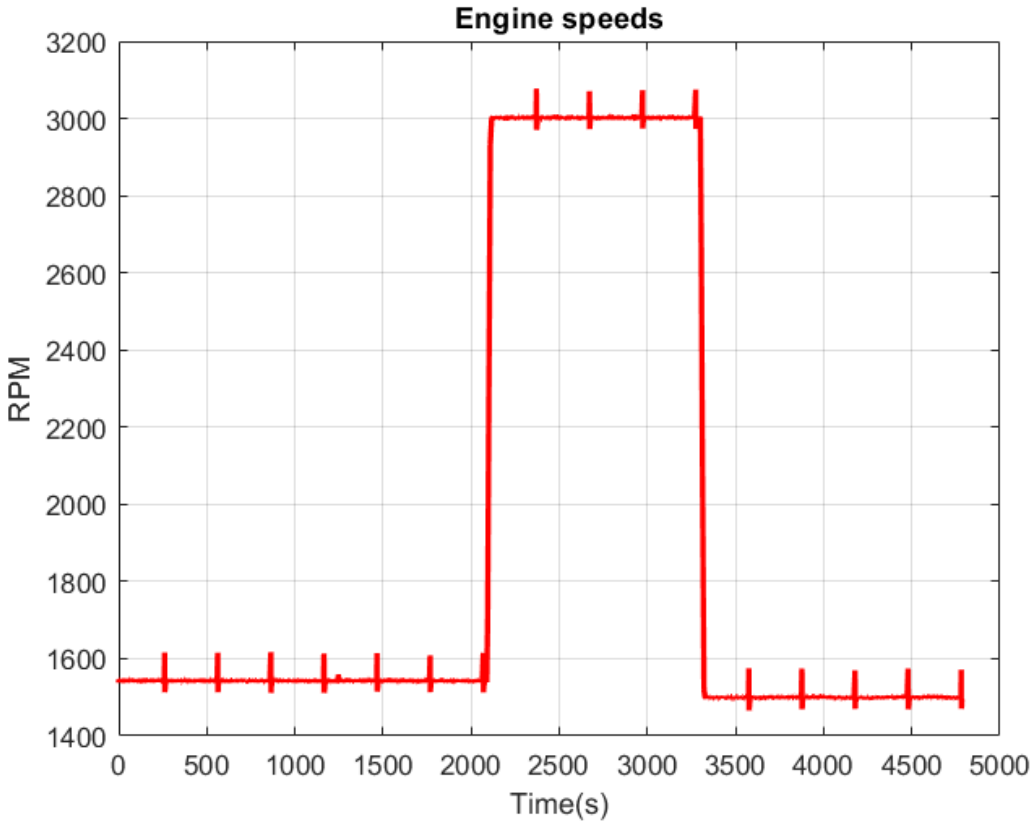


**Figure 4.14:** Retry experiment $\lambda = 1.1$: Engine speeds

While studying the target- vs. Brettschneider-$\lambda$, even though a similar massflow is used, a distinct difference can be seen, see Fig. 4.15

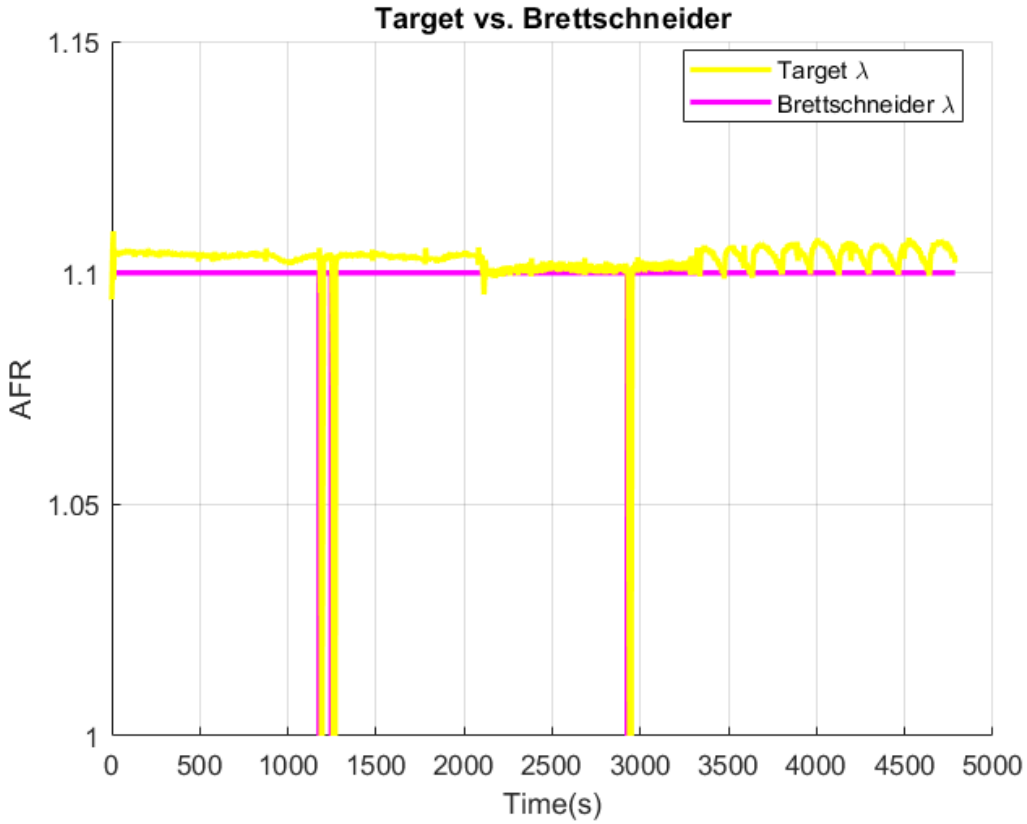


**Figure 4.15:** Retry: $\lambda$-discrepancy at $\lambda = 1.1$, using 30mm catalyst

Higher massflows result in more accurate matches between target and Brettschneider, while a lower massflow results in a slightly overpredicted value. Going downslope even gives an oscillatory behaviour. This is attributed to some sort of alias effect while sampling. For future reference, even though conversion graphs might suggest a system hysteresis, this can often be attributed to this feature.

## 4.5 Rich Side Performance Loss

To illustrate the phenomena of a potential poisoning effect, a 30mm $\lambda = 0.9$ experiment was considered a good candidate. In this experiment, actively pulsing lean $\lambda = 1.1$ was done at strategically adequate situations to see if a lean section could cleanse the catalyst.

The operating point is displayed in Fig. 4.16. The system was allowed to settle in between changes.

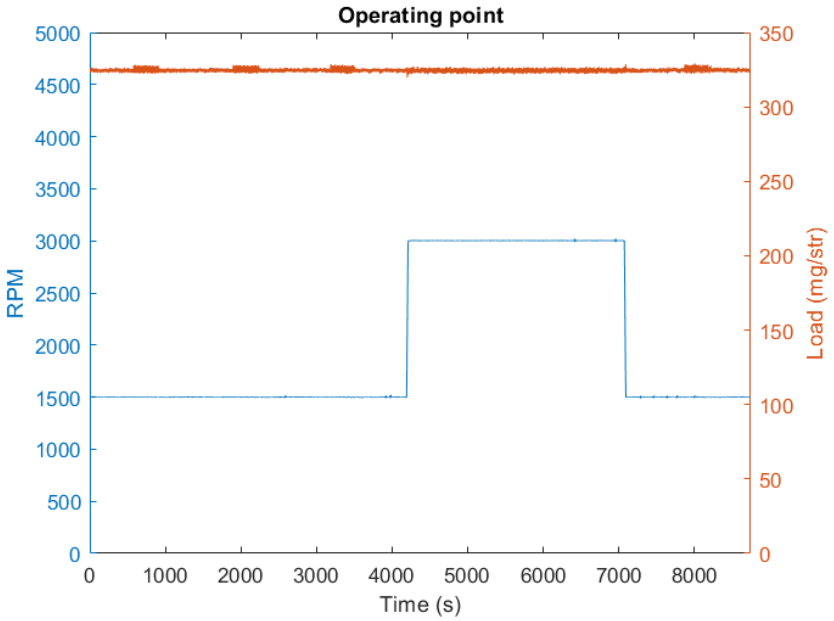


**Figure 4.16:** Operating point at $\lambda = 0.9$ using 30mm catalyst

Downslope was made in one step, synchronizing with the fan cooling. Temperature profiles are presented in Fig. 4.17. Distinct temperature peaks can be noted when lean pulsing.

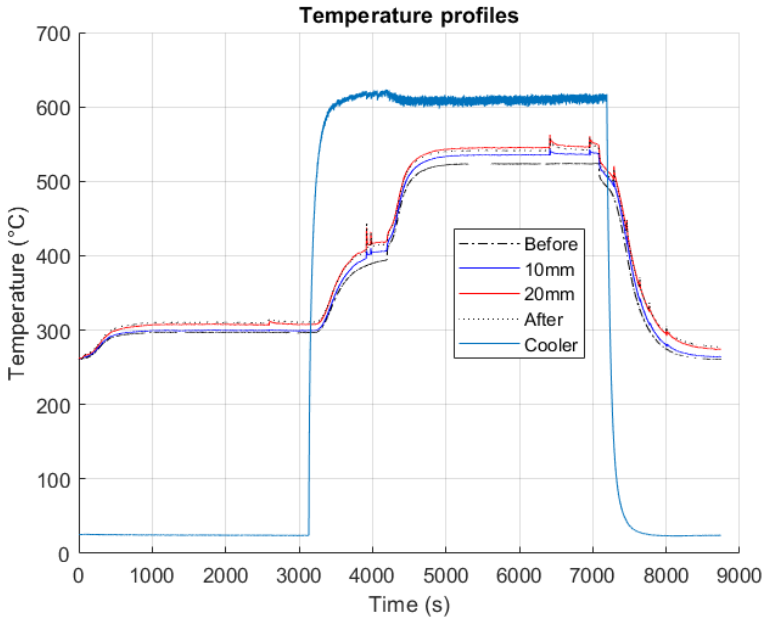


**Figure 4.17:** Temperatures at $\lambda = 0.9$ using 30mm catalyst

Emissions of the three main species can be seen in Fig. 4.18. Note that when lighting off, both CO and THC as well as NO start to show some conversion. Then suddenly, even though temperature increases, a conversion decrease can be noted. This effect is very prominent on CO, and could be explained by the equilibrium nature of the

WGS reaction. THC, in contrast to CO, also shows this behaviour, but to a lesser extent. CO shows a 1000 ppm difference, THC a 100 ppm difference.

One possible explanation could be that a coking effect (production of carbonaceous species) might light off here, occupying vacant noble metal sites. Note, lean pulses before light-off show no change. After light-off, after 6000s and beyond, a distinct conversion increase can be noted for all species when lean pulsing.

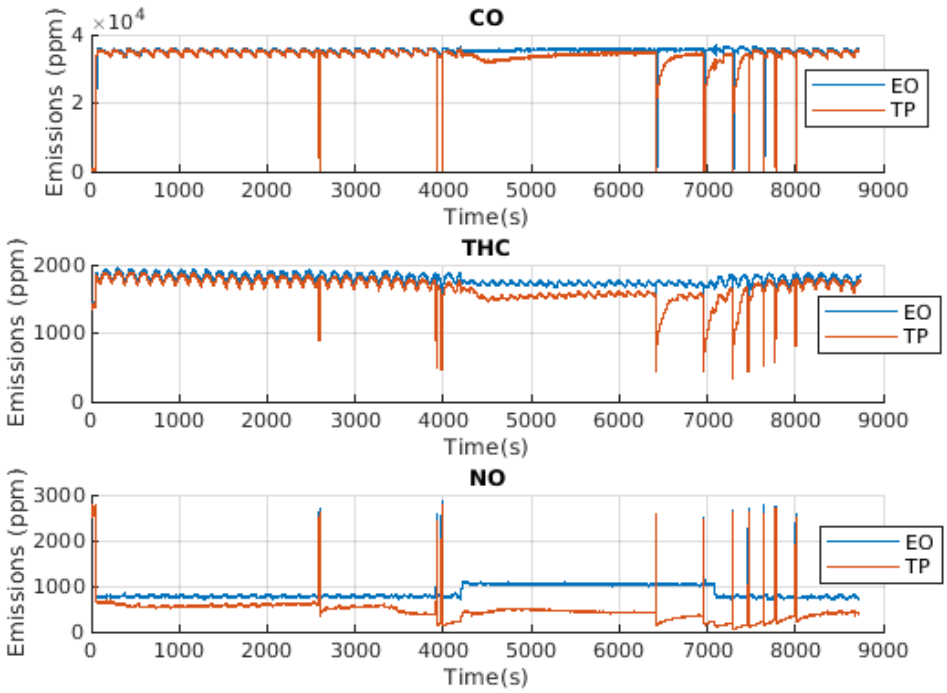


**Figure 4.18:** Emissions at $\lambda = 0.9$ using 30mm catalyst

Additionally, the $H_2$ TP measurement displays some interesting features, see Fig. 4.19. Before 4000s, it can be seen that lean steps shows a significantly lower amount of $H_2$, which is expected as the engine does not produce much $H_2$ at lean operating points. A slope increase can be noted at 4400s, which synchronizes with the CO profile seen in Fig. 4.18. Remember, this can be attributed to the equilibrium nature of the WGS.

After 4000s, lean pulsing displays a different behaviour from pre 4000s. Note that the graph initially drops, and then drastically increases to double its pre-pulsing value. The temperatures has now increased to such extent that the WGS (and also SR) has lighted off. The catalyst is affected by running extensively rich, and it is believed that purging the catalytic surface with $O_2$ is beneficial for these reactions to occur.

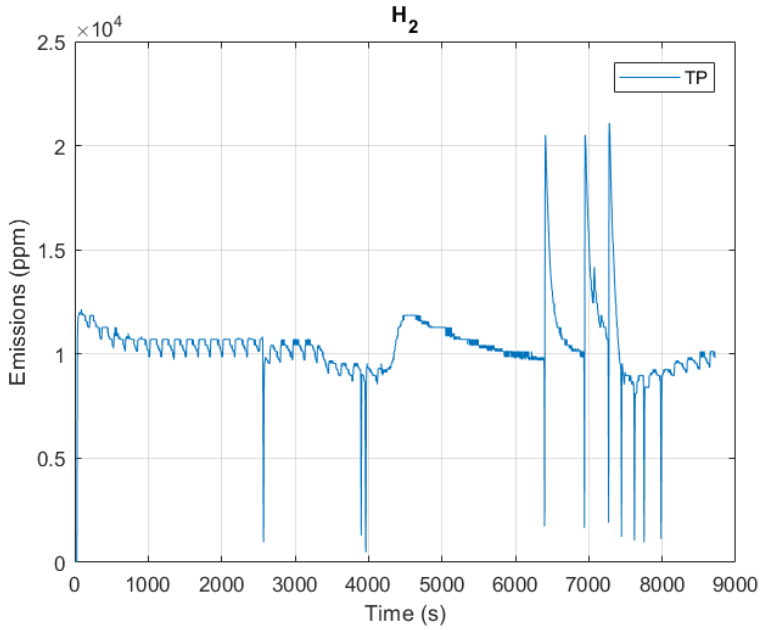


**Figure 4.19:** $H_2$ emissions at $\lambda = 0.9$ using 30mm catalyst

Similar behaviour was noted for all rich side $\lambda$ tested within this thesis. Running $\lambda = 1.0$ did not display this phenomena, suggesting that this is exclusive to rich side operation. It is a phenomena which similar to the reaction scheme proposed exhibit an exponential relation to temperature, as it suddenly just lights-off, inhibiting conversion for all species. This is problematic for optimization purposes, as the model does not have any inherent mechanism to cope with this type of behaviour.

# 5

# Optimization Results

This section houses information on the choice of data for optimization, its results and validation of the tuned model.

## 5.1 Obtained Tuning

Common setting used with the in-built MATLAB function, *lsqnonlin*, were,

1. DiffMinChange = 0.1
2. FiniteDifferenceStepSize = 1e-6
3. Lower bound(Pre-exponential factor, activation energy) = (0.1, 0.4)
4. Upper bound(Pre-exponential factor, activation energy) = (Inf, Inf)

Calculations were done by using an Intel Core i5 5200U 2.20GHz processor.

Note the third point in the above list. The activation energy had to be restricted to a lower bound of 0.4, where tuning it lower could in some cases degenerate the simulation, as a result of too high reaction rates. In the upcoming tables, it will be shown that the average simulation time increases when more reactions are active in combination with higher temperatures. More reactions lighting-off shows higher stiffness, which is reflected in the time steps taken by ode15s. A histogram displaying time steps is shown in Fig. 5.1 using the final tuning obtained. An interesting break point is 0.01, which was the static sampling time set in the SIMULINK model.

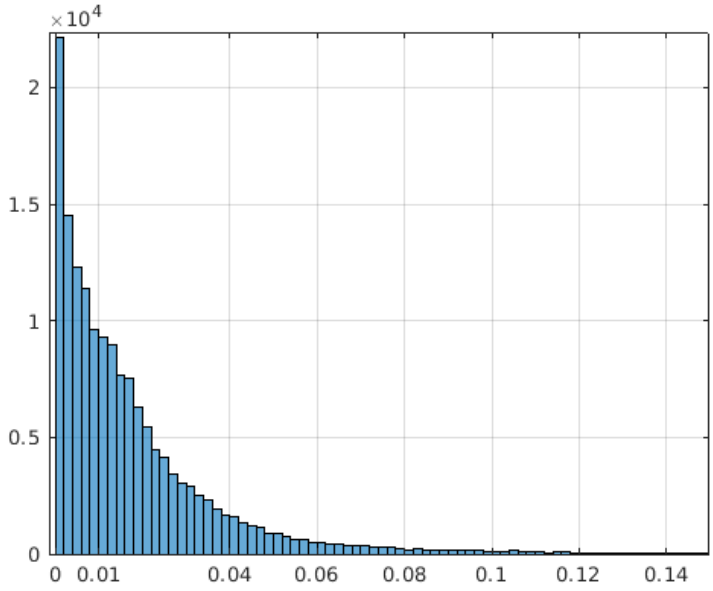


**Figure 5.1:** Histogram of time steps taken for the model to run through the training data

Also, recall the transformation of the model parameters

$$k_i = a_i \times A_i e^{\left(\frac{-e_i \times E_i}{RT_g}\right)} \tag{5.1}$$

where the procedure tunes for $a_i$ and $e_i$, rather than $A_i$ and $E_i$.

### 5.1.1 R1 to R4 reactions

The lean intervals during the catalyst light-off were incorporated into the objective function. Details regarding the optimization and the obtained tunings for reactions, $R_1$ to $R_4$ are given by tables 5.1 and 5.2 respectively.

| Iterations | Function calls per iteration | Objective value | | Experiment duration (secs) | Avg. Simulation time (secs) | Optimization duration |
|---|---|---|---|---|---|---|
| | | Start | End | | | |
| 20 | 9 | 435.401 | 18.9365 | 260 | 30 | 1hr 28mins |

**Table 5.1:** Optimization results for oxidation with $O_2$ reactions using 70mm catalyst experiment

| Kinetic parameters for R1-R4 | | | | | | | |
|---|---|---|---|---|---|---|---|
| $a_1$ | $e_1$ | $a_2$ | $e_2$ | $a_3$ | $e_3$ | $a_4$ | $e_4$ |
| 3.7566 | 0.8942 | 7.7903 | 0.8140 | 0.1025 | 2.3960 | 0.1001 | 0.4798 |

**Table 5.2:** Kinetic parameters for oxidation with $O_2$ reactions tuned using 70mm catalyst experiment

### 5.1.2 R5 to R7 reactions

The rich intervals during catalyst light-off were used to compute the objective function. Optimization details and the obtained tunings for reactions from $R_5$ to $R_7$ are shown in tables 5.3 and 5.4 respectively.

| Iterations | Function calls per iteration | Objective value | | Experiment duration (secs) | Avg. Simulation time (secs) | Optimization duration |
|---|---|---|---|---|---|---|
| | | Start | End | | | |
| 14 | 7 | 579.488 | 48.161 | 464 | 78 | 2hrs 7mins |

**Table 5.3:** Optimization results for reduction of $NO$ reactions using 70mm catalyst experiment

| Kinetic parameters for R5-R7 | | | | | |
|---|---|---|---|---|---|
| $a_5$ | $e_5$ | $a_6$ | $e_6$ | $a_7$ | $e_7$ |
| 1.0439 | 0.8374 | 1.0001 | 0.9990 | 1.0002 | 0.9987 |

**Table 5.4:** Kinetic parameters for reduction of $NO$ reactions tuned using 70mm catalyst experiment

### 5.1.3 R8 and R9 reactions

The region consisting of enhanced $CO$ and $THC$ conversions with $H_2$ production on rich intervals were used. Optimization details and the obtained tunings for reactions from $R_8$ and $R_9$ are shown in tables 5.5 and 5.6 respectively.

| Iterations | Function calls per iteration | Objective value | | Experiment duration (secs) | Avg. Simulation time (secs) | Optimization duration |
|---|---|---|---|---|---|---|
| | | Start | End | | | |
| 17 | 5 | 657.46 | 41.5635 | 772 | 145.18 | 3hrs 25mins |

**Table 5.5:** Optimization results for reduction of $NO$ reactions using 70mm catalyst experiment

| Kinetic parameters for R8-R9 | | | |
|---|---|---|---|
| $a_8$ | $e_8$ | $a_9$ | $e_9$ |
| 3.7411 | 0.9678 | 1.9265 | 0.4562 |

**Table 5.6:** Kinetic parameters for the water-gas shift and steam reforming reactions tuned using 70mm catalyst experiment

### 5.1.4 Ceria reactions

The tuning for the ceria reactions, R10 to R15 were not optimized due to the presence of sensor dynamics within the lean-to-rich (L2R) or rich-to-lean (R2L) transitions and hence, all tunings parameters were set to one. An example as to illustrate this can be seen in Fig. 5.2.

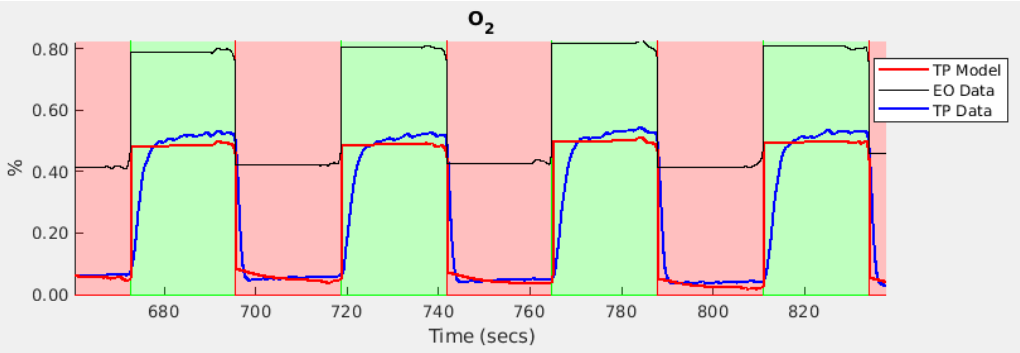


**Figure 5.2:** An illustration of four R2L and three L2R transitions - focusing on O2 emissions

The signals manipulation previously described, where the EO signal was manually designed to attain its final value (omitting the sensor dynamics completely - which was justified by the engines fast dynamic behaviour) can be seen by studying the black legend. This affects the red legend, which displays the model tailpipe signal. Due to mass convection through the catalyst, it instantly changes at a transition, to later attain its steady-state value as a first order response. This is most prominent at the L2R transitions. As the signals has been tinkered with, making a proper fit becomes nonsensical, as it would not be able to explain the dynamic behaviour of the instrument. Furthermore, it is not wished to mimic the instrument, but rather extract the true signal via some convolution technique, or similar. Accurate signals processing, recovering the original signal should be done prior to tuning the dynamic behaviour and transitions of the TWC. Due to lack of skill within this field, the final decision fell on not tuning the buffer. Additionally, there is also delays which has been troublesome, requiring faster instruments necessary to capture the delayed emissions at a transition. As for the sensors used within this thesis, the response is believed to be too long to capture any essential buffer behaviour.

Lastly, Fig. 5.3 shows the model accuracy on the training data using the tuned parameters. Green legend is lean, red is rich. The solid lines refer to the data while, the dashed lines refer to the model estimates.

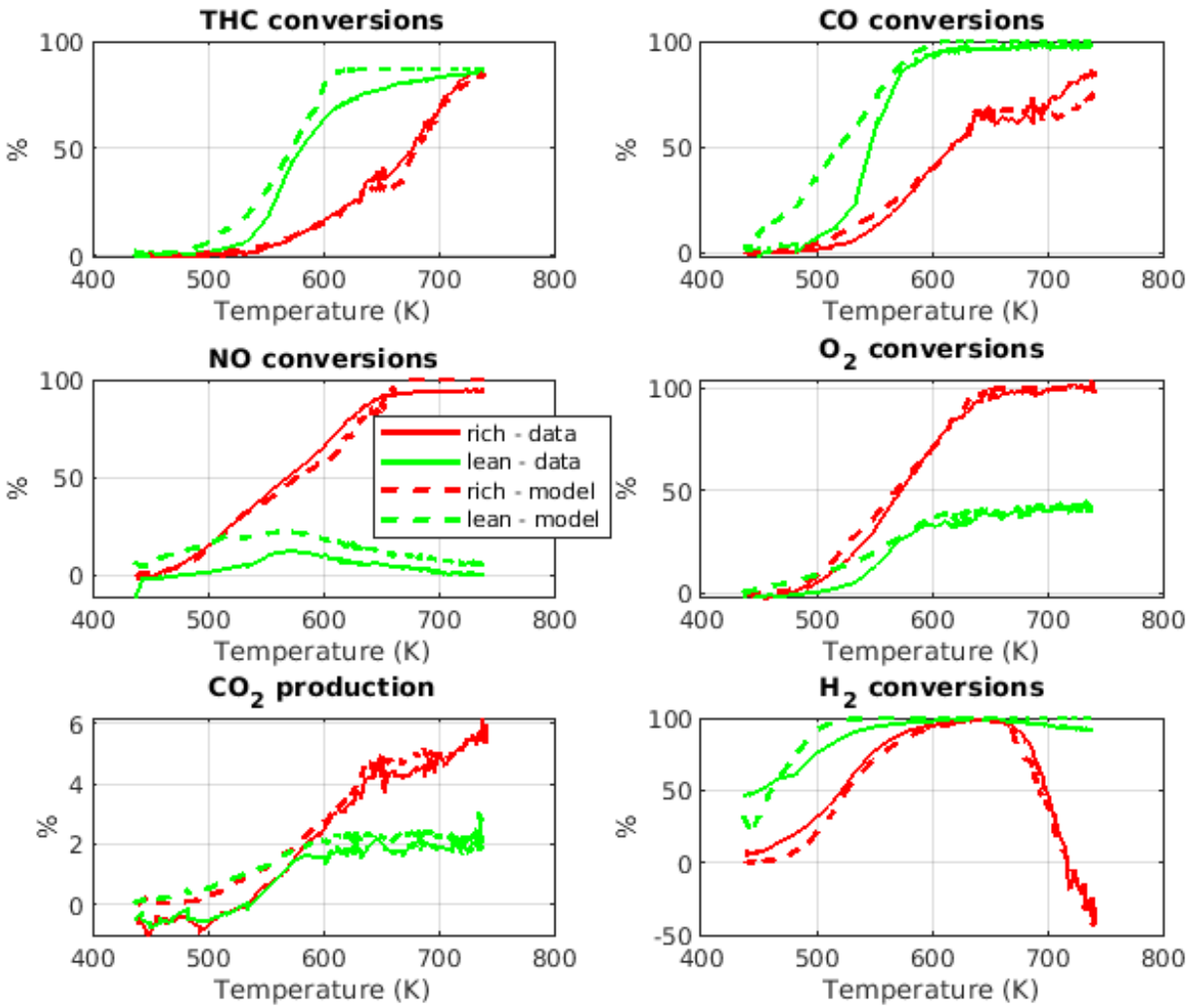


**Figure 5.3:** Species conversion with respect to temperature for the 70mm ± 2% with 17g/s bang-bang experiment

## 5.2 Model Validation

The achieved tuning was validated against a range of data, including an increased massflow and an increase in $\lambda$-amplitude, along with its 30mm counterpart. The 30mm and 15mm ±2% showed similar behaviour, hence only the 30mm is presented here. For the interested reader, the 15mm results can be found in the Appendix-section.

### 5.2.1 70mm with ± 2% $\lambda$-switches at 34g/s

This experiment was used for validation as it is very similar to the data used for optimization but with a higher mass flow. Unfortunately, this data lacks $H_2$ mea-

surements.

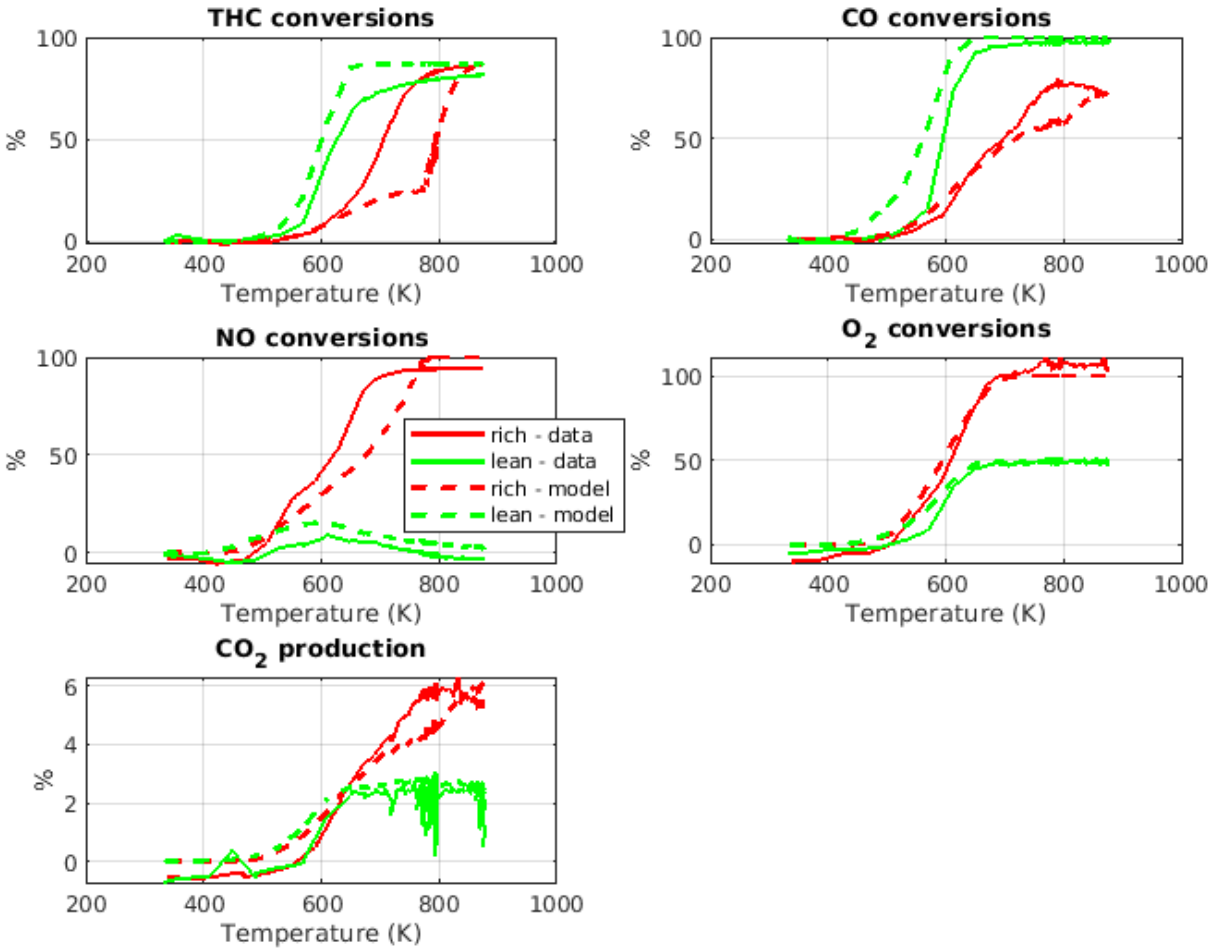


**Figure 5.4:** Species conversion with respect to temperature for the 70mm ± 2% with 34g/s bang-bang experiment

Generally, lean side shows satisfactory results, where light-offs are passably predicted. However, a slight overprediction can always be noted. Rich side is worse, especially for THC. Light-off capture is a failure, as a dramatic underprediction is always noted. It seems like the conversion recovers, for unknown reasons. It is unfortunate that $H_2$ is missing, as it surely holds valuable information to understanding this behaviour.

CO conversion starts declining at 800K, as a probable result of the WGS equilibrium, which the model fails to predict. NO consequently shows an underprediction, culminating in a 100% conversion, while the data suggests otherwise. This is likely attributed to the model not showing any mass transfer limitations.

### 5.2.2 70mm with ± 5% λ-switches

This is yet another 70mm catalyst heat up experiment with a larger lambda switches of ±5% as opposed to the ±2% data it was tuned for.

#### 5.2.2.1 17g/s

Fig. 5.5 shows the light-off region with a constant mass flow of 17g/s.

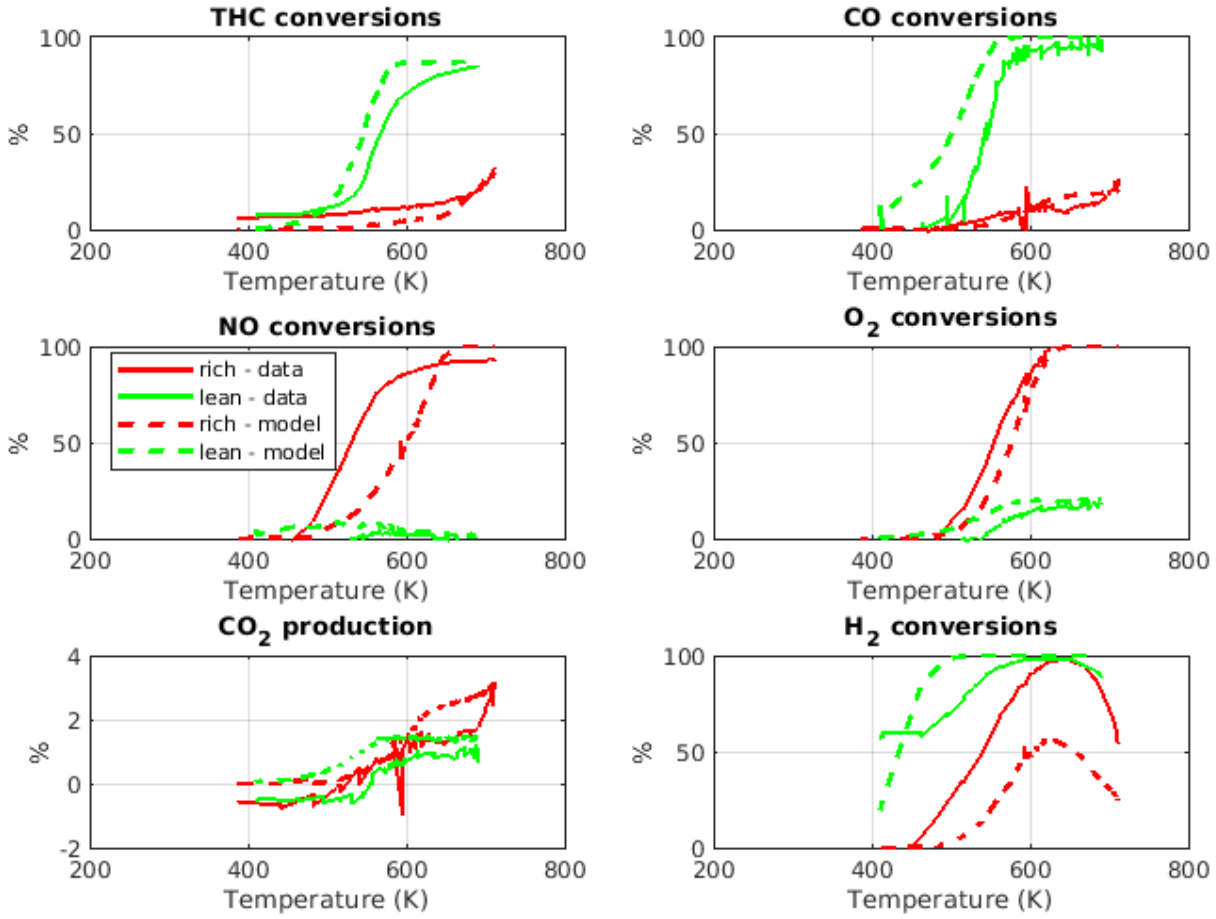


**Figure 5.5:** Conversion of species with respect to temperature for the 70mm ± 5% bang-bang experiment

There is a similar behaviour to the 70mm ±2% counterpart lean side, with exceptions on $H_2$. It seems like the data is erronous the initial few dozen degrees, as the data suggests a static 60% conversion.

Unfortunately the operating point was switched at 700K, which is too early since the $H_2$ lean side was still on a downslope and rich conversions for THC and CO still hadn't settled. This makes it difficult to draw any conclusions regarding THC and CO. As for NO, the results once again show an underprediction, culminating in

a 100% conversion. The $H_2$ measurements show a satisfactory shape, suggesting a good light-off tuning for the WGS and SR, but a distinct underprediction can still be noted.

#### 5.2.2.2 34g/s + 51g/s

This is part of the above experiment where the volume flow is increased from 17g/s to 34g/s and later to 51g/s. The graphs cover both 34 g/s and 51 g/s.

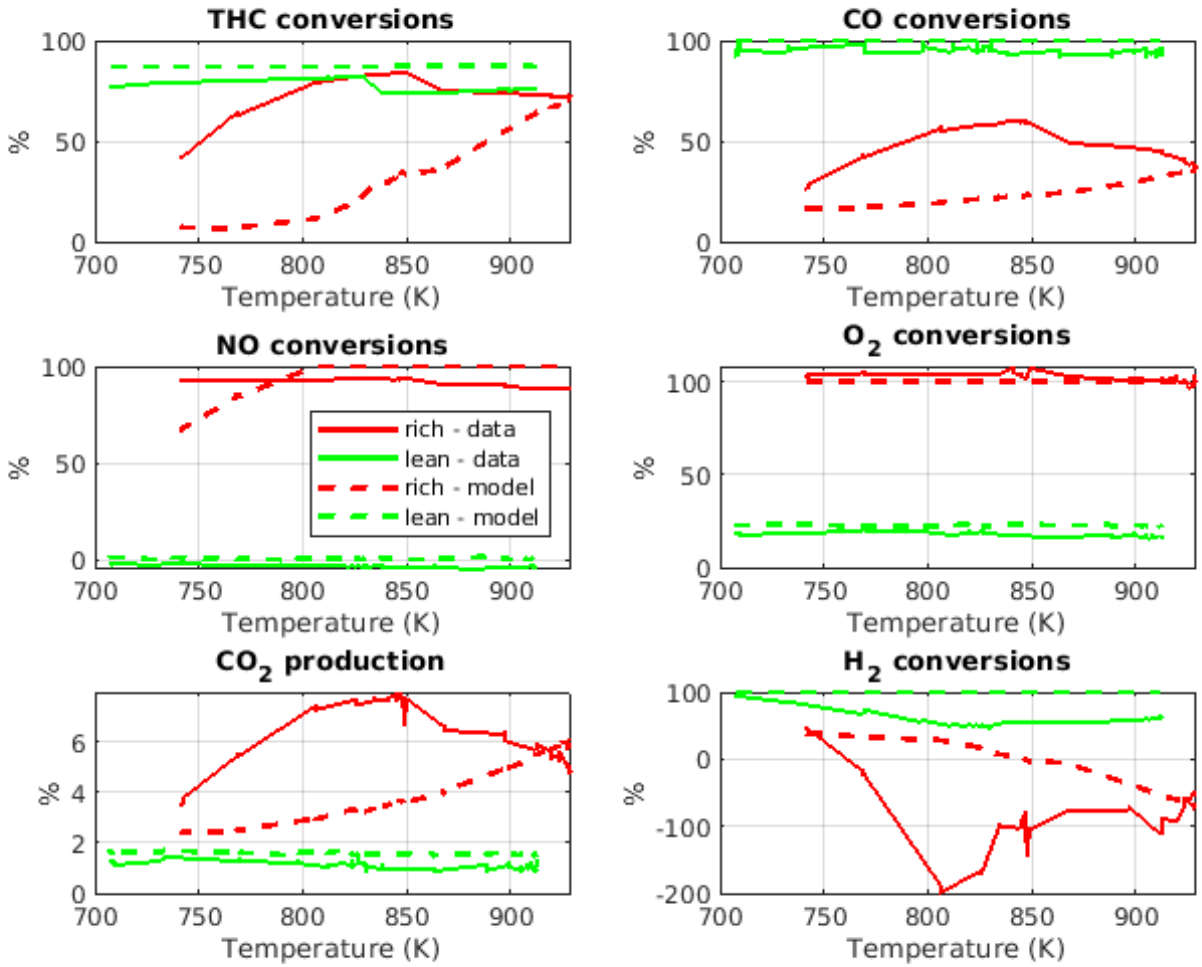


**Figure 5.6:** Conversion of species with respect to temperature for the 70mm ± 5% bang-bang experiment using flows of 34 and 51 g/s

At higher flows, there is a distinct loss in model prediction accuracy. Lean side is satisfactory, but is not attributed to the tuning, With an abundance of $O_2$ in combination with high temperatures, there isn't much data variety present - note the flat slopes. THC, CO and $H_2$ always show high conversions, while NO shows none.

Note that data $H_2$ lean side shows a decrease. In combination with the CO rich side declining shape, this suggests a WGS equilibrium settling. The model once again clearly fails to predict this behaviour.

To summarize the rich side: predictions are poor, with little to no match. The acquired tuning does not cover an operation this far from the tuning. Recall, not only the space velocity is different but also the $\lambda$-amplitude. A $\pm 5\%$ deviation suggests lean regions being leaner and rich regions being richer, in relation to $\pm 2\%$. In other words, the model is tuned for prediction closer to stochiometry.

### 5.2.3 30mm with $\pm$ 2% $\lambda$-switches

This experiment houses three different operating points including 1500, 3000 and 4500 rpm. Load is always set to 325 mg/str, this translates to mass flows 17, 34 and 51 g/s. Switching from a 70mm to 30mm gives space velocity increases, as the residence time within the catalyst shortens. Roughly speaking, a 17g/s experiment using a 30mm catalyst gives a space velocity equal to a 70mm 34g/s run.

#### 5.2.3.1 17 g/s

Conversions are displayed in Fig. 5.7.

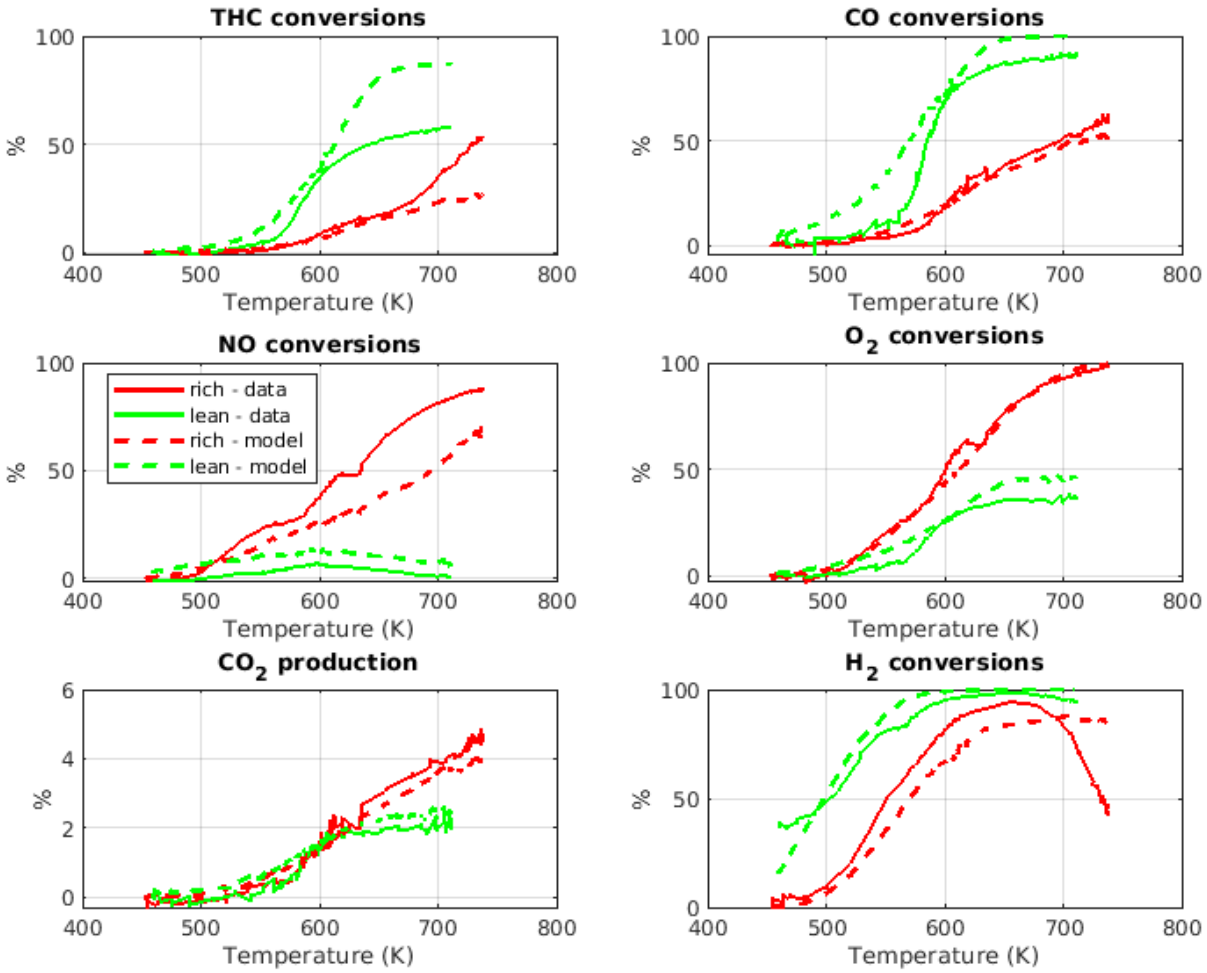


**Figure 5.7:** Conversion of species with respect to temperature for the 30mm ± 2% with 17g/s bang-bang experiment

Starting with lean side, as usual, the model tends to overpredict the conversions, which partly can be attributed to lacking mass transfer descriptions. Also, the tuning can of course be questioned. Even though THC light-off is well captured the steady-state final conversion is off by ∼30%. Rich side experiments would've benefitted from additional run time, as species THC, CO and NO are still on their upslope.

It is interesting to put this experiment in relations to 70mm ±2% 34g/s, which show a similar space velocity. They look fairly similar, but it is difficult to make a proper comparison as the temperature range is slightly different. 70mm ±2% 34g/s went up to 850K, here we only go up to 750K.

#### 5.2.3.2 34 g/s

Looking at the graphs below, it is quite clear that the tuning is not adequate for this space velocity. Temperature ranges between 710-860K, and non-existent slopes can

be noted. THC conversion has a 30% offset lean side, and 40% offset rich side. Once more, the WGS equilibrium gives CO and $H_2$ their characteristic rich side shapes.

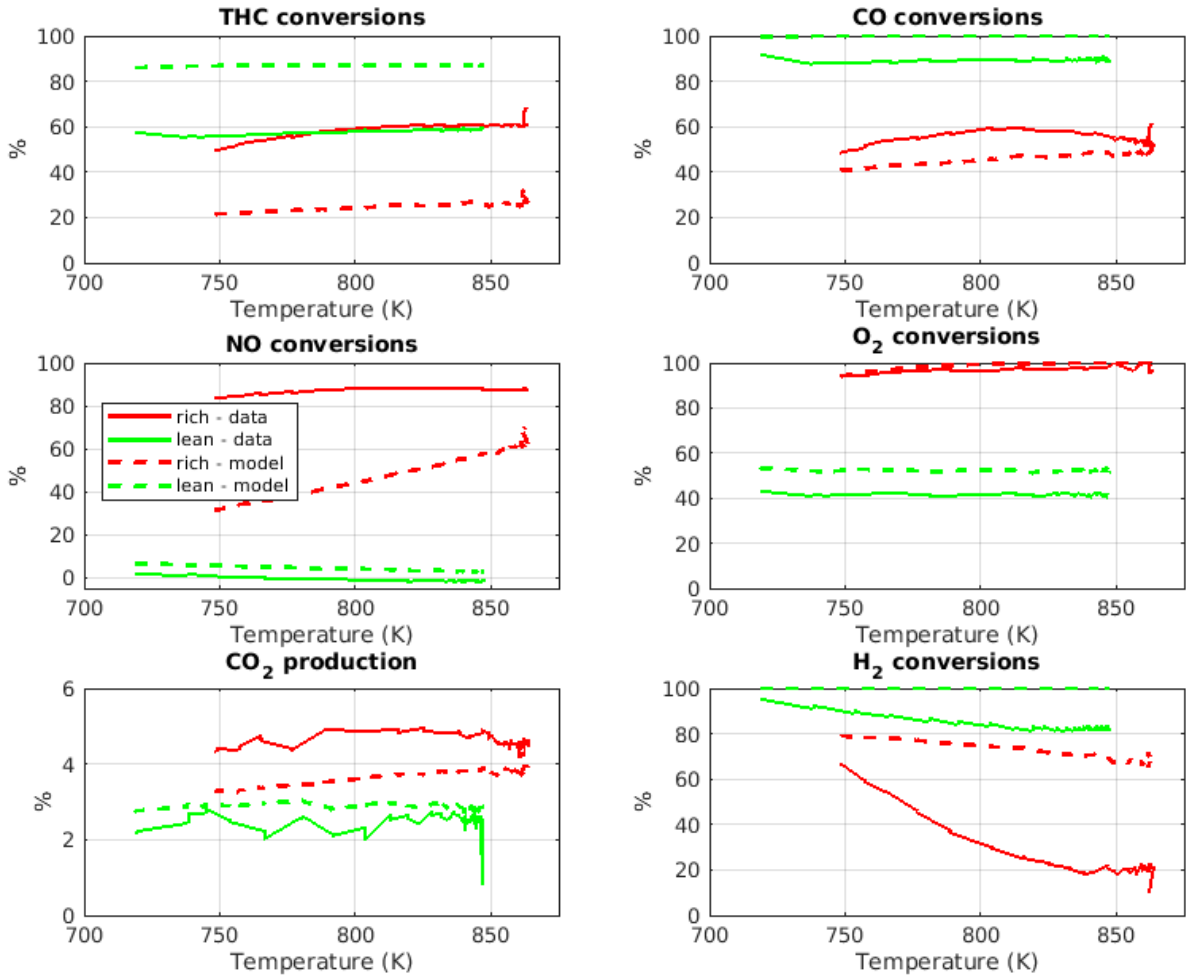


**Figure 5.8:** Conversion of species with respect to temperature for the 30mm ± 2% with 34g/s bang-bang experiment

### 5.2.4 A Final Remark

The achieved tuning is obviously biased towards the training data, where it shows a great match. Stretching outwards onto operating points beyond this, gives different outcomes, but some general trends can be noted and commented.

- "Higher" temperatures usually shows 100% (or high) conversions for all relevant species (i.e. CO and THC lean side, NO rich side).
- A difficulty to mimic WGS equilibrium dynamics is displayed throughout all experiments.
- Stretching to bigger $\lambda$-spans (such as $\pm 5\%$) gave poor performance, as the operating point is too far from stoichiometry.

- Lean sides usually gave better matches than rich side, maybe due to an abundance of $O_2$ making R1-R4 dominate. An exception was $H_2$ which could be attributed to the training data lacking full light-off information for this species.

Additionally, it is difficult to make predictions at the higher temperature range, which is difficult to define, but occurs somewhere close to 750K. A range of space velocities can give satisfying predictions, but only before reaching the max steady-state conversion value, i.e. during the light-off phase. It seems like the prediction problem lies in high temperatures, rather than high space velocities. In hindsight, the model should've been trained with several more experiments to be able to cope with more operating points, making it more diverse.

# 6
# Conclusion

As expected, the model fails its predictions when the mass transfer limits the conversion. As long as there is an abundance of agents, in combination with high temperatures, the model is able to sweep all pollutants. In many situations this results in either a 100% conversion of CO lean side or NO rich side, to give a few examples. To resolve this issue, a task for future works would be to design a mass transfer limitations within the model, which could be some type of diffusion mechanism. This could include internal- as well as external mass transfer, which is a topic covered extensively in literature.

In Auckenthaler's thesis [6], a reaction mechanism for the coking phenomena is suggested. It is apparent that the model would also benefit from this design, to be able to deal with rich side poisoning. Auckenthaler makes a distinction between ceria sites and noble metal sites, and uses several phases to handle diffusion properly. A suggestion for future works would hence be to study that thesis thoroughly, to be able to account for the two above mentioned phenomena the model lacks information about.

Optimization has shown improvement, but lacks some flair, as it only manages to cover the particular operating point it has been optimized for. *lsqnonlin* is prone to get stuck in local minima, leading to poor predictions outside the scope of optimization. Using the same massflow for a different catalyst size also shows poor matching, especially for WGS and SR. A suggestion for future works would hence be to test a global algorithm, such as the genetic algorithm, $ga()$, to find better solutions. Addition of multiple experiments into the routine could also benefit the outcome.

Also, this thesis only focused on optimizing for the reactions, omitting the inhibition terms. These clearly influence the behaviour, and should be an addition to the optimization routine. These were omitted by a means to simplify the problem. If it is considered interesting to go with a model housing an inhibition factor, a future works would hence be to figure out how to properly make this addition to the routine. Ramanathan [4] might be a probable starting point for investigations.

Regarding the buffer reactions, R10-R15, optimization has been a redundant task, as the data used was not handled properly for the detail required by those reactions. The delays were handled using a constant time. The dynamics were only accounted for using the EO signal. The dynamics for the TP-signal required some

sophisticated convolution techniques, beyond our skill. At all times the TP-signal has been used it has hence been so untruthfully, as it houses the dynamics of the instruments alongside it. Future works would be to handle the signals processing in a more professional manner, such that the true signal data would be extracted from the collected data. Additionally, it is believed that the delay time might be a function of the operating point, hence it would be valuable to find that relation for even better signals processing.

The procedure by using feedforward bang-bang was shown superior to studying constant $\lambda$. The former strategy gave information on both rich and lean side steady-states, as well as R2L and L2R transitions. Hydrogen measurements were shown to be key, as it showed valuable information about the poisoning phenomena as well as when WGS and SR lighted off. However, having the system separated from MEXA was shown problematic, as tedious data handling increased analysis difficulties. Prior to learning the facets of the instruments, a lot of poor measurements were taken, not suitable for MATLAB use. It was of course a downside not to be able to measure both EO and TP, simultaneously, but a LUT was accurate enough for the purpose of this thesis. Additional $H_2O$ measurements would refine the analysis even further, and should be considered for future works.

This thesis leaves a MATLAB implemented model, along with plotting scripts and an optimization routine, to be used for further refinement. The MATLAB version shows increased stability properties, in contrast to its SIMULINK counterpart. It allows for an arbitrary choice of slicing. Suggestion on improvements have been made, to study catalyst behaviour even further. Data handling, including signals processing, is very important, and can't be stressed enough. A restricted amount of operating points was chosen for this thesis, including one engine load and four engine speeds. This should be extended to cover a wider range. For studies on mass transfer limitations, higher temperatures are necessary and hence the engine has to be pushed even further.

Choosing three different catalyst sizes has conceptually shown to be interesting, despite the fact that the smaller catalyst sizes showed unsatisfactory results when optimizing. The 70mm thermocouple data suggested that the reactions finish roughly 40mm in, meaning that sizes below this should be focused on when finding sensitive data for tuning purposes. The task of refining the optimization routine is left for future works.

This thesis also leaves the task of controlling the OBL. Another approach of future works would be to focus on the control aspect, rather than the modelling aspect. However, a controller requires a model, and hence it would be deceptive to design a controller without having a properly designed model first. The most important message to take from this thesis is the methods which has been proposed. Feedforward bang-bang and heat-exchanging using different catalyst sizes can give valuable data, as long as the signals processing alongside it is on par.

# Bibliography


[1] Oak Ridge National Laboratory CC BY 2.0 (https://creativecommons.org/licenses/by/2.0/?ref=ccsearch&atype=rich). Catalytic converter, December 2009. URL https://www.flickr.com/photos/oakridgelab/4293629922. [Online; accessed July 21, 2021].

[2] Michael Handrich - Own work, CC BY-SA 3.0 (https://creativecommons.org/licenses/by-sa/3.0/). A planar zirconia sensor (schematic picture), June 2010. URL https://commons.wikimedia.org/w/index.php?curid=10781084. [Online; accessed July 07, 2021].

[3] Michael Handrich - Own work, CC BY-SA 3.0 (https://creativecommons.org/licenses/by-sa/3.0/). A planar wide-band zirconia sensor (schematic picture), June 2010. URL https://commons.wikimedia.org/w/index.php?curid=10757452. [Online; accessed July 07, 2021].

[4] Karthik Ramanathan and Chander Shekhar Sharma. Kinetic parameters estimation for three way catalyst modeling. *Industrial & Engineering Chemistry Research*, 50(17):9960–9979, 2011. doi: 10.1021/ie200726j. URL https://doi.org/10.1021/ie200726j.

[5] Pascal Kiwic. *Model-Based Control of Catalytic Converters*. PhD thesis, Swiss Federal Institute of Technology in Zurich, Sonneggstrasse 3, November 2012. https://doi.org/10.3929/ethz-a-007593810.

[6] Theophil Auckenthaler. *Modelling and control of three-way catalytic converters*. PhD thesis, Swiss Federal Institute of Technology in Zurich, Sonneggstrasse 3, July 2005. https://doi.org/10.3929/ethz-a-005011053.

[7] J. Heywood. *Internal Combustion Engine Fundamentals 2E*. McGraw-Hill Education, 2018. ISBN 9781260116113. URL https://books.google.se/books?id=0mJUDwAAQBAJ.

[8] Irman Svraka and Linus Österdahl Wetterhag. Model Based Catalyst Control. Master's thesis, Linköping University, Linköping, Sweden, 2019.

[9] European Environment Agency (EEA). Air quality in europe - 2020 report, 2020. URL https://www.eea.europa.eu//publications/air-quality-in-europe-2020-report.

[10] World Health Organization. *World Health Statistics - Monitoring Health for the SGDs 2020*. World Health Organization, Avenue Appia 20, Geneva, 2020.

[11] United Nations. *Sustainable Development Goals - Goal 13*. https://www.un.org/sustainabledevelopment/climate-change/, .

[12] United Nations. *Sustainable Development Goals - Goal 3*. https://www.un.org/sustainabledevelopment/health/, .

[13] European Parliament and of the Council. Regulation (EC) no 715/2007 on type approval of motor vehicles with respect to emissions from light passenger and commercial vehicles (Euro 5 and Euro 6) and on access to vehicle repair and maintenance information, June 2007. URL https://eur-lex.europa.eu/legal-content/EN/TXT/?uri=CELEX:32007R0715.

[14] European Parliament and of The Council. Implementing and amending Regulation (EC) no 595/2009 with respect to emissions from heavy duty vehicles (Euro VI) and amending Annexes I and III to Directive 2007/46/EC, May 2011. URL https://eur-lex.europa.eu/eli/reg/2011/582/oj.

[15] European Parliament and of The Council. Regulation (EU) 2019/631 of the European Parliament and of the Council on setting $CO_2$ emission performance standards for new passenger cars and for new light commercial vehicels, and repealing Regulations (EC) No 443/2009 and (EU) No 510/2011, April 2019. URL https://eur-lex.europa.eu/legal-content/EN/TXT/?uri=CELEX%3A02019R0631-20210301.

[16] Dieter Quartier. Do you know your Euro 6 from your 6c and 6d-TEMP?, 2018. URL https://www.fleeteurope.com/fr/new-energies-fiscalite-et-legislation/europe/features/do-you-know-your-euro-6-your-6c-and-6d-temp?

[17] Choongsik Bae and Jaeheun Kim. Alternative fuels for internal combustion engines. *Proceedings of the Combustion Institute*, 36(3):3389–3413, 2017. ISSN 15407489. doi: 10.1016/j.proci.2016.09.009. URL http://dx.doi.org/10.1016/j.proci.2016.09.009.

[18] Zissis Samaras. Light-duty vehicle (LDV) exhaust. 9th Advisory Group on Vehicle Emission Standards (AGVES) Online Meeting, April 2021. URL https://circabc.europa.eu/ui/group/f57c2059-ef63-4baf-b793-015e46f70421/library/83a09cc8-7f8f-4ca6-9764-0b77da57d4cc/details.

[19] Association for Emission Control by Catalyst (AECC). AECC position paper on Euro 7/VII emission standards, July 2020. URL https://www.aecc.eu/resources/position-papers/. [Online; accessed July 08, 2021].

[20] Z. Samaras, S. Hausberger, and G. Mellios. Preliminary findings on possible Euro 7 emission limits for LD and HD vehicles. 6th Advisory Group on Vehicle Emission Standards (AGVES) Online Meeting, October 2020. URL https://circabc.europa.eu/ui/group/f57c2059-ef63-4baf-b793-015e46f70421/library/fdd70a2d-b50a-4d0b-a92a-e64d41d0e947/details.

[21] *Engine—Introduction*, chapter 4, pages 67–80. John Wiley and Sons, Ltd, 2014. ISBN 9781118536186. doi: https://doi.org/10.1002/9781118536186.ch4. URL https://onlinelibrary.wiley.com/doi/abs/10.1002/9781118536186.ch4.

[22] Pankaj Kumar, Imad Makki, James Kerns, Karolos Grigoriadis, Matthew Franchek, and Vemuri Balakotaiah. A low-dimensional model for describing the oxygen storage capacity and transient behavior of a three-way catalytic converter. *Chemical Engineering Science*, 73:373–387, 2012. ISSN 00092509. doi: 10.1016/j.ces.2011.12.001. URL http://dx.doi.org/10.1016/j.ces.2011.12.001.

[23] Helder Santos and Mário Costa. Influence of the three way catalytic converter substrate cell density on the mass transfer and reaction resistances. *Chemical Engineering Science*, 107:181–191, 2014. ISSN 00092509. doi: 10.1016/j.ces.2013.12.014. URL http://dx.doi.org/10.1016/j.ces.2013.12.014.

[24] Shawn Rood, Salvador Eslava, Alexis Manigrasso, and Chris Bannister. Recent advances in gasoline three-way catalyst formulation: A review. *Proceedings of the Institution of Mechanical Engineers, Part D: Journal of Automobile Engineering*, 234(4):936–949, 2020. ISSN 09544070. doi: 10.1177/0954407019859822.

[25] David R. Monroe, Martin H. Krueger, Donald D. Beck, and Michael J. D'Aniello. The effect of sulfur on three-way catalysts. *Studies in Surface Science and Catalysis*, 71(C):593–616, 1991. ISSN 01672991. doi: 10.1016/S0167-2991(08)63005-0.

[26] Pooya Tabib Zadeh Adibi. *Studies of catalyst sintering during operating conditions*. Licentiate thesis, Chalmers University of Technology, Göteborg, Sweden, 2004.

[27] J. Bickel, B. Odendall, G. Eigenberger, and U. Nieken. Oxygen storage dominated three-way catalyst modeling for fresh catalysts. *Chemical Engineering Science*, 160:34 – 53, 2017. ISSN 0009-2509. doi: https://doi.org/10.1016/j.ces.2016.11.016. URL http://www.sciencedirect.com/science/article/pii/S0009250916306108.

[28] R. Schrader. Lambda calculation brettschneider equation, March 2007. URL https://www.bridgeanalyzers.com/air-fuel-ratio/.

[29] Saurabh Y Joshi, Michael P Harold, and Vemuri Balakotaiah. Low-dimensional models for real time simulations of catalytic monoliths. *AIChE Journal*, 55 (7):1771–1783, 2009. doi: https://doi.org/10.1002/aic.11794. URL https://aiche.onlinelibrary.wiley.com/doi/abs/10.1002/aic.11794.

[30] Pankaj Kumar, Tian Gu, Karolos Grigoriadis, Matthew Franchek, and Vemuri Balakotaiah. Spatio-temporal dynamics of oxygen storage and release in a three-way catalytic converter. *Chemical Engineering Science*, 111(x):180–190, 2014. ISSN 00092509. doi: 10.1016/j.ces.2014.02.014. URL http://dx.doi.org/10.1016/j.ces.2014.02.014.

[31] H. Santos and M. Costa. Modelling transport phenomena and chemical reactions in automotive three-way catalytic converters. *Chemical Engineering Journal*, 148(1):173–183, 2009. ISSN 13858947. doi: 10.1016/j.cej.2008.11.047.

[32] H. Santos and M. Costa. The relative importance of external and internal transport phenomena in three way catalysts. *International Journal of Heat and Mass Transfer*, 51(5-6):1409–1422, 2007. ISSN 00179310. doi: 10.1016/j.ijheatmasstransfer.2007.11.005.

[33] Nikunj Gupta and Vemuri Balakotaiah. Heat and mass transfer coefficients in catalytic monoliths. *Chemical Engineering Science*, 56(16):4771–4786, 2001. ISSN 00092509. doi: 10.1016/S0009-2509(01)00134-8.

[34] Edward Jobson, Ove Hjortsberg, S. Lennart Andersson, and Ingemar Gottberg. Reactions over a double layer tri-metal three-way catalyst. *SAE Technical Papers*, (412), 1996. ISSN 26883627. doi: 10.4271/960801.

[35] T. Bäroth, A. Drochner, H. Vogel, and M. Votsmeier. Effect of Diverse Hydrocarbons on the Cold Start Behavior of Three-Way Catalysts. *Topics in Catalysis*, 60(3-5):278–282, 2017. ISSN 15729028. doi: 10.1007/s11244-016-0609-8.

[36] G. N. Pontikakis, G. S. Konstantas, and A. M. Stamatelos. Three-way catalytic converter modeling as a modern engineering design tool. *Journal of Engineering for Gas Turbines and Power*, 126(4):906–923, 2004. ISSN 07424795. doi: 10.1115/1.1787506.

[37] Theophil S. Auckenthaler, Christopher H. Onder, and Hans P. Geering. Online estimation of the oxygen storage level of a three-way catalyst. *SAE Technical Papers*, 2004(724), 2004. ISSN 26883627. doi: 10.4271/2004-01-0525.

[38] Dimitrios N. Tsinoglou, Grigorios C. Koltsakis, and James C. Peyton Jones. Oxygen storage modeling in three way catalytic converters. *Industrial and Engineering Chemistry Research*, 41(5):1152–1165, 2002. ISSN 08885885. doi: 10.1021/ie010576c.

[39] G. C. Koltsakis, P. A. Konstantinidis, and A. M. Stamatelos. Development and application range of mathematical models for 3-way catalytic converters. *Applied Catalysis B: Environmental*, 12(2-3):161–191, 1997. ISSN 09263373. doi: 10.1016/S0926-3373(96)00073-2.

[40] P. Atkins, J. de Paula, and R. Friedman. *Quanta, Matter, and Change: A Molecular Approach to Physical Chemistry*. OUP Oxford, 2009. ISBN 9780199206063. URL `https://books.google.se/books?id=QbQJAgAAQBAJ`.

[41] Sterling E. Voltz, Charles R. Morgan, David Liederman, and Solomon M. Jacob. Kinetic Study of Carbon Monoxide and Propylene Oxidation on Platinum Catalysts. *Industrial and Engineering Chemistry Product Research and Development*, 12(4):294–301, 1973. ISSN 01964321. doi: 10.1021/i360048a006.

[42] Pankaj Kumar and Imad Makki. Model Based Control of a Three-way Catalytic Converter Based on the Oxygen Storage Level of the Catalyst. *SAE Technical Papers*, 2017-March(March), 2017. ISSN 01487191. doi: 10.4271/2017-01-0960.

[43] C.L. Yaws. *Chemical Properties Handbook: Physical, Thermodynamics, Environmental Transport, Safety & Health Related Properties for Organic &*. Chemical engineering books. McGraw-Hill Education, 1999. ISBN 9780070734012. URL https://books.google.se/books?id=PH2KG4cbtzYC.

[44] Daniel C. Harris. *Quantative Chemical Analysis*. W. H. Freeman and Company, 8th edition, 2010. ISBN 978-1-4292-1815-3.

[45] HORIBA. Magneto-pneumatic analysis. URL https://www.horiba.com/en_en/products/by-technique/material-characterization/magneto-pneumatic-analysis/.

[46] V&F Analyse und Messtechnik GmbH. Technical description: IMR-MS - How it works, 2016.

[47] Mathworks Documentation. lsqnonlin - solve nonlinear least-squares (nonlinear data-fitting) problems. URL https://se.mathworks.com/help/optim/ug/lsqnonlin.html.

[48] S. Koteswara Rao, Rayees Imam, Karthik Ramanathan, and S. Pushpavanam. Sensitivity analysis and kinetic parameter estimation in a three way catalytic converter. *Industrial and Engineering Chemistry Research*, 48:3779–3790, 4 2009. ISSN 08885885. doi: 10.1021/ie801244w.

[49] Jonas Sjöblom. *Parameter estimation in heterogeneous catalysis*. PhD thesis, Chalmers University of Technology, Chalmersplatsen 4, April 2009. ISBN: 9789173852715.

# A

# Kinetic Parameters

**Table A.1:** Original kinetic parameters as proposed by Ramanathan et. al [4]

| Reaction | Activation energy $E_a$ (J/mol) | Pre-exponential factor $A$ (1/s) | Enthalpy $H$ (J/mol) |
|---|---|---|---|
| 1 | 111 450 | 4.21e13 | -2.83e5 |
| 2 | 129 530 | 1.02e15 | -1.93e6 |
| 3 | 165 150 | 4.68e10 | -2.04e6 |
| 4 | 111 450 | 4.21e13 | -2.42e5 |
| 5 | 52 374 | 1.19e9 | -3.73e5 |
| 6 | 90 063 | 6.2e10 | -2.74e6 |
| 7 | 69 237 | 6.1e9 | -3.32e5 |
| 8 | 56 720 | 1.8e5 | -4.12e4 |
| 9 | 81 920 | 1.23e5 | 3.74e5 |
| 10 | 5 296 | 9.78e-1 | -2.00e5 |
| 11 | 25 101 | 4.61e1 | -1.90e5 |
| 12 | 21 768 | 5.05e0 | -1.83e5 |
| 13 | 39 070 | 2.27e3 | -4.77e5 |
| 14 | 39 680 | 2.25e3 | -4.95e5 |
| 15 | 21 768 | 5.05e0 | -1.42e5 |

**Table A.2:** Inhibition term parameters as proposed by Ramanathan [4] et. al

| Inhibition factor term | Kinetic parameter $k_{i,G}$ | Exponential term $E_{i,G}$ (K) |
|---|---|---|
| 1 | -485 $\left(\frac{m^3}{mol}\right)$ | 7.33e0 |
| 2 | 166 $\left(\frac{m^3}{mol}\right)$ | 2.57e2 |
| 3 | -10 163 $\left(\frac{m^3}{mol}\right)^3$ | 1.8e-4 |
| 4 | 3 685 $\left(\frac{m^3}{mol}\right)$ | 3.14e6 |

## A.1 Obtained Tunings

In tables below the acquired tunings from optimization are summarized. Starting with the oxidation reactions, R1 and R2 shows a similar trend, where the pre-exponential factor has increased and activtion energy decreased. R3 shows the

opposite, and the decreased rate for this reaction likely reflects the fitting of the leftover slow oxidized hydrocarbons. R4 shows a large decrease in activation energy, reflecting hydrogen combustion being prominent already at lower temperatures.

| Kinetic parameters for R1-R4 | | | | | | | |
|---|---|---|---|---|---|---|---|
| $a_1$ | $e_1$ | $a_2$ | $e_2$ | $a_3$ | $e_3$ | $a_4$ | $e_4$ |
| 3.7566 | 0.8942 | 7.7903 | 0.8140 | 0.1025 | 2.3960 | 0.1001 | 0.4798 |

**Table A.3:** Obtained kinetic parameters for oxidation with $O_2$ reactions tuned using 70mm catalyst experiment

Tunings for NO reductions are a bit more modest, and are closer to the starting values of 1. Most changes are made on R5, which is the reaction where CO reduces NO. A possible explanation for the poor sensitivity on R7 (which is where $H_2$ reduces NO), could be attributed to $H_2$ favouring the path via $O_2$ instead. Even less change is seen for R6, meaning that even less sensitivity was seen for this reaction. This reaction has a higher nominal activation energy, so an explanation might be that the temperature range was too low for this reaction to show any sensitivity. A lower bound was set on this parameter, which for this particular case might have affected the outcome. All changes are attributed to R5, which showed a prominent sensitivity in the selected range.

| Kinetic parameters for R5-R7 | | | | | |
|---|---|---|---|---|---|
| $a_5$ | $e_5$ | $a_6$ | $e_6$ | $a_7$ | $e_7$ |
| 1.0439 | 0.8374 | 1.0001 | 0.9990 | 1.0002 | 0.9987 |

**Table A.4:** Obtained kinetic parameters for reduction of $NO$ reactions tuned using 70mm catalyst experiment

The region chosen for WGS and SR was shown fruitful, as the selected portion showed sensitivity. Generally, both reactions ended up with increased rates to acquire a good fit. R8 had more focus on pre-exponential factor, in contrast to R9 which showed more sensitivity towards a decreased activation energy. The nominal R8 tuning complied better with the temperature, while $e_9$ was more than halfed. Recall the exponential relation to temperature, meaning that this is quite a drastic change.

| Kinetic parameters for R8-R9 | | | |
|---|---|---|---|
| $a_8$ | $e_8$ | $a_9$ | $e_9$ |
| 3.7411 | 0.9678 | 1.9265 | 0.4562 |

**Table A.5:** Obtained kinetic parameters for the water-gas shift and steam reforming reactions tuned using 70mm catalyst experiment

# B

# Additional Model Validations

## B.1 30mm with ±2% $\lambda$-switches 51 g/s

By increasing the space velocity to the highest setting, little to no variation is seen in the conversions. Note that the temperatures span in the upper range, between 600-920K. Similar behaviour to the 34 g/s counterpart can be seen in Fig. B.1.

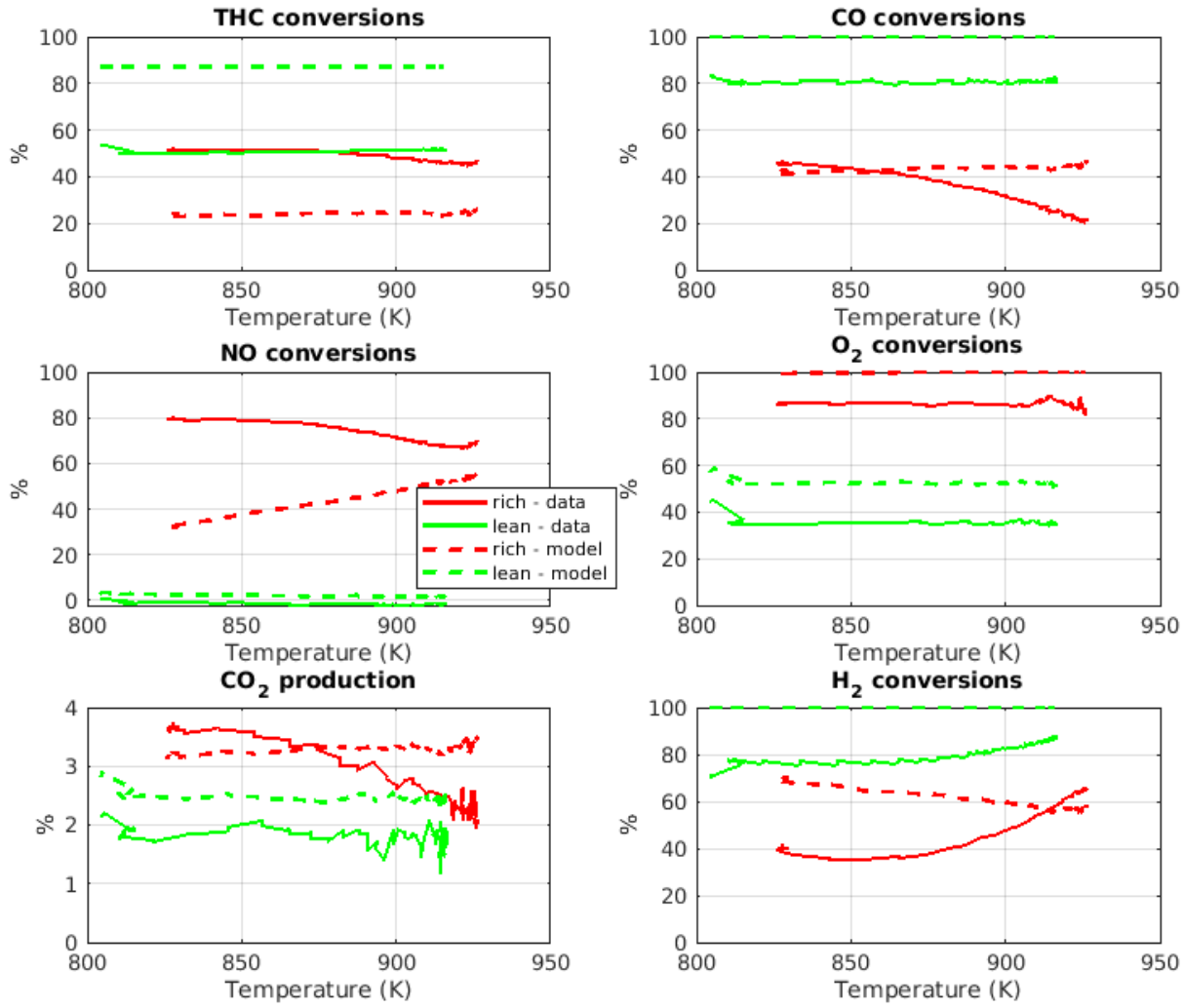


**Figure B.1:** Conversion of species with respect to temperature for the 30mm ± 2% with 51g/s bang-bang experiment

Lean side THC, CO and $H_2$ shows worse conversion, even though temperature is higher. The increased space velocity is not counter-affected with high enough temperatures.

Rich side predictions for THC, CO and NO are similar. So is $H_2$, but the conversion is slightly lower. The WGS equilibrium settling mismatch continues, and the effects are still protruded when experiment is ended at 930K.

## B.2 15mm with ±2% λ-switches

The final case is the 15mm catalyst with ±2% switches. It is once again interesting to think in terms of space velocity. The length is roughly 3 times shorter than the

70mm, meaning that space velocity wise, this experiment is comparable with 70mm with massflow 51 g/s. Conversions are shown in Fig. B.2.

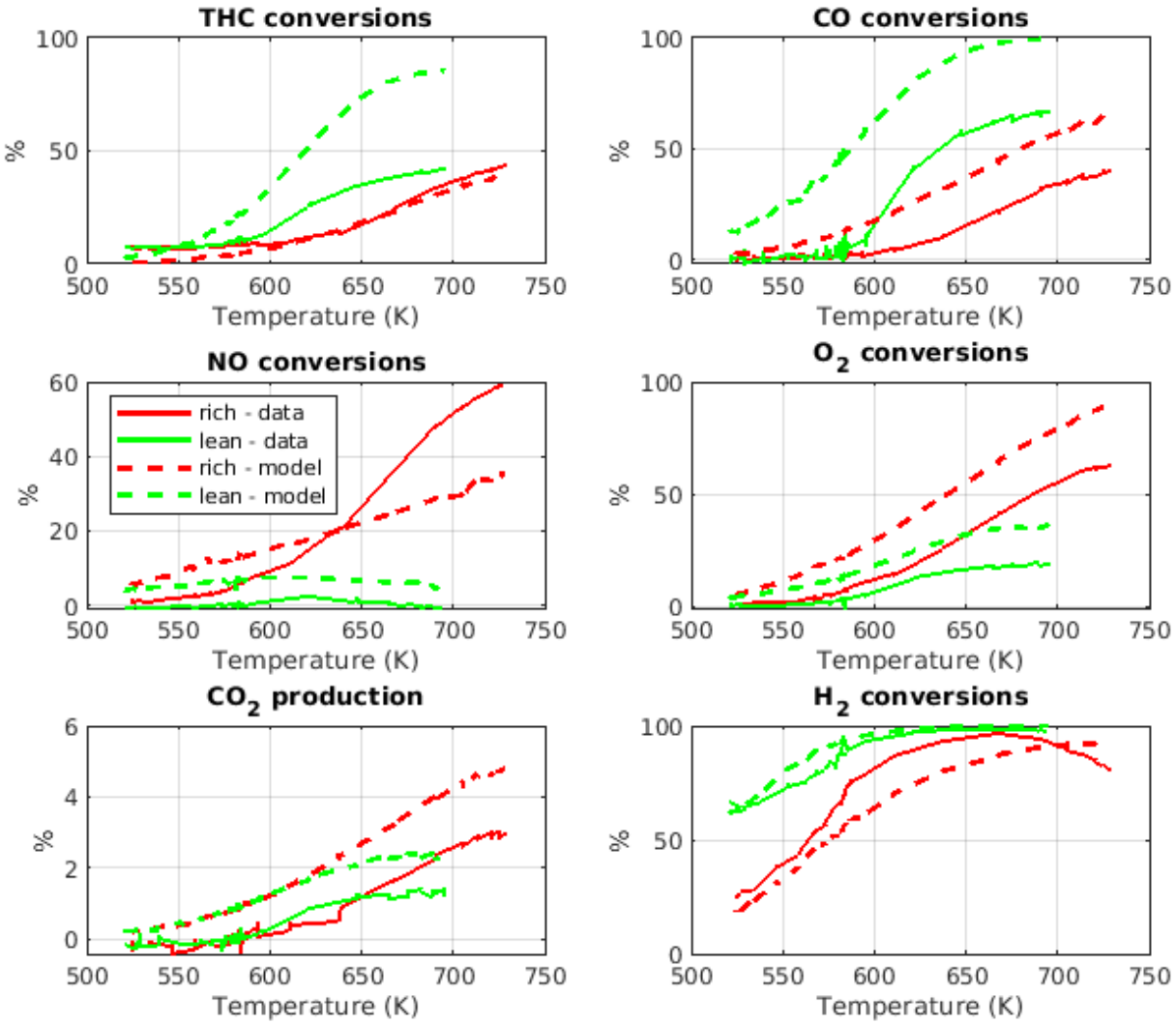


**Figure B.2:** Conversion of species with respect to temperature for the 15mm ± 2% with 17g/s bang-bang experiment

Lean side predictions are not very good (with exceptions on $H_2$), but still accurate light-off shapes can be noted, even though the absolute conversions are slightly over-predicted.

As for the rich side, overpredicted $O_2$ usage translates to an overpredicted CO conversion. NO is showing a linear behaviour, rather than exponential. Studying the reaction rates, these suggest NO conversion is dominated by reduction via CO, most likely due to a high tuning for this reaction. CO shows a modest slope, which might be able to explain the similar shape on the NO conversion.

# C

# 70mm - Constant $\lambda$

### C.0.0.1 $\lambda = 1.2$

Running at $\lambda = 1.2$ with 1500 RPM and 325 mg/str was made with the fan initially set to max. $H_2$ measurements was not taken for this experiment. This is not considered a problem, as the combination of an engine producing low amounts $H_2$ with excess $O_2$ and a relatively long catalyst should be able to clean all $H_2$. The temperature development over the experiment course can be seen in Fig. C.1.

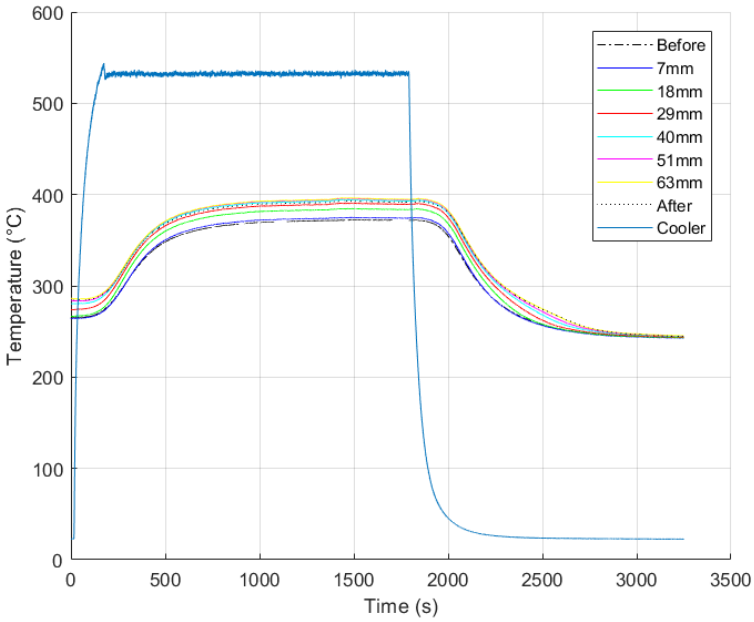


**Figure C.1:** Temperatures at $\lambda = 1.2$, 1500 RPM and 325 mg/str using 70mm catalyst

The first 500s displays a rise as a result of heat from fan and reaction exotherms as the catalyst is lighting off. After settling, the fan is switched to cooling with ambient temperature, to let settle again. It is noted that the heat increase after 40mm is almost negligable. It can hence be concluded that most conversion happen during the first 40mm.

The conversions of CO, THC and NO are displayed in Fig. C.2 as a function of the temperature at 63mm. As expected at a lean setting, CO and THC conversion

are good while NO is poor. This indicates that the NO reduction reactions are overpowered by the $O_2$ oxidation reactions at this setting.

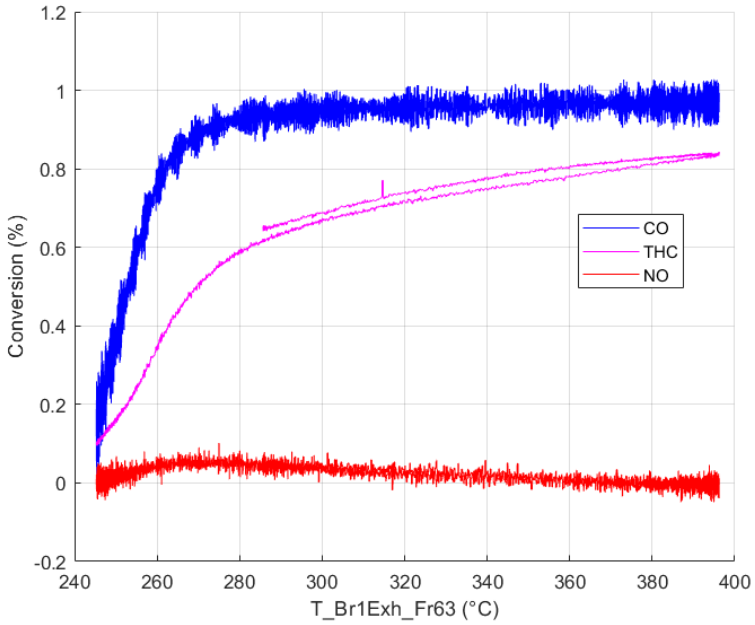


**Figure C.2:** Conversions at $\lambda = 1.2$, 1500 RPM and 325 mg/str using 70mm catalyst

CO conversion is almost 100%. THC is still on the rise, and looks like it is settling at roughly 85%. It could benefit from higher temperatures and/or longer residence time. NO shows some conversion during light-off, but at as the catalyst is getting hotter this conversion declines. No hysteresis is noted.

Emissions of the three main species are illustrated in Fig. C.3. Note the abrupt decrease at 2500s.

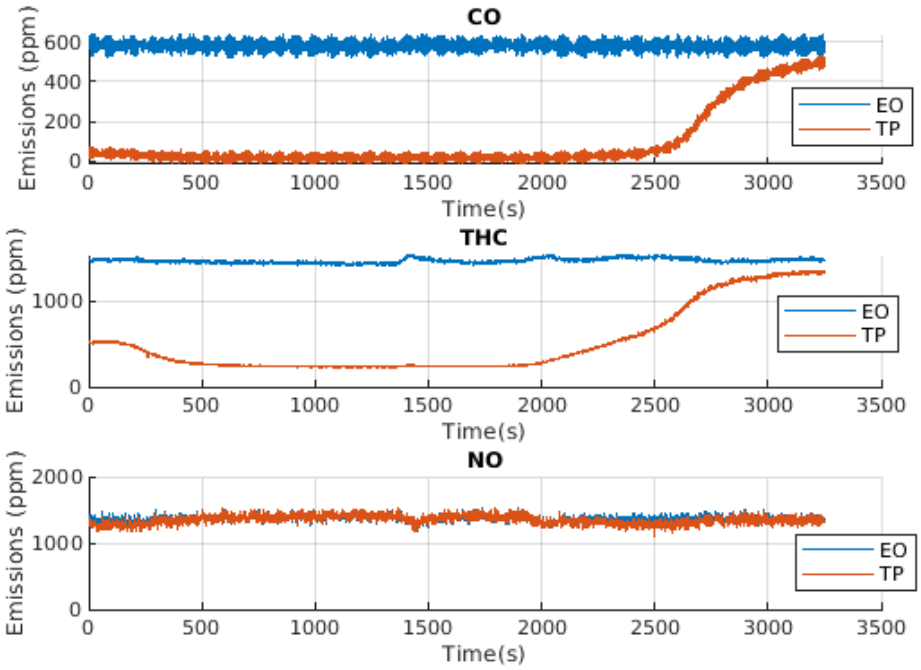


**Figure C.3:** Emissions at $\lambda = 1.2$, 1500 RPM and 325 mg/str using 70mm catalyst

At this point, fan-cooling becomes prominent. When starting measurements at 280°C, very good conversion could be noted, especially for CO. At the end, 240°C has been reached. This is only a difference of 40°C, yet all conversion has been halted. This clearly displays the exponential relation between reaction rates and temperature.

#### C.0.0.2 $\lambda = 1.0$

For this test, the operating point was set to 1450 RPM. Load was for two thirds set to 390 mg/str, later being switched to 325 mg/str. See Fig. C.4. $H_2$ was not measured.

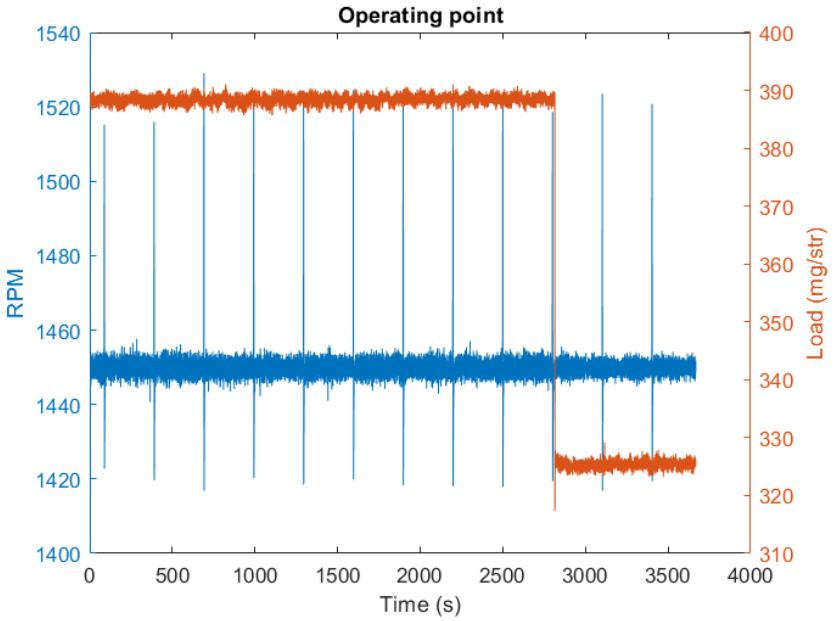


**Figure C.4:** Operating point at $\lambda = 1.0$, 1500 RPM and 390/325 mg/str using 70mm catalyst

The reason for this step change was to study the effects of an decreased temperature slope, as decreasing load affects the amount of air intake to the cylinders. Less air means worse conversion and hence lower temperatures. The temperature profiles are displayed in Fig. C.5.

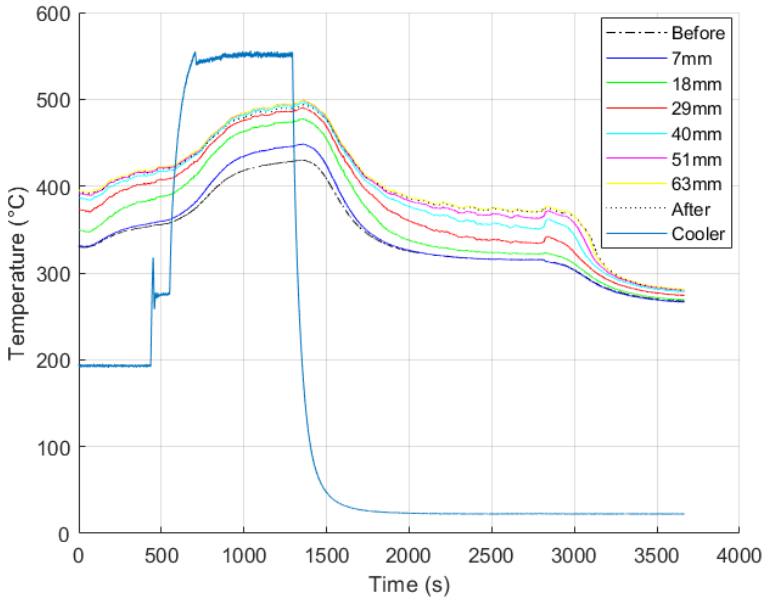


**Figure C.5:** Temperatures at $\lambda = 1.0$, 1450 RPM and 390/325 mg/str using 70mm catalyst

Initially, the fan is set to 200°C, increased to max at roughly 600s. The temperatures

settles, and the fan is set to cool using ambient temperature air. After settling, the load step is initiated followed by a final settling period. Note that similar to $\lambda = 1.2$, most conversion occurs the first 29mm. The higher temperatures for this $\lambda$ is mostly attributed to the higher load, which provides $O_2$ for CO and THC combustion. Theoretically, this operating point should give the best conversion for all species, see Fig. C.6.

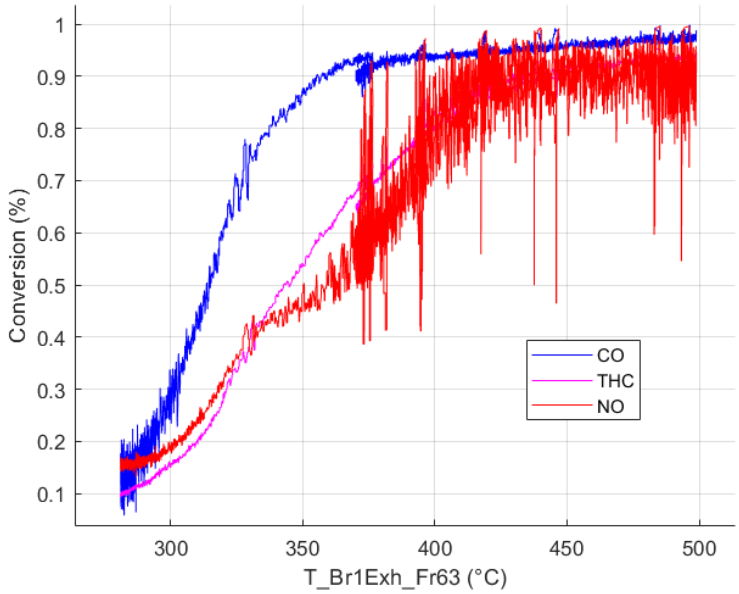


**Figure C.6:** Conversions at $\lambda = 1.0$, 1500 RPM and 390/325 mg/str using 70mm catalyst

No hysteresis can be observed. Indeed high conversion can be noted for all species. It can be seen that CO is yet to settle, but not quite reaches 100%. Looking at the available $O_2$ in Fig. C.7, it can be seen that $O_2$ is completely depleted. An explanation is that NO can still be used to reduce both CO or THC. This indicates that reduction via NO is not as potent as combustion via $O_2$.

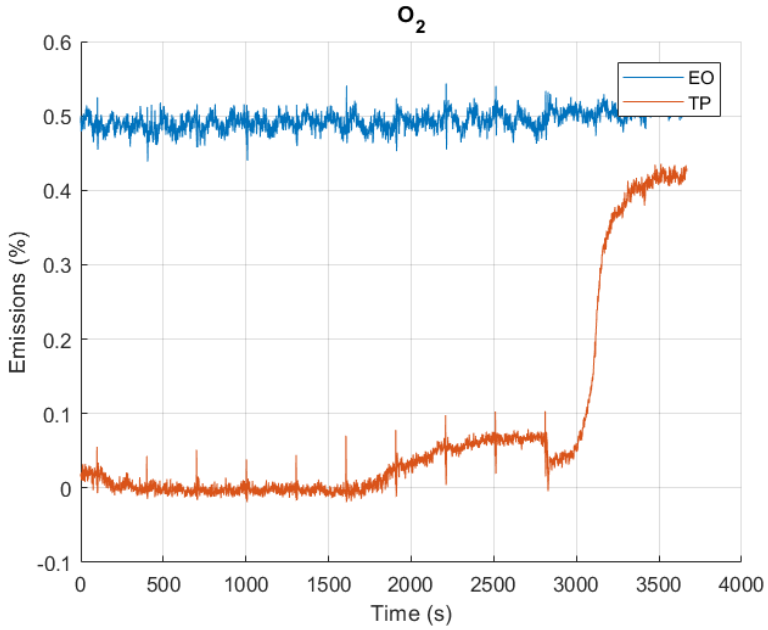


**Figure C.7:** $O_2$ pre- and post catalyst at $\lambda = 1.0$, 1500 RPM and 390/325 mg/str using 70mm catalyst

#### C.0.0.3 $\lambda = 0.9$

For this setting, 1500 RPM and 325 mg/str is used. Measurements are taken directly after a 150 mg/str to 325 mg/str load step, which explains the initial transient behaviour in some of the graphs. The catalyst is initially cold at roughly 150°C, and it can be seen in Fig. C.8 that all temperatures coincide.

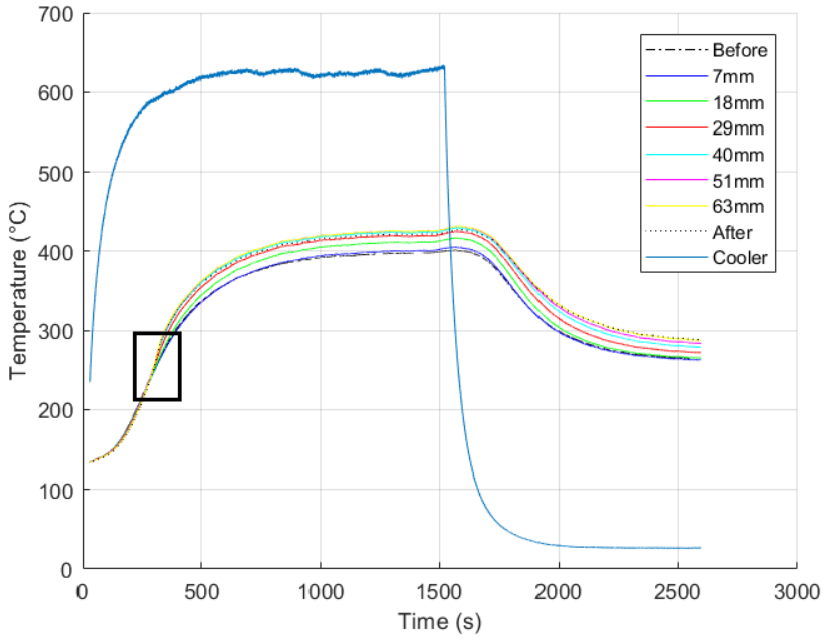


**Figure C.8:** Temperatures at $\lambda = 0.9$, 1500 RPM and 325 mg/str using 70mm catalyst

Note the area marked with a black rectangle. This region is displayed in higher resolution in Fig. C.9.

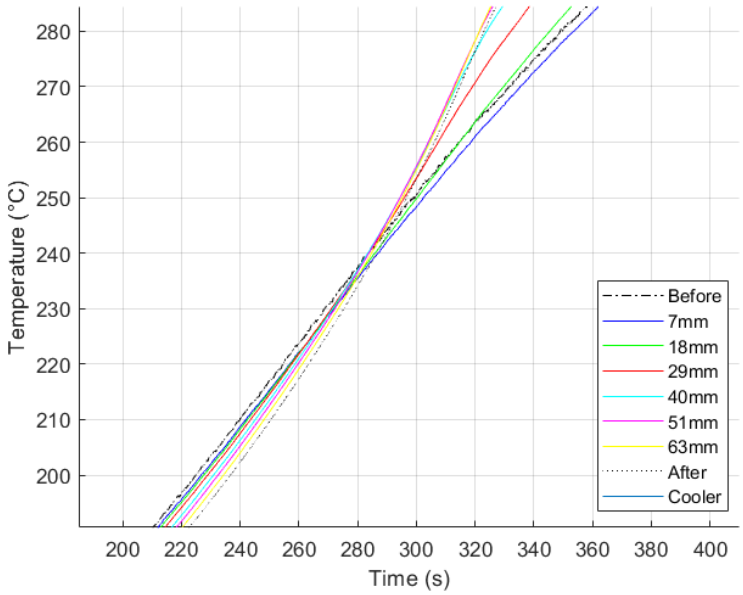


**Figure C.9:** Light-off region at $\lambda = 0.9$, 1500 RPM and 325 mg/str using 70mm catalyst

The yellow curve, which is the rear temperature, is located below the blue curve displaying front temperature. As the catalyst lights off, it does this from the rear

which is illustrated by the yellow curve showing a higher slope than the blue curve at light-off.

Conversions indicate a distinct hysteresis as shown in Fig. C.10. As the fan is set to cool, conversions start to decay, but follows a different path when compared to the temperature upslope.

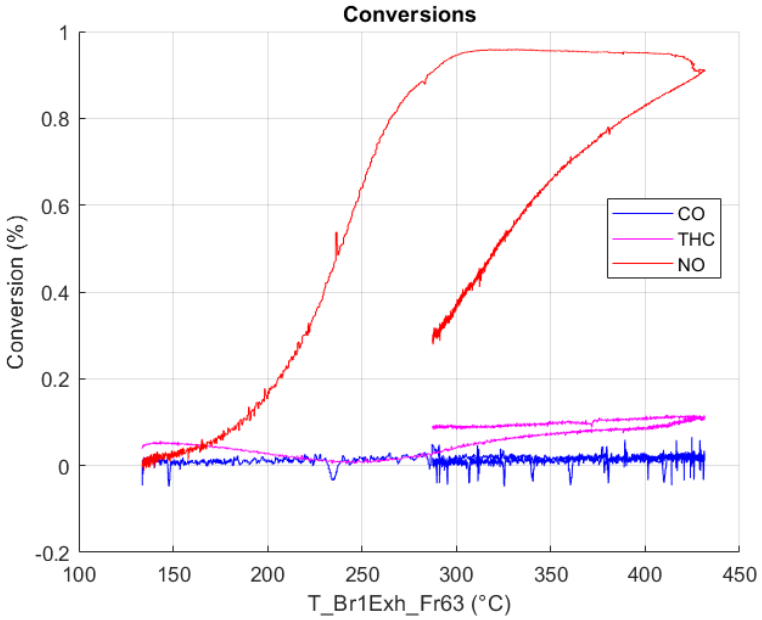


**Figure C.10:** Conversions at $\lambda = 0.9$, 1500 RPM and 325 mg/str using 70mm catalyst

This indicates a potential poisoning effect. The observant eye can note that the NO conversion exhibits a weak declining slope even though temperatures increase. It does not reach 100%, even though reducing species such as CO and THC exist in abundance, as can be seen in Fig. C.11.

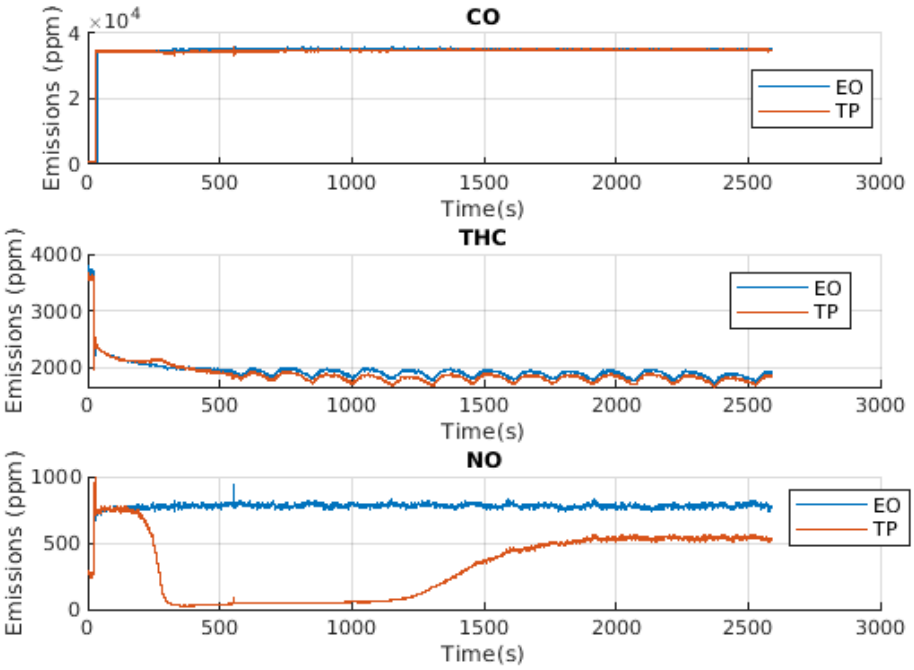


**Figure C.11:** Emissions pre- and post catalyst at $\lambda = 0.9$, 1500 RPM and 325 mg/str using 70mm catalyst

A conclusion here is that using this data for optimization is not appropriate, as the model does not take this phenomena into account.

Another feature of this experiments was that $H_2$ measurements were taken, see Fig. C.12. These show some slight disturbance peaks at 1000s and 2600s, but the general trends can be followed. When the fan is set to cool, the conversion decreases.

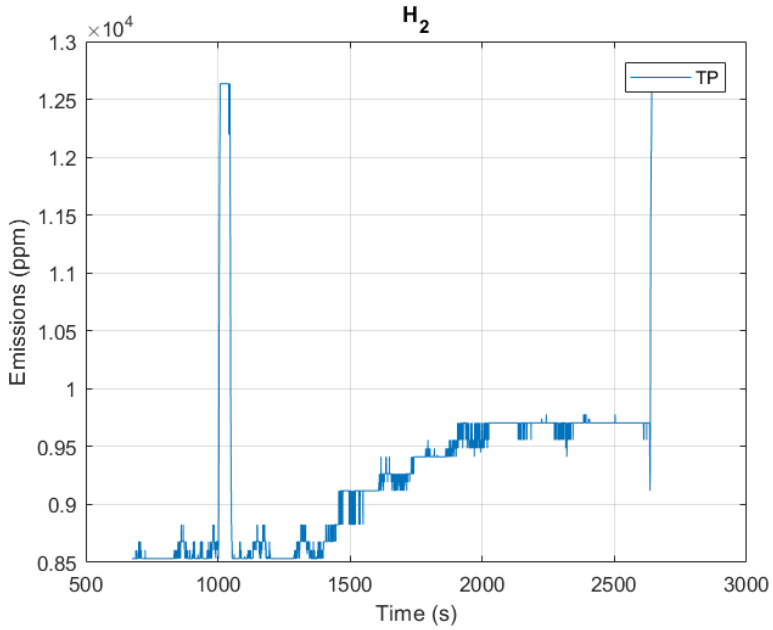


**Figure C.12:** $H_2$ tailpipe emissions at $\lambda = 0.9$, 1500 RPM and 325 mg/str using 70mm catalyst

$H_2$ is converted either by NO reduction or $O_2$ oxidation, see Fig. C.13.

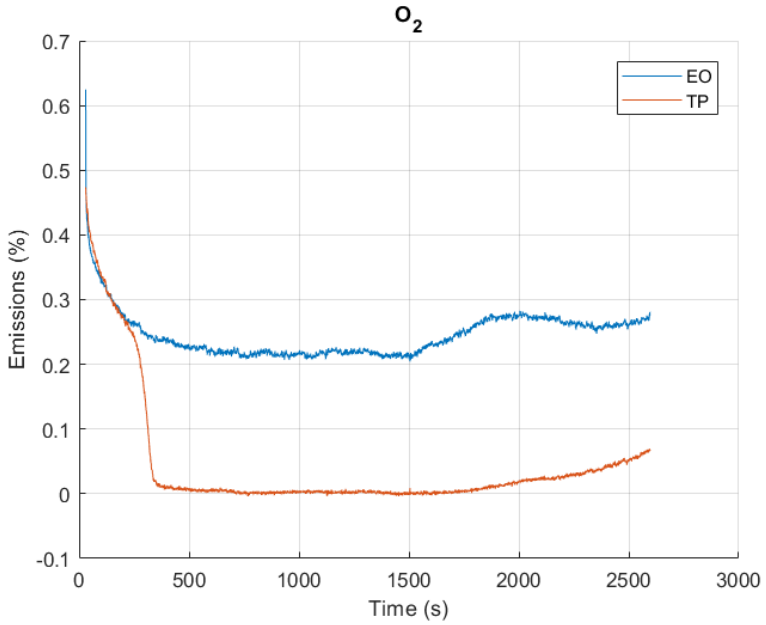


**Figure C.13:** $O_2$ pre- and post catalyst at $\lambda = 0.9$, 1500 RPM and 325 mg/str using 70mm catalyst

$O_2$ being completely depleted in combination with the poisoning effect makes it impossible to convert all $H_2$, leaving a 1% slip post catalyst.

# D

# 30mm - Constant $\lambda$

#### D.0.0.1 $\lambda = 1.1$

For this catalyst length, the previous choice of $\lambda = 1.2$ was revised, in favour of $\lambda = 1.1$. $H_2$ measurements were taken, but show nothing of interest as everything is depleted post-catalyst. The routine was slightly changed in contrast to 70mm experiments, as a result of a learn-by-doing process. Load is constantly set to 325 mg/str, while the engine speed is revved up in intervals, as shown in Fig. D.1.

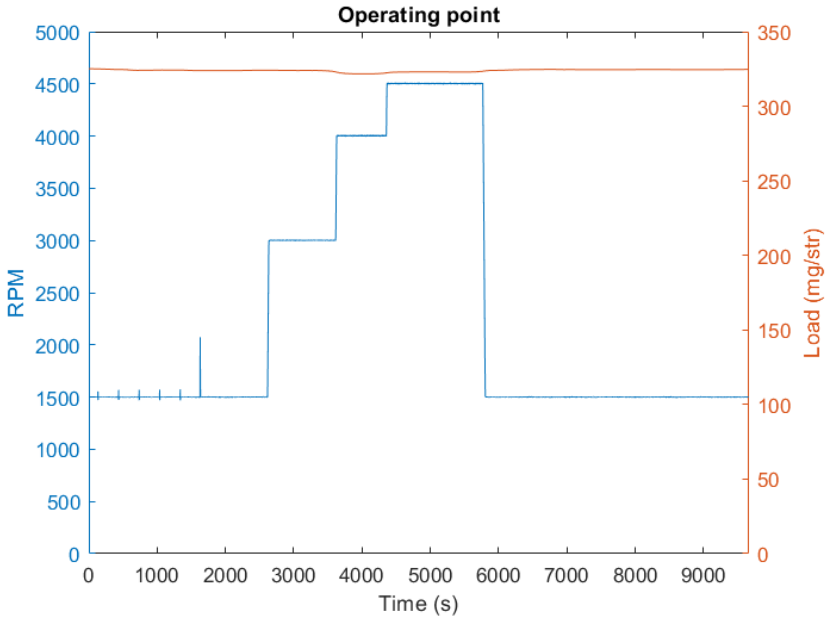


**Figure D.1:** Operating point at $\lambda = 1.1$ using 30mm catalyst

Temperatures were allowed to settle in between these changes, as displayed in Fig. D.2. Peak temperatures are above 600°C, and is a result of the high engine speed of 4500 RPM.

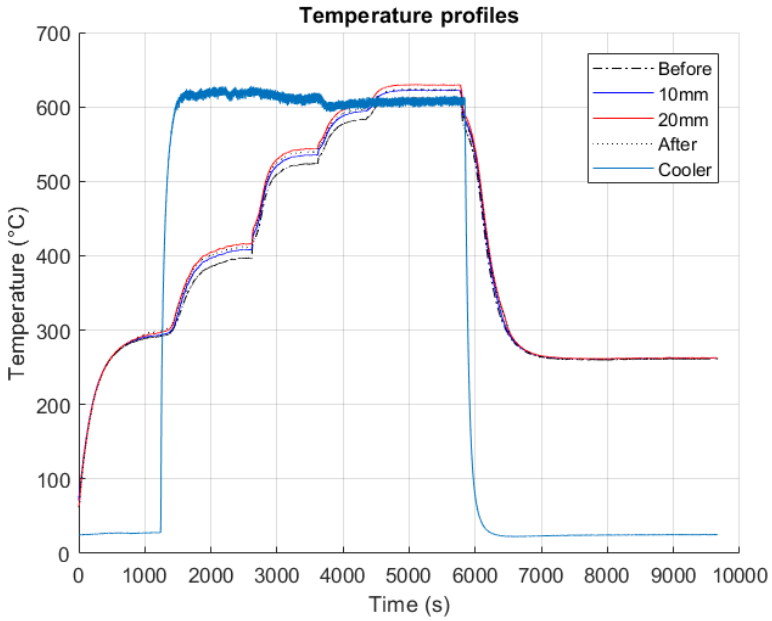


**Figure D.2:** Temperatures at $\lambda = 1.1$ using 30mm catalyst

These high temperatures are important to reach high conversion when the catalyst is relatively shorter, see Fig. D.3. But even though higher speeds give higher temperatures, the residence time decrease overpowers this increase. Also, hysteresis is not shown.

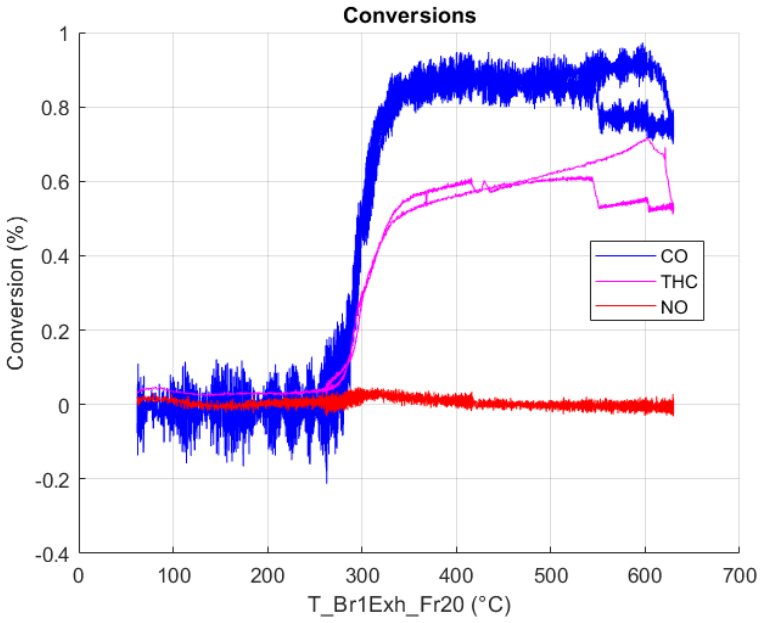


**Figure D.3:** Conversions at $\lambda = 1.1$ using 30mm catalyst

#### D.0.0.2 $\lambda = 1.0$

Stochiometric $\lambda$ was operated with a load at 325 mg/str. A noisy pulse can be observed at 2000s. Engine speed was revved up in two steps from 1500 RPM to 3000 RPM, via 1550RPM for a shorter time, see Fig. D.4.

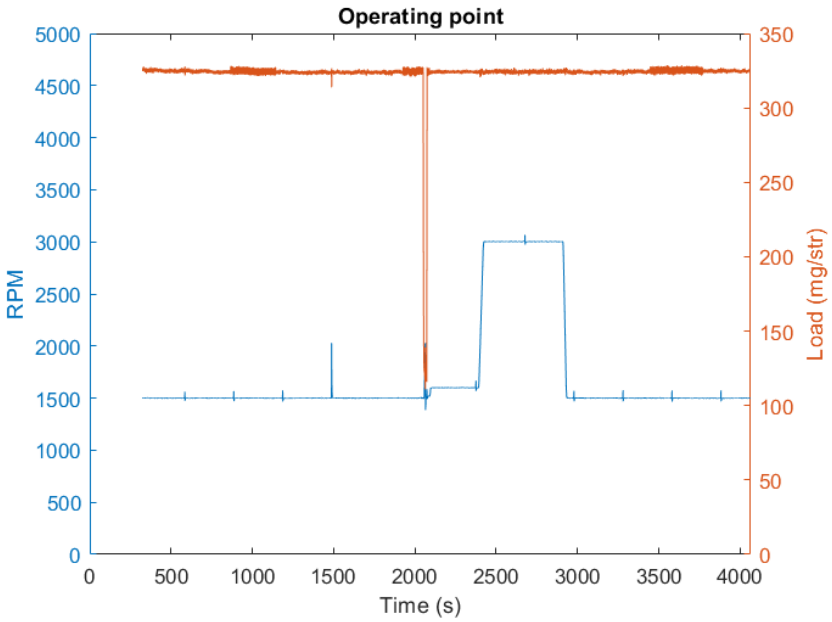


**Figure D.4:** Operating point at $\lambda = 1.0$ using 30mm catalyst

Temperature profiles are displayed in Fig. D.5. The temperatures does not quite settle at 3000 RPM. Decreasing to 1500 RPM and fan cooling is synchronized.

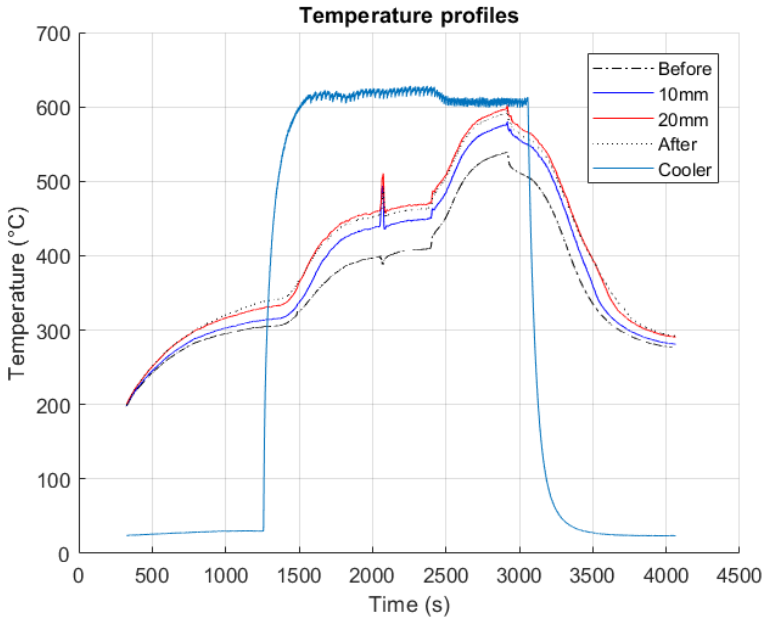


**Figure D.5:** Temperatures at $\lambda = 1.0$ using 30mm catalyst

The load noise dislays a peak, which explains the conversion jump seen in Fig. D.6. All species show conversion, further illustrating the trade-off between higher temperature and decreased residence time. All species would clearly benefit from a longer catalyst, especially NO.

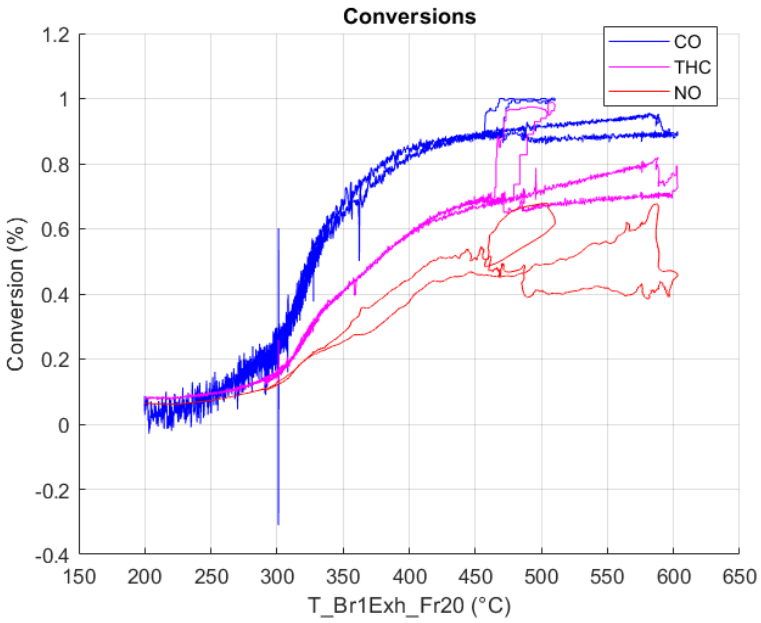


**Figure D.6:** Conversions at $\lambda = 1.0$ using 30mm catalyst

Emissions data show that $O_2$ is still available for reaction, see Fig. D.7. Note that full depletion occurs at 3000s. This is the section when the catalyst has reached its peak temperature, followed by an engine speed step to 1500 RPM. At this instant, the increase in residence time in combination with the high temperature memory displays good $O_2$ usage.

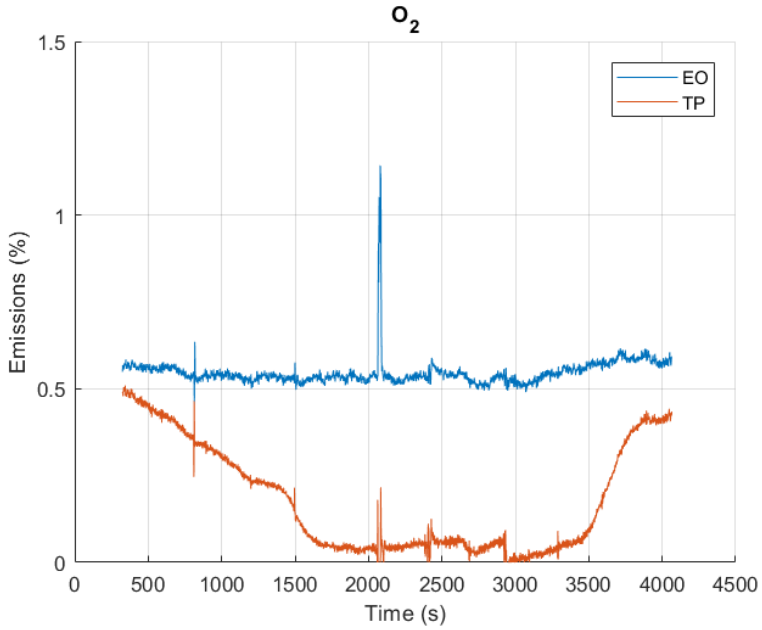


**Figure D.7:** $O_2$ emissions at $\lambda = 1.0$ using 30mm catalyst

The decrease in NO conversion in comparison to 70mm can be attributed to the decrease in residence time. NO reduction reactions clearly influence the conversion. These are probably slower than the combustion reactions, and a longer residence times hence benefit those reaction paths as $O_2$ has depleted.

#### D.0.0.3 $\lambda = 0.98$

Poisoning effects were studied further by trying a $\lambda$ closer to stochiometry. Choice of operating point was identical to the $\lambda = 0.9$ counterpart, as shown in the main document. The temperature profiles are displayed in Fig. D.8. Temperature reach a higher level in comparison, as better conversion is obtained when closer to stochiometry.

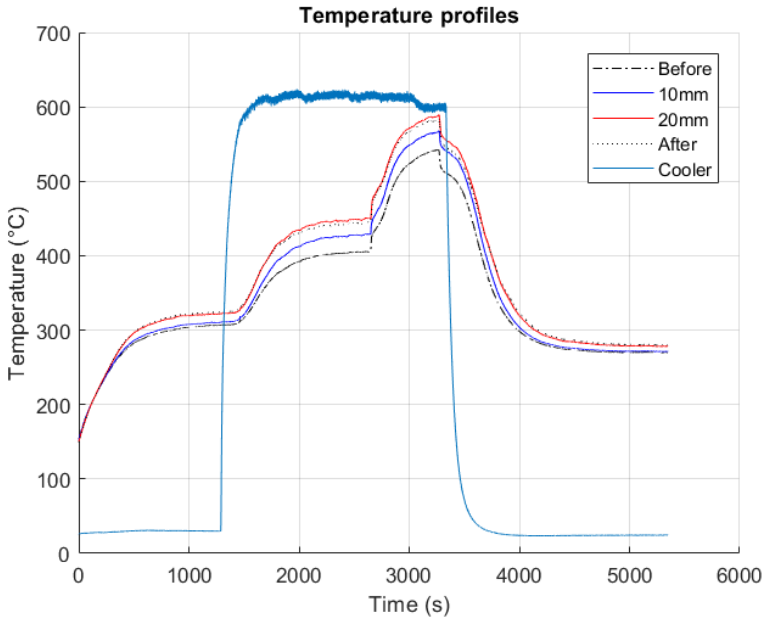


**Figure D.8:** Temperatures at $\lambda = 0.98$ using 30mm catalyst

As expected, NO shows best conversion, see Fig. D.9. Note that NO exhibits a conversion decrease twice, once pre CO and THC light-off and once post CO and THC light-off. The first instance is likely attributed to CO and THC light-off, rather taking the path via $O_2$ rather than NO. The second conversion decrease can be observed for all three species simultaneously, and is a result of poisoning. It is most prominent for CO.

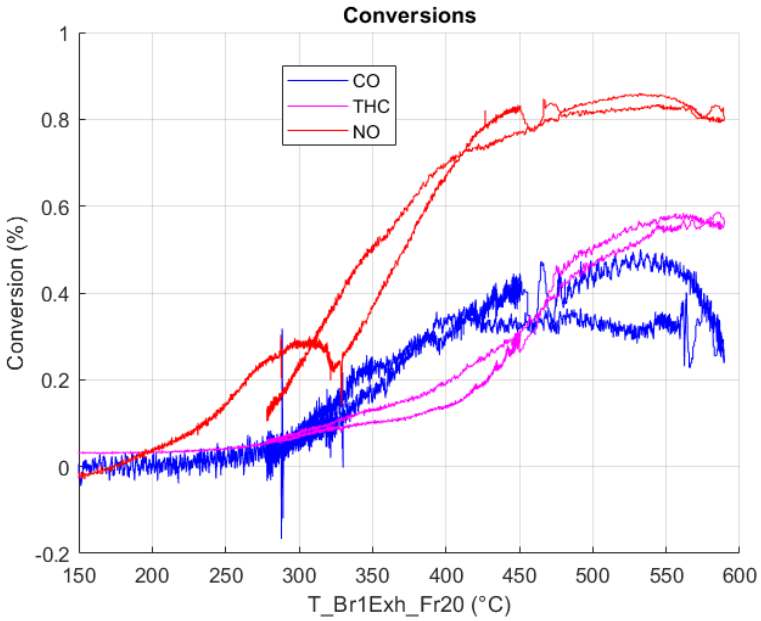


**Figure D.9:** Conversions at $\lambda = 0.98$ using 30mm catalyst

$H_2$ emissions are shown in Fig. D.10. Note the section between 2600s and 3800s.

Engine revving up to 3000 RPM gives an increase which is parried by an increased temperature. The next peak can be attributed to revving down to 1500 RPM. Conversion increases significantly to later decay as a result of decreasing temperatures.

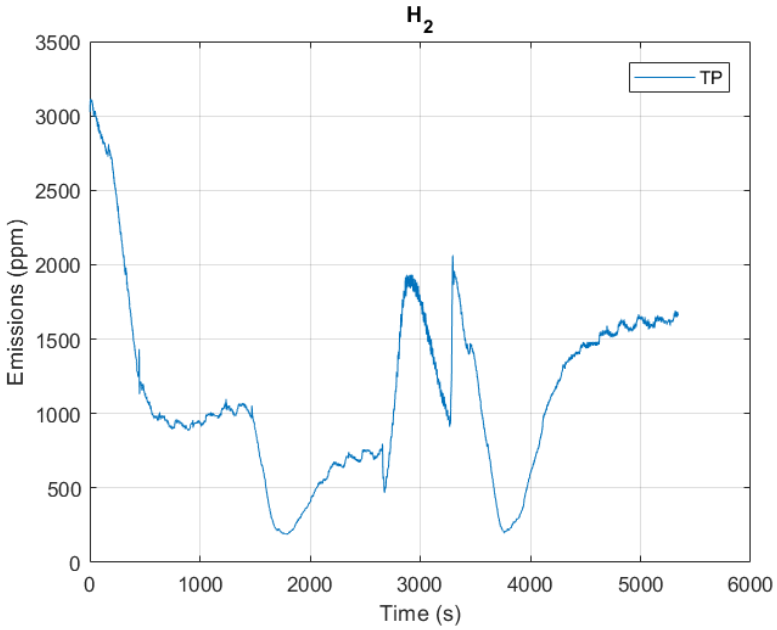


**Figure D.10:** $H_2$ emissions at $\lambda = 0.98$ using 30mm catalyst

Additional tests including particle counting and lean pulsing was also executed at this $\lambda$ to further verify the origin of the poisoning. By advancing the ignition angle more soot particles from the engine could be acquired. Dual lean pulsing of 5s was made, one for normal and advanced ignition angle respectively. Identical recovery and re-poisoning was observed for both cases. This points to the coking effect being a phenomena occuring in the catalyst, rather than being a function of the engine operating point.

# E

# 15mm - Constant $\lambda$

#### E.0.0.1 $\lambda = 1.1$

All temperature sweep experiments with 15mm catalyst include,

1. Let the temperature after light off to settle
2. Heat-exchanger is used to heat the exhaust to the maximum
3. Switched to a higher speed and let it settle
4. Switched back to the lower speed and maximum cooling with the heat-exchanger either simultaneously or in steps.

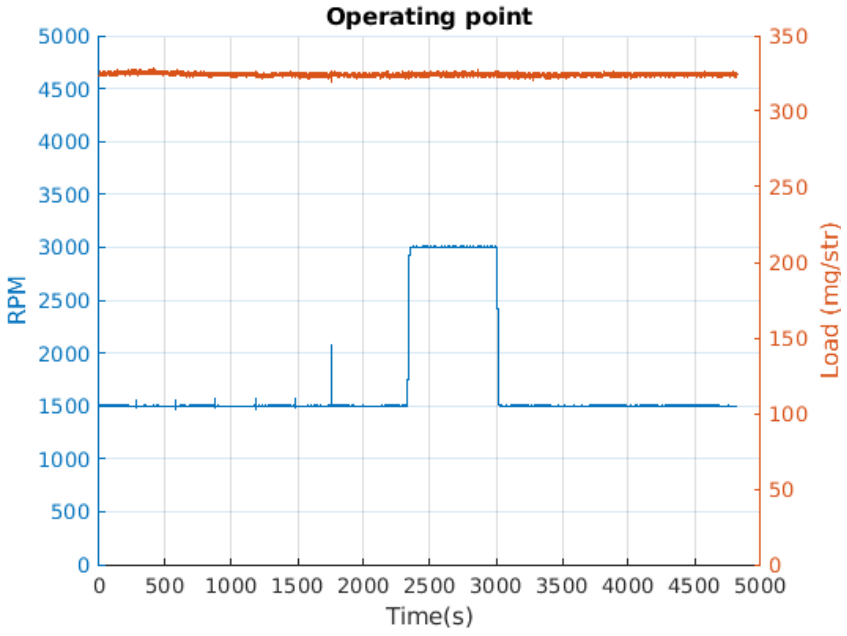


**Figure E.1:** Operating point at $\lambda = 1.1$ using 15mm catalyst

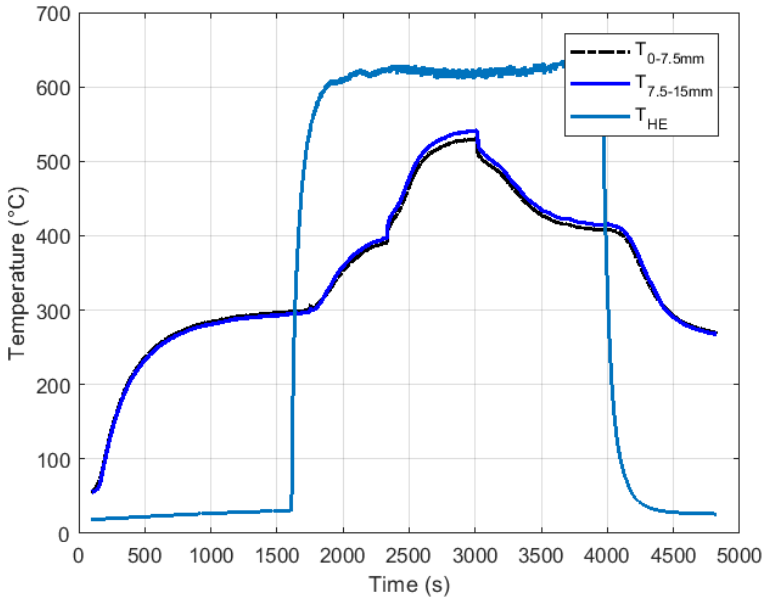


**Figure E.2:** Temperatures at $\lambda = 1.1$ using 15mm catalyst

As seen in fig. E.2, there is good temperature range from before light off (100 degrees) to a maximum temperature of 550 degrees.

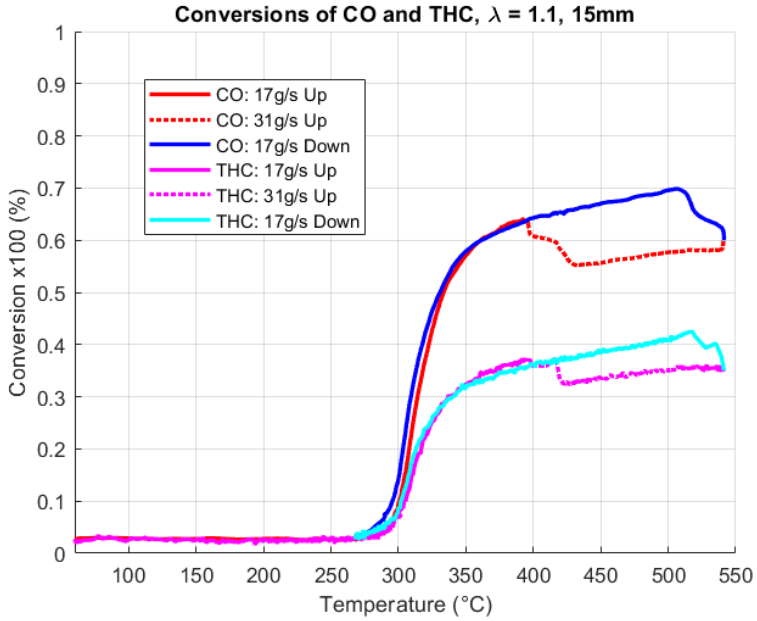


**Figure E.3:** Conversions at $\lambda = 1.1$ using 15mm catalyst

From conversion plot in fig. E.3 that there is no hysteresis between the heat up and cool down phases. The conversion rates of CO and THC can be seen to saturate at about 500 degrees which could be an indication of the mass transfer limitation. (Rates being limited by the small residence times)

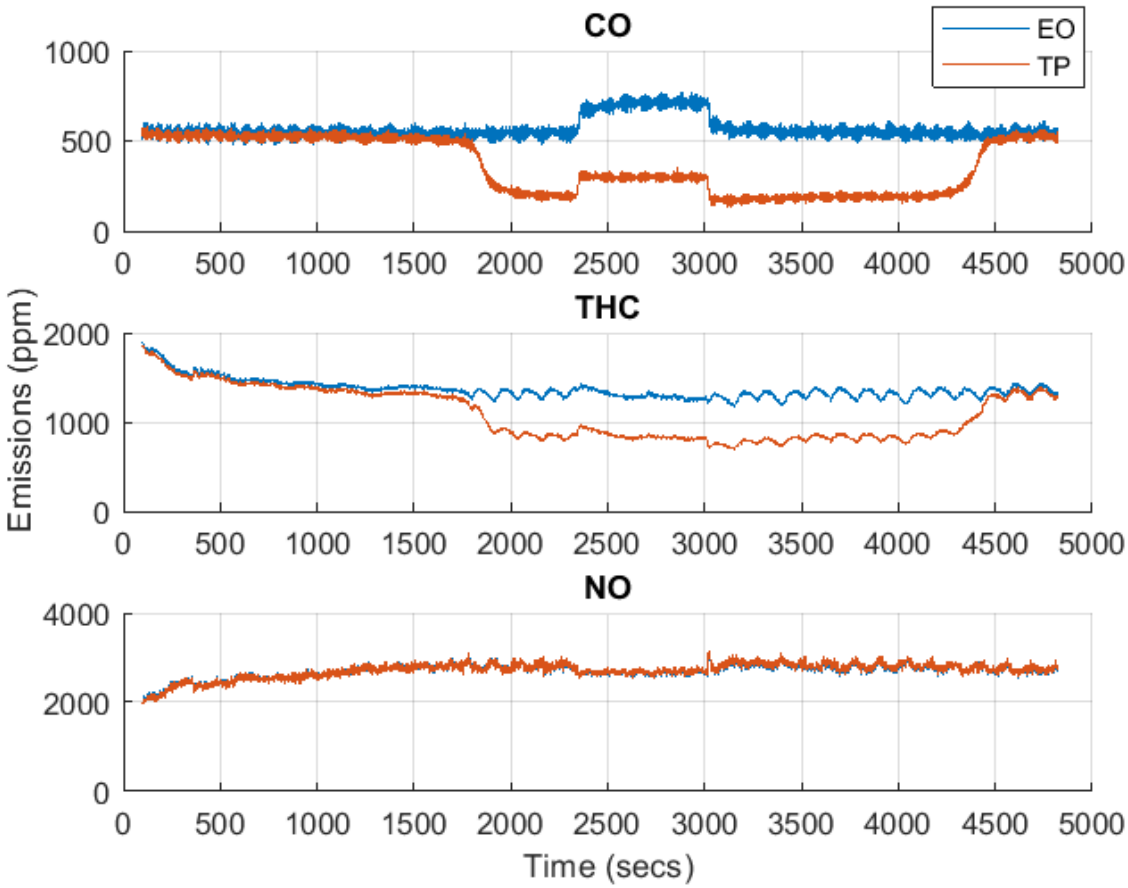


**Figure E.4:** Emissions pre- and post catalyst at $\lambda = 1.1$ using 15mm catalyst

Due to the abundance of $O_2$ concentrations, there is very limited reduction of $NO_x$ on the lean regions. We can also assume buffer to be full and ceria related reactions to be small. Thus making these experiments to be a good validation dataset on the oxidation by $O_2$ reactions.

#### E.0.0.2 $\lambda = 1.02$

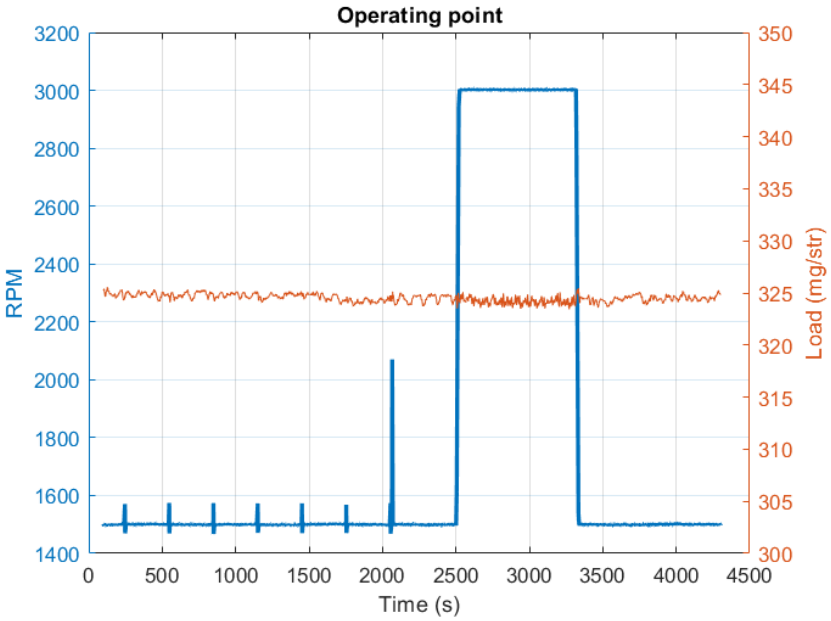


**Figure E.5:** Operating point at $\lambda = 1.02$ using 15mm catalyst

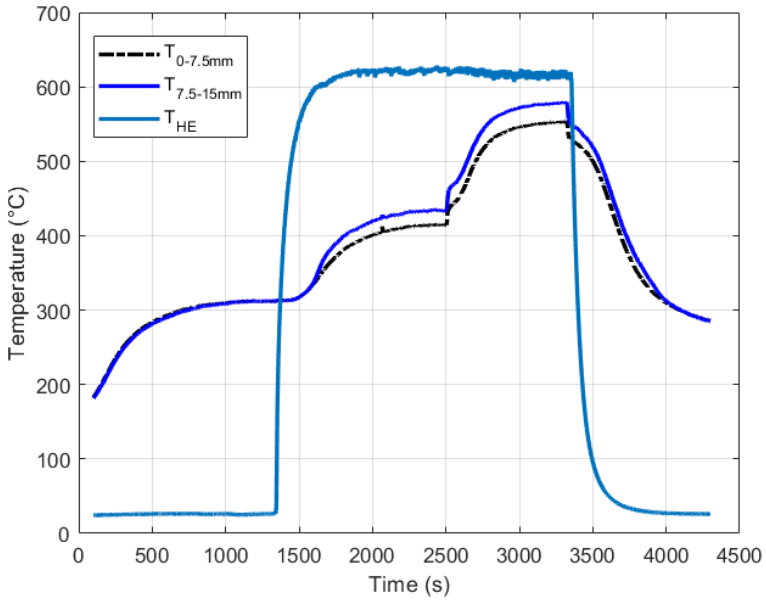


**Figure E.6:** Temperatures at $\lambda = 1.02$ using 15mm catalyst

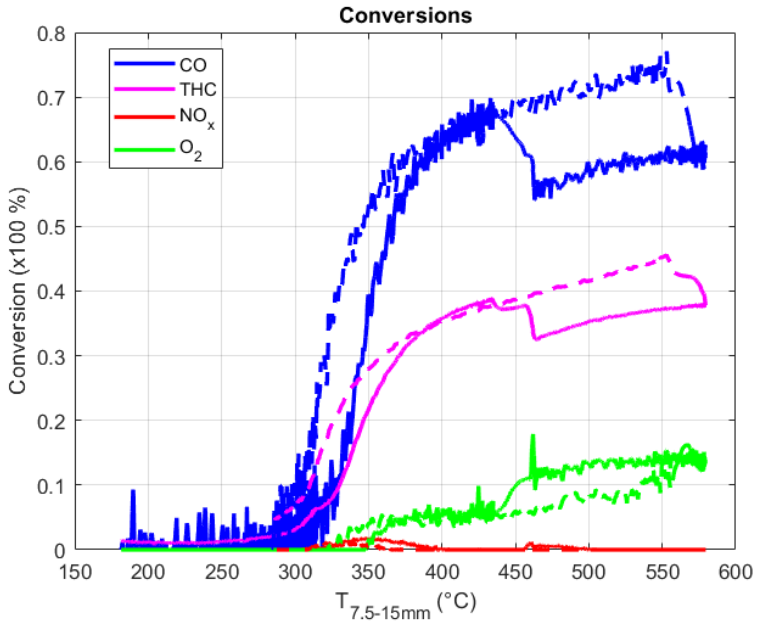


**Figure E.7:** Conversions at $\lambda = 1.02$ using 15mm catalyst

It is observed from Fig. E.7 that there are better conversion rates on the cool down phase. The reason for this hysteresis could be the fact that the cool down is initiated by switching back to 1500 rpm and cooling with the heat exchanger simultaneously.

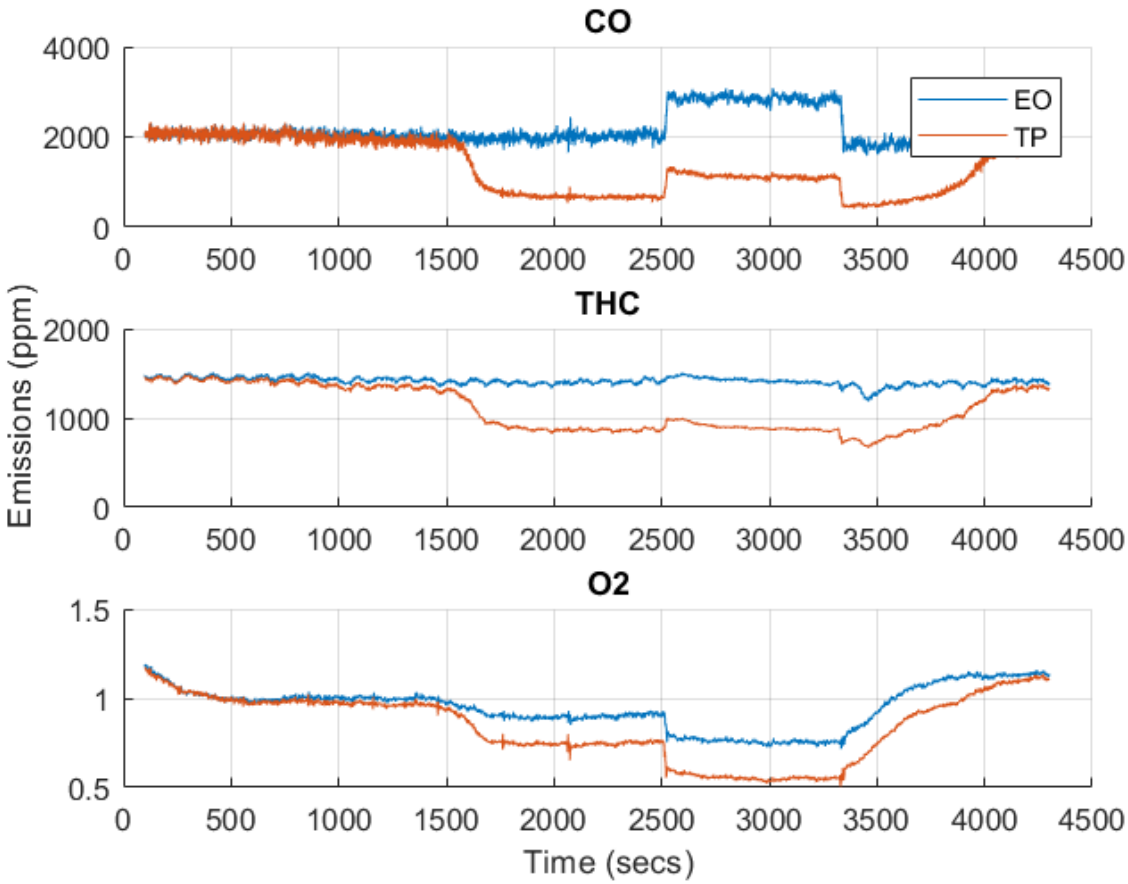


**Figure E.8:** Emissions pre- and post catalyst at $\lambda = 1.02$ using 15mm catalyst

#### E.0.0.3 $\lambda = 1.00$

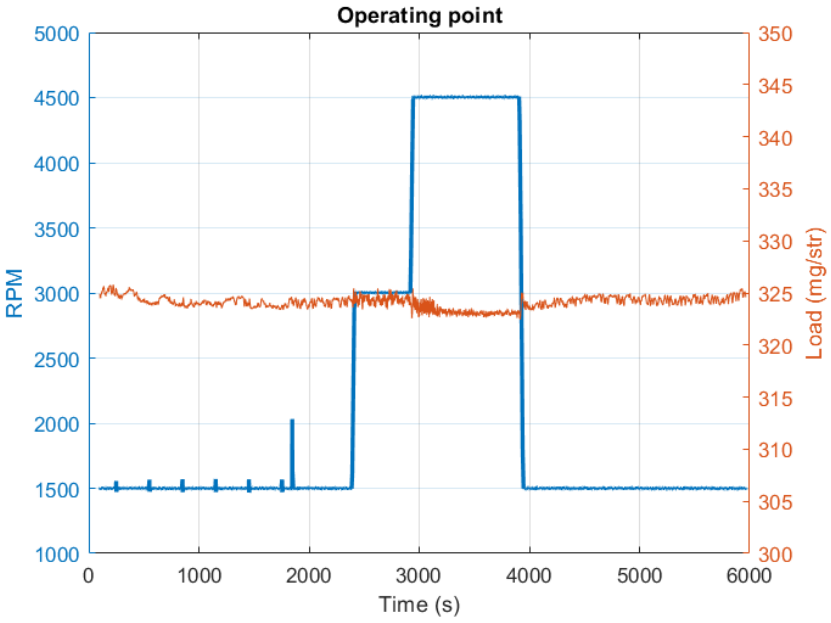


**Figure E.9:** Operating point at $\lambda = 1.00$ using 15mm catalyst

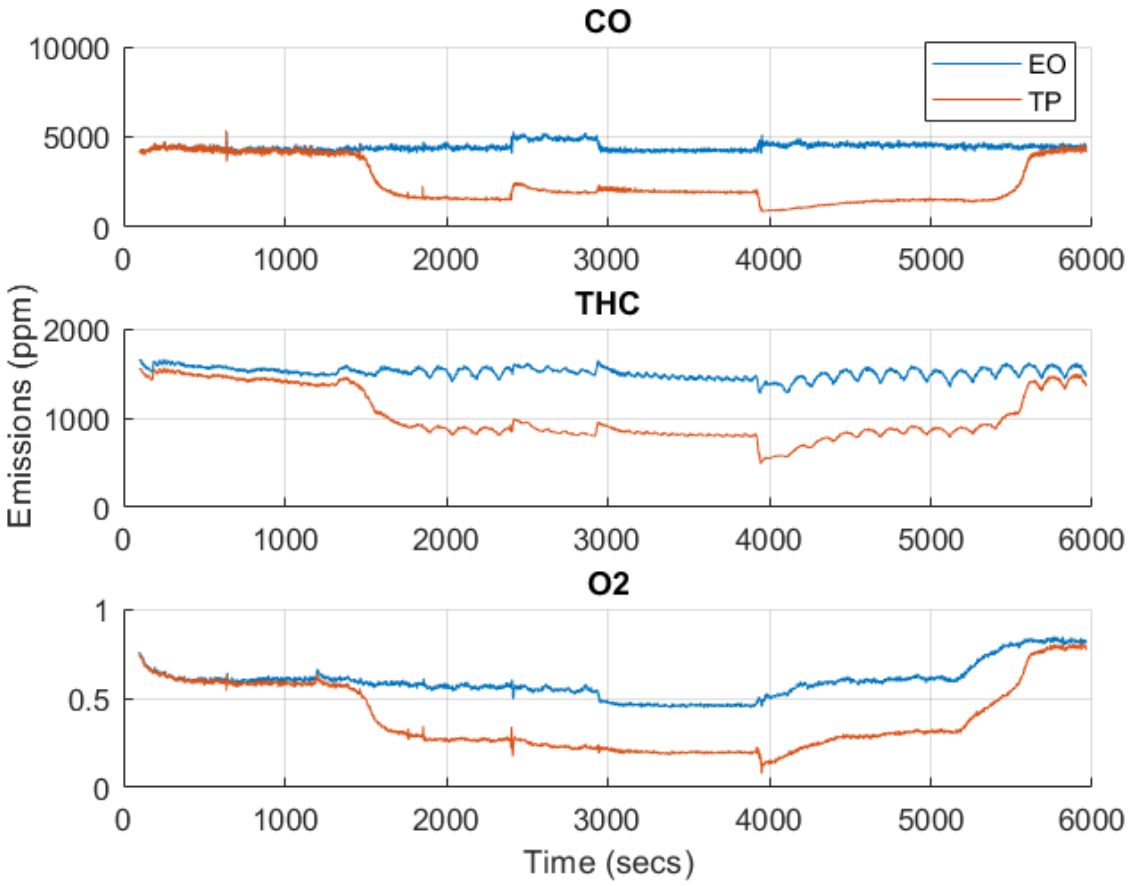


**Figure E.10:** Emissions pre- and post catalyst at $\lambda = 1.00$ using 15mm catalyst

#### E.0.0.4 $\lambda = 0.98$

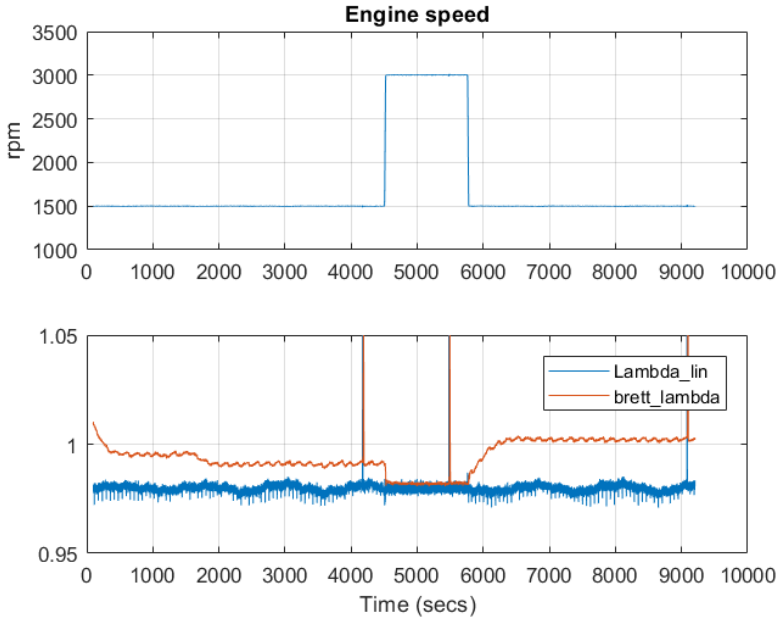


**Figure E.11:** Operating point at $\lambda = 0.98$ using 15mm catalyst

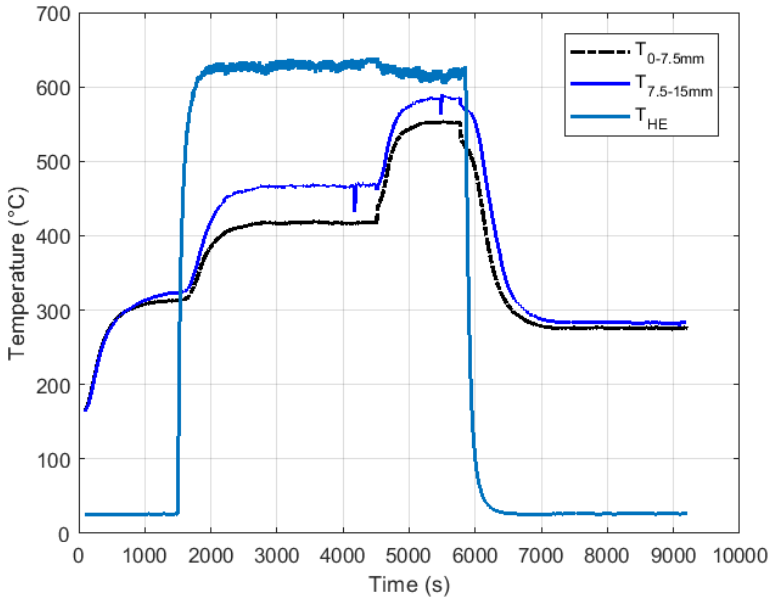


**Figure E.12:** Temperatures at $\lambda = 0.98$ using 15mm catalyst

The air temperature through the heat exchanger is switched to 620 degrees and switched back to 25 degrees at 1500 and 5800 seconds respectively as shown in Fig. E.12. The engine speed was switched to 3000 rpm and back to 1500 rpm at 4500 and 5700 seconds respectively as shown in Fig. E.11.

At all these time instances mentioned above, the $O_2$ concentrations in the engine-out seem to be affected as observed in Fig. E.13. This could be due to a leakage of air into the heat exchanger which is reduced by the increase in pressure caused by increase in temperature or the mass flow (engine speed). Additionally, the Brettschneider lambda shows that we only achieve $\lambda = 0.98$ at the 3000 rpm.

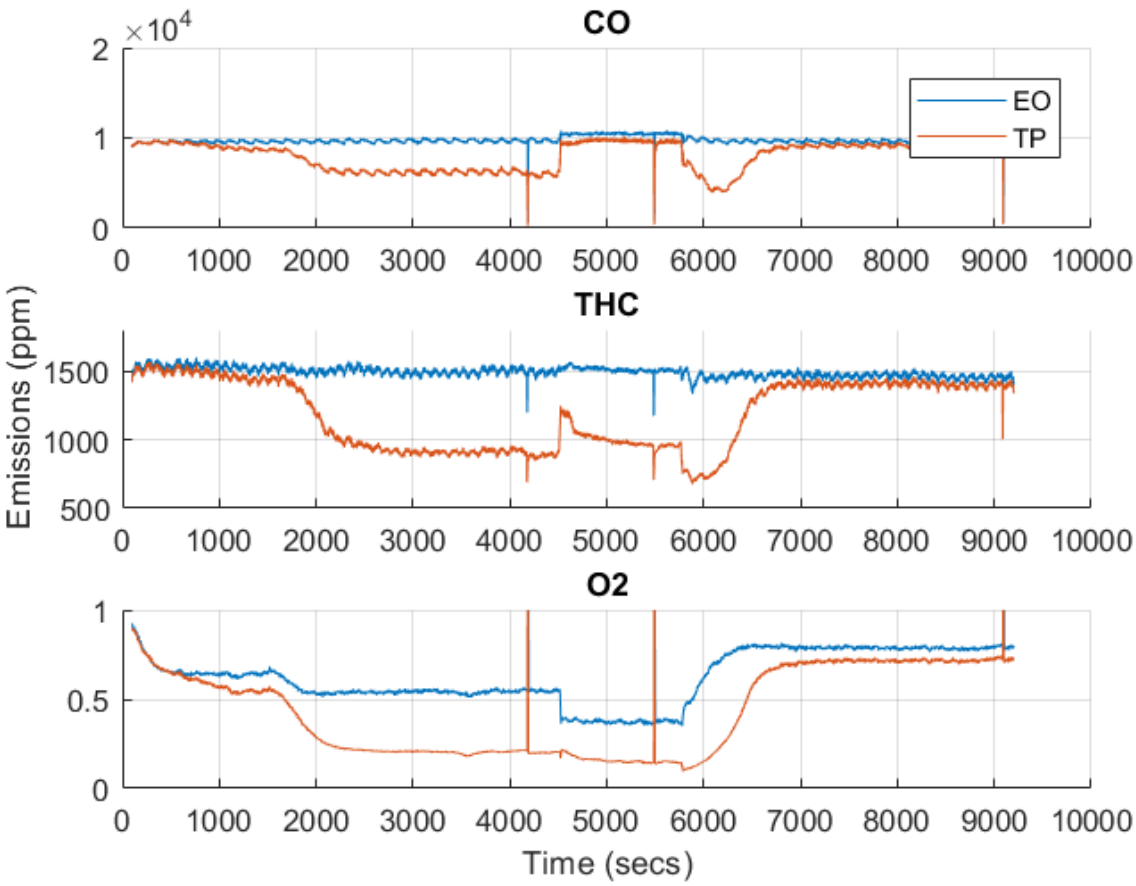


**Figure E.13:** Emissions pre- and post catalyst at $\lambda = 0.98$ using 15mm catalyst

This abnormal behaviour does not affect the model since it uses the engine-out emissions for simulation.

#### E.0.0.5 $\lambda = 0.90$

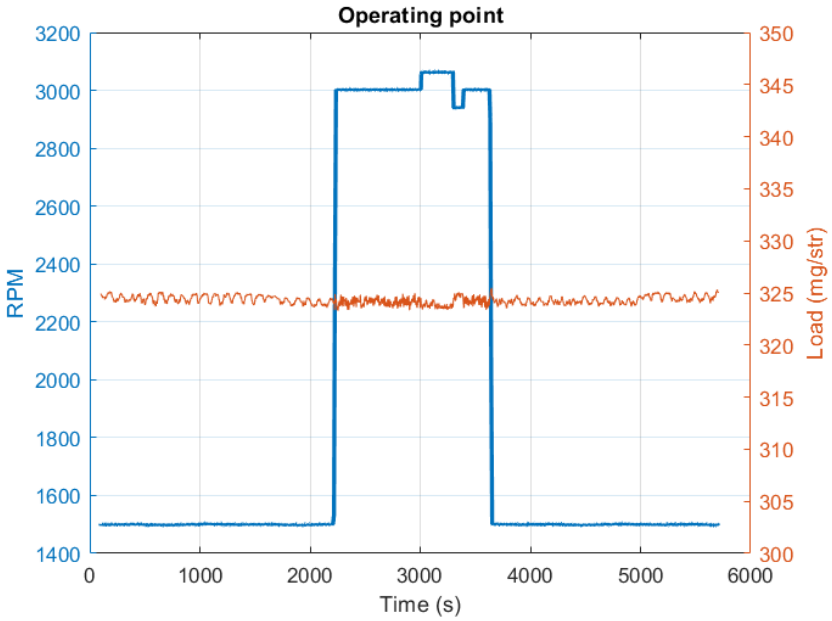


**Figure E.14:** Operating point at $\lambda = 0.90$ using 15mm catalyst

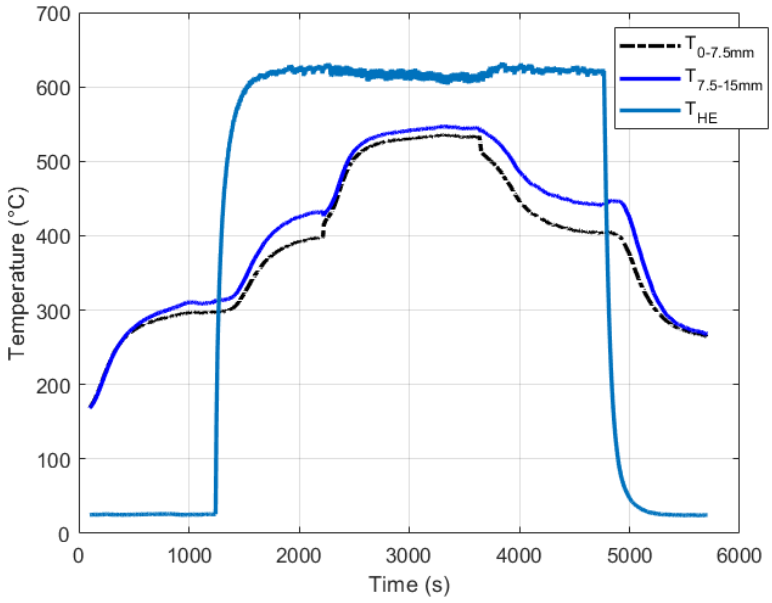


**Figure E.15:** Temperatures at $\lambda = 0.90$ using 15mm catalyst

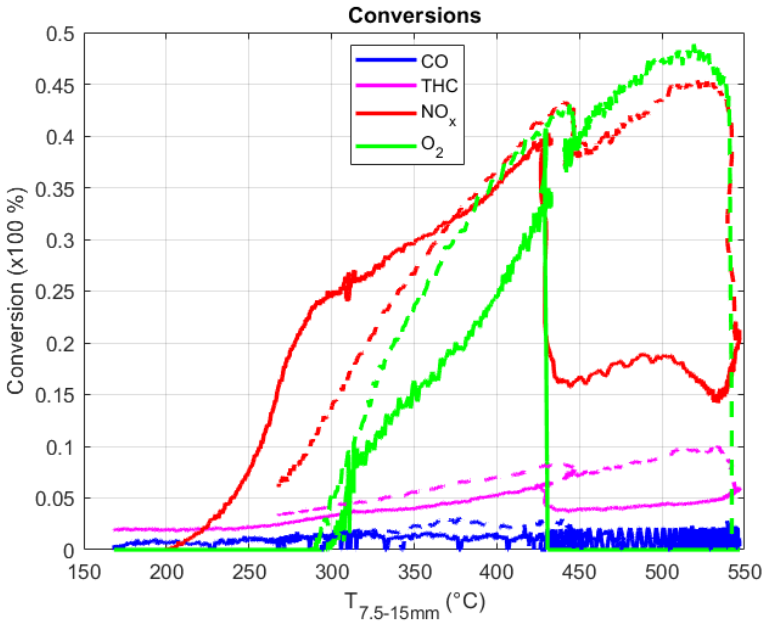


**Figure E.16:** Conversions at $\lambda = 0.90$ using 15mm catalyst

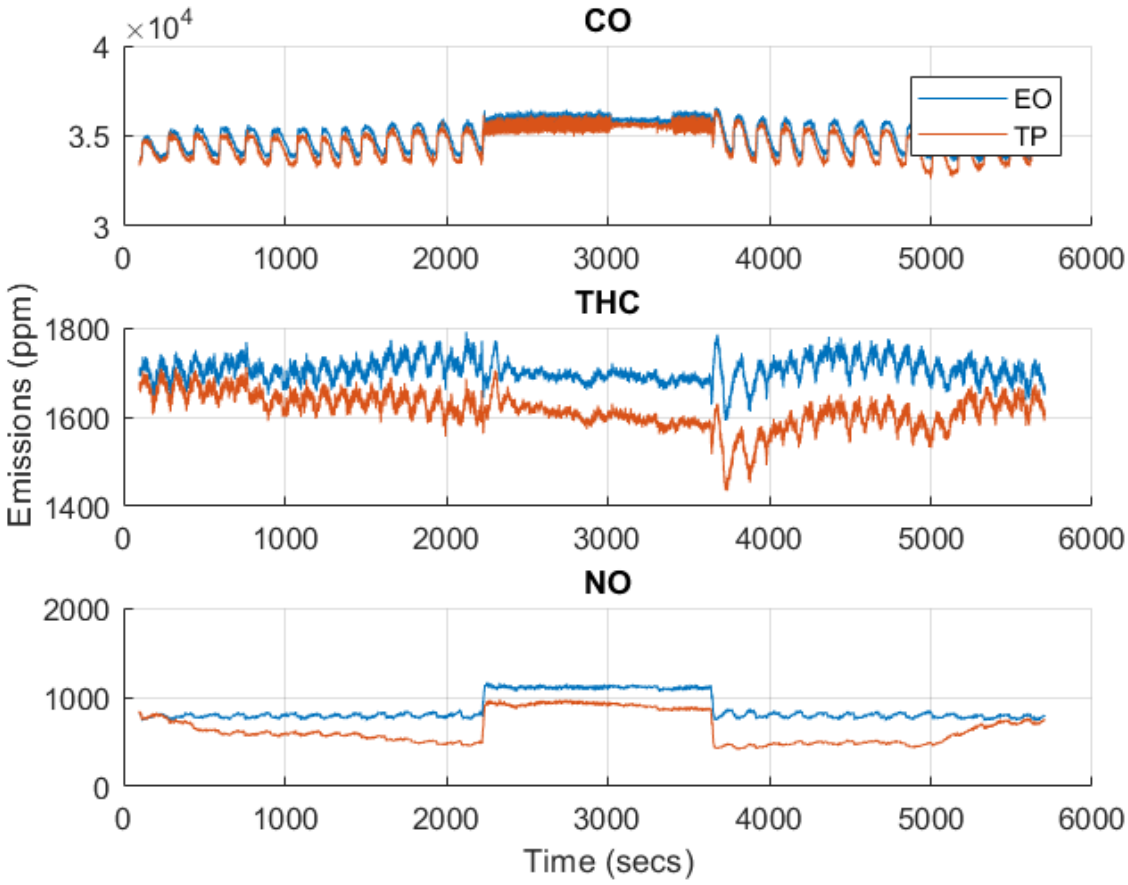


**Figure E.17:** Emissions pre- and post catalyst at $\lambda = 0.90$ using 15mm catalyst

**DEPARTMENT OF MECHANICS AND MARITIME SCIENCES**
**CHALMERS UNIVERSITY OF TECHNOLOGY**
Gothenburg, Sweden
www.chalmers.se


CHALMERS
UNIVERSITY OF TECHNOLOGY